Large Eddy Simulation in the Scalar Field

Dem Fachbereich Maschinenbau
an der Technischen Universität Darmstadt
zur Erlangung des Titels
eines Doktor-Ingenieurs (Dr.-Ing.) genehmigte

Dissertation
vorgelegt von

M.S. Ying Huai
aus China, Chengdu

Berichterstatter:	Prof. Dr.-Ing. Johannes Janicka
Mitberichterstatter:	Prof. Dr.-Ing. Egon P. Hassel
Mitberichterstatter:	Prof. Dr. rer. nat. Amsini Sadiki
Tag der Einreichung:	8.09.2005
Tag der mündlichen Prüfung:	6.12.2005

Darmstadt 2005
D 17

Acknowledgements

The present work has been done for the last three years during my scientific fellowship in the Institute of Energy and Power Plant Technology (EKT), Darmstadt University of Technology. The financial support comes from the Deutsche Forschungsgemeinschaft.

Completing this work would not have been possible without the support and inspiration from a large number of people. First of all I would like to thank professor Dr.-Ing. J. Janicka for enabling me to carry out this research. His guideline and experience in research gave me very valuable instructions. I admire the vigorous way he got the projects officially going.

I would especially like to thank my advisor, Professor Dr. rer. nat. A. Sadiki, for indoctrinating me into the ways of science, turbulence, and computer simulations, for his steadfast support, limitless patience, and encouragement that he has given to me and his other students, and for his commitment to excellence in research. He used a lot of time to make helpful comments on a draft of this dissertation.

This work has benefited greatly from discussions with many graduate students, postdoctoral fellows and visitors at EKT, among them, A.R. Kumar, B. Wegner, Dr.-rer.nat. A. Dreizler, M. Chrigui, J.C. Espada, Dr.-Ing. M. Klein, Dr.-Ing. A. Maltsev, Dr.-Ing. A. Yun gave me a lot of help throughout my studying. The conversations with them not only bring me new ideas in my researching topic but also expand my knowledge profiting from their experience.

Additional appreciations are of all my friends and other colleagues at EKT for numerous instructive discussions and many recreational activities.

Finally, I would like to mention all my families who always supported and encouraged me in everything I did.

Ying Huai

September 8, 2005

Contents

Nomenclature

QUANTITY	SYMBOL	COHERENT SI UNIT
angle	α	^{0}
Cartesian coordinates	*x, y, z*	m, m, m
correlation function		
spatial correlation function	R_{ij}^{L}	—
temporal correlation function	R_{ij}^{T}	—
longitudinal autocorrelation function	R_f	—
transversal autocorrelation function	R_g	—
time autocorrelation function	R_A^T	—
cross term	c_{ij}^{v}	m^2/s^2
density	ρ	kg/m^3
diameter	*D, d*	m
diffusion coefficient for mixture fraction	D_f	m^2/s
dissipation rate	ε	m^2/s^3
equivalence ratio	Θ	—
error	*e*	*
filter function	*G*	—
filter width	Δ	m
filter width in *i*th direction	Δ_i	m
flux blending factor	*o*	—
general variable	Φ	*
general diffusion coefficient	Γ_Φ	m^2/s
height	*H*	m

QUANTITY	SYMBOL	COHERENT SI UNIT
Kronecker delta	δ_{ij}	—
length	L	m
length scale		
length scale tensor	L_{ij}	m
characteristic length scale	L_C	m
Komogorov length scale	L_K	m
integral length scale	L_I	m
Taylor microscale	L_T	m
longitudinal Taylor microscale	L_T^{11}	m
transversal Taylor microscale	L_T^{22}	m
Batchelor scale	$L_{\phi B}$	m
scalar integral scale	$L_{\phi I}$	m
scalar Taylor microscale	$L_{\phi T}$	m
Leonard stress	L_{ij}^V	m^2/s^2
mechanical-to-scalar time-scale ratio	R_ϕ^T	—
mixture fraction		
instantaneous mixture fraction	f	—
temporal mean mixture fraction	F	—
fluctuation of mixture fraction	f'	—
model coefficient		
Smagorisnsky model	C_{sm}	—
dynamic procedure	C_{dy}	—
scale similarity model for SGS stress	C_{ss}	—
eddy diffusivity model	D_{ed}	—
scale similarity model for SGS scalar flux	D_{ss}	—
nonlinear model	D_{no}	—
anisotropy model	D_{an}	—
number of (time steps, grid points)	n	—
pressure	p	$Pa = N/m^2$
pressure parameter	P	$Pa = N/m^2$
Reynolds number	Re	—
radius	R	m

QUANTITY	**SYMBOL**	**COHERENT SI UNIT**
scalar	ϕ	—
scalar dissipation rate	ε_ϕ	1/s
scalar variance	ϕ'^2	—
Schmidt number	Sc	—
SGS Reynolds stress	R_{ij}^v	m^2/s^2
SGS scalar flux	J_{ij}^{SGS}	m/s
SGS scalar dissipation	ε_ϕ^{SGS}	$1/m^2$
SGS scalar variance	θ_ϕ	—
SGS stress	τ_{ij}^{SGS}	m^2/s^2
SGS stress (deviatoric part)	τ_{ij}^{SGS*}	m^2/s^2
source term	Q	*
strain-rate tensor	S_{ij}	1/s
stress tensor	τ_{ij}	m^2/s^2
surface	S	m^2
surface unit normal vector	$\vec{n}$	—
swirl number	Sw	—
turbulent Reynolds number	Re_t	—
turbulent Schmidt number	Sc_t	—
velocity vector	$\vec{U}$	m/s
characteristic velocity	U_c	m/s
instantaneous velocity components	u, v, w	m/s, m/s, m/s
temporal mean velocity	U, V, W	m/s, m/s, m/s
fluctuation of velocity	u', v', w'	m/s, m/s, m/s
viscosity		
dynamic (absolute) viscosity	μ	N s/m^2
kinematic viscosity	ν	m^2/s
volume	V	m^3
volume element	dV	m^3
wavenumber	K_w	—
width	W	m

The symbol * in the unit groups stands for a generic variables and is defined according to the particular dimension being described.

	QUANTITY	SYMBOL
SUBSCRIPTS	characteristic	c
	cross flow	cf
	jet flow	Jet
	central line	ce
	cross-section average	$profile$
	maximal	max
	scalar	ϕ
	subgrid scale	SGS
OPERATORS	filter operation	$\bar{...}$
	Faver filter operation	$\tilde{...}$
	test filter operation	$\hat{...}$
	Reynolds (local, time-) averaging	$\langle ... \rangle$
ABBREVIATIONS	air/fuel ratio	AFR
	central difference scheme	CDS
	coefficient of variation	CoV
	computational fluid dynamics	CFD
	control volume	CV
	direct numerical simulation	DNS
	excess air	XSA
	fuel/Air ratio	FAR
	large eddy simulation	LES
	mixedness parameter	MIX
	Reynolds averaging numerical simulation	RANS
	spatial mixing deficiency	SMD
	subgrid scale	SGS
	temporal mixing deficiency	TMD
	total variation diminishing	TVD
	upwind difference scheme	UDS

Chapter 1
Introduction

1.1 Motivation and Objective

Turbulent mixing is one of the operations applied most frequently in the chemical industry, both as an independent operation with the objective of obtaining homogeneity of a mixture*and as a means of increasing the contact surface in other operations (such as absorption, extraction or drying) [47], [33]. As in chemical engineering applications, in other process engineering dealing with mass, heat or scalar and momentum transfer as well as in combustion applications the need of efficient mixing systems and a reliable prediction of mixing is strongly increased, e.g. [79]. Although studies have been extensively carried out to clarify the physics of turbulent mixing processes (e.g. [35]), the extreme complexity due to the intriguing complex topology of fluid motions and scalar fields does not yet allow a satisfactory understanding (as pointed out in [84]). For complex configurations of technical importance in which experimental investigations are difficult to be accomplished, a comprehensive knowledge of phenomena can well be achieved only by solving the equations governing the processes involved in the frame of Computational Fluid Dynamics (CFD) [26].

In the field of CFD, Large Eddy Simulation (LES) [100] stands in the middle of the range of turbulent flow prediction tools, between Direct Numerical Simulation (DNS) [76] and Reynolds Averaging Numerical Simulation (here RANS) [25]. Under certain conditions RANS can be very accurate, but it turns out that it experiences some limitations for transient flows, where the averaging process wipes out most of the important characteristics of a time-dependent solution,

* Mixture results from the substances that are mixed, but not chemically combined. Mixtures are non-homogeneous, and may be separated mechanically.

which is important in a turbulent mixing process. DNS, on the other hand, attempts to resolve all temporal and spatial scales. As a result, the solution is very accurate. Unfortunately, DNS is computationally unrealistic for turbulent flows of high Reynolds number or high Schmidt/Prandtl number. That is, to resolve all spatial and temporal scales, the grids and time step width would need to be extremely small, resulting in a problem which would take an extraordinarily long time to solve with today's technology.

LES was originally implemented in the 1970s by atmospheric scientists to study the weather [54]. Since that time it has been utilized in almost every engineering field, e.g. [55]. LES seeks to directly resolve large spatial scales (like DNS), while modeling the smaller scales (like RANS). The basis is two-part. First, the larger scales carry the majority of the energy, and hence are more important. Second, the smaller scales have been found to be more universal, and hence are more easily modeled. The resulting methodology is a hybrid between these two methods, which involve the filtering of the governing equations to separate those scales which will be modeled from those which will be solved directly. It therefore allows generating useful solutions for transient and unsteady turbulent flows of engineering importance, while still maintaining computationally realistic costs.

The difficulties encountered in LES modeling scalar (such as energy, enthalpy, temperature, mass fraction of species, etc.) mixing processes can be primarily attributed to the interaction among turbulent stirring, molecular diffusion, and chemical reaction at the smallest scales of the flow [84]. Because these small scales are not resolved in any conventional LES numerical treatment, it is necessary to account for these effects on large scales. This might be achieved by subgrid scale (SGS) models. With regard to SGS models, high level modelisation of unsteady turbulent transport of momentum and scalar along with accurate numerical simulation tools are imperatively needed.

Therefore, focus will first be put especially on the modeling and validation part. Different SGS scalar flux models approaches will therefore be evaluated on the basis of their performance in predicting mixing processes and on the corresponding computational cost needed. This review criticizes the isotropic proposed SGS scalar flux models [6], [96] that may produce wrong impact of the small scales on the large scale physics. Thus, a new thermodynamically consistent SGS scalar flux model (named anisotropy SGS scalar flux model) will be proposed based on the

second law of thermodynamics. Unlike the isotropic models, the new model involves a SGS anisotropic diffusivity and takes into account the scalar gradient in all directions for each SGS scalar flux component. The aim is to achieve reliable numerical data relevant for the turbulent mixing process evaluation.

To gain quantitative view of mixing, parameters will be introduced to measure the processes at different macro and micromixing level. The purpose of this analysis is to bring valuable information for mixing optimization.

Some chemical or engineering processes are not running at high performance because the mixing has been neglected or designed incorrectly. An inefficient mixing can lead to a chain of related undesirable consequences: desired reactions are slowed, selectivity is decreased, and the accumulation of unwanted byproducts is increased. Since the amount of byproducts is directly related to the scale of downstream purification and separation units (and the use of solvents in the purification units often entails additional costs due to environmental and regulatory concerns), it is clear that a mixing optimization procedure is necessary to overcome such undesirable phenomena. In this work, a numerical optimization procedure will be introduced based on results of different mixing modification techniques. This procedure will then be applied to a specific mixer for demonstration. This investigation constitutes the second objective of the work.

1.2 Literature Survey

Because mixing is a widely practiced operation, there is a long history of mixing research [74]. In 1950s and 1960s, there were already some works concerning mixing problem, which mostly investigated the mixing happened in the nature [53] with simple measurements. With the aid of the development of computer performances, DNS is now being increasingly applied for mixing study (e.g. [10], [40] and [88]). However, it still remains limited to low Reynolds number not interesting for practical applications. Focused on technically relevant mixing processes, modeling of the turbulent mixing is therefore state of the art. Usually RANS (see [47] and therein mentioned references) is applied for the turbulent flow and scalar field description. Because the importance of unsteady large-scale turbulent structures in scalar mixing is now well recognized, the limitations of stationary RANS [22] in capturing unsteady processes suggest the

use of unsteady numerical methods. However, the ability of unsteady RANS (URANS) to predict accurately spatial-temporal phenomena is not yet clearly established. Therefore, the technique used in this work is the classical LES.

In classical LES (see [49], [100] and therein cited references), all scales of turbulent motion and scalar mixing larger than a certain scale are explicitly simulated using a time- and space-accurate scheme, while the effect of the unresolved smaller scales on the resolved part is modeled using a SGS model. This is generally relied on the information residing at filtered or resolved field. Because the modeling effort of turbulence is reduced to only small residual structures, this approach is accredited a high accuracy in capturing transport processes affected by resolved large scale structures. Nevertheless, some problems have to be faced.

One is a precise selection of boundary conditions along with numerical requirements to provide reliable and accurate LES results [85]. Another problem is how the SGS models for the momentum and scalar flux transport can be formulated in compatibility with the physics to be described [30].

The first problem represents the challenge how to impose correct instantaneous flow quantities at the inflow boundary using LES. One approach is simply to use a laminar flow by starting far upstream so that the natural transition to turbulence can occur. This procedure is not applicable for many turbulent flow simulations because simulating the transition is already costly, and coupling it with downstream simulation of turbulence becomes prohibitively expensive. To account for the turbulent inflow conditions, there exist various methods. One way to impose the fluctuations is to extract them from experimental data. Another way is the use of hybrid methods that attempt to combine RANS simulation and LES into one simulation by modifying the RANS Reynolds-stress tensor to incorporate SGS eddy viscosity solely based on mesh element size to distinguish the RANS simulation region from the LES. A recent view can be found in [30] and [68]. Even though these methods can impose fluctuations on boundaries, the complex implementation procedures reduce their applications.

With regard to SGS models in the velocity field, linear eddy viscosity based models are usually applied (e.g. [22], [28] and [107]). Thereby the SGS stress tensor is postulated to be proportional to the symmetric part of the resolved velocity gradient through the turbulent viscosity. The so-called Smagorinsky approach is acceptable for momentum transport. In this case all the

energy-containing scales are resolved, and all the unresolved scales, that are mostly isotropic in the inertial and dissipative range and mainly exhibit a universal structure, can be modeled in a simple way on the basis of scale separation assumption. To determine the model coefficient, the so-called dynamic procedure [67] seems to be useful. Based on the Germano identity, the model coefficient is determined as the calculation progresses rather than input a priori as in the standard Smagorinsky [54] model. It therefore makes possible the model coefficient to change with scale, improves substantially the prediction of spectra and mean velocity profiles as reported in [100]. These models appear to be successfully implemented in a number of engineering flows, e.g. [3]. However, all Smagorinsky-type models assume the equilibrium between production and dissipation of kinetic energy in small scales, which is difficult to be met in complex flows. To overcome the shortcomings, the so-called scale-similarity based models [48], the mixed model [34], [60] and the one-equation model [63] gained popularity while second order type-models [81] remain less considered.

Regarding the scalar flux transport, various models have been proposed including the probability density functions, the linear eddy model and diverse algebraic models as reviewed in [35]. The most popular is the linear eddy-diffusivity model relying on the SGS fluxes postulated proportionally to the resolved scalar gradients. New experimental findings show, however, that structured functions and derivative skewness of scalar field do not follow the assumption of isotropy at inertial and dissipation scales in presence of a mean scalar gradient (e.g. [101]). To account for this observed anisotropy behavior in the modeling, similarity models [6], serial decomposition closures and (non-linear) gradient models [35], [39] have been recently proposed besides a one-transport equation [73]. Analysis of DNS data confirms elevated correlation between real scalar flux vector (measured from the data) and modeled SGS scalar flux vector obtained by using these models [69] for simple configurations. When implemented in the simulations, the mixed models and the serial decomposition closure lead to more satisfactory results than the (non-linear) gradient model [35] at least in simple configurations, such as turbulent homogeneous isotropic flows, homogeneous shear layers and temporally developing shear layers as well as channel flows with differentially heated side walls.

Nonetheless, most simulations of complex flows of practical interest use the linear eddy diffusivity model due to low computational costs required. All these studies are often related to

the prediction of flow field (e.g. [16], [24]) and rarely reported for mixing problems (e.g. [56], [106]). Some works (e.g. [17], [80]) contributed to evaluate mixing efficiencies. However, detailed numerical studies of scalar field and systematic mixing analysis based on the influence of the mixing modeling in complex configurations of engineering relevance are not yet available. Only recently, C. Priere et al. [23] used LES to study the effect of mixing devices on a row of jets issuing into a duct, while B. Wegner et al. [19] investigated the effects of the variation of the angles of the jet on the mixing mechanism in a jet in cross flow configuration. However, these works only reach to the knowledge of mixing enhancement by the adjustment of handling parameters. A further optimization study appears in very limited papers recently. For example, K. Park et al. [61] used shape optimization of the plate–fin type heat sink with vortex generator to minimize the pressure loss subjected to the desired maximum temperature. Even though these works have introduced optimization techniques into the mixing mechanism, there still has a gap to implement these studies in various engineering applications because of their accuracy and/or efficiency, which formulates an important objective of this work using LES.

In this work, the mixing investigation involves modeling (a new developed anisotropy SGS scalar model is proposed and implemented), analysis (mixing parameters are introduced to evaluate the mixing degree concerning macro and micromixing) and optimization (A numerical optimization procedure with LES is introduced). These items are illustrated with different configurations which include a mixing layer, jet in cross flow, jet in channel flow and impinging jet configuration.

1.3 Structure of the Thesis

To cover the backgrounds, Chapter 2 begins with an introduction of the physics nature of turbulent flows and mixing. After this general view, governing equations used to describe the flow and scalar motion will be presented in Section 2.2, 2.3 and 2.4 respectively. To characterize the mixing ratio, mixture fraction is utilized throughout this thesis. The mathematical definition and governing equation of mixture fraction will be introduced in Section 2.5.

The development of different numerical simulations is based on the understanding of the scaling phenomena. Therefore, the first two sections in Chapter 3 will be addressed to expatiate on the

scale of turbulent flow and scalar mixing. Afterwards, the three simulation methods, DNS, RANS and LES will be outlined in Section 3.3, 3.4 and 3.5. The statement focuses on presenting the state of development of these strategies, and outlining some challenges that lie ahead, in terms of applications, numerical and modeling issues.

In Chapter 4, the focus will be deposited on LES of scalar mixing. The formulation of LES (Section 3.1) indicates that the contribution of the small scales (removed by a filter operation) should be parameterized as a function of the resolved field using SGS models. In Section 3.2, classical SGS stress models are reviewed. A state-of –the-art study of SGS scalar flux models is presented in Section 3.3 and the new developed anisotropy model will be a highlight in this section.

After selecting the simulation tool, one has to consider a suitable discretization method of approximating the governing equations by a system of algebraic equations for the variables at some sets of discrete locations in space and time. The discretization method (Finite Volume), the discretization procedure of different terms in governing equations and corresponding solution methods will be compactly introduced in Chapter 5.

In Chapter 6, the applications of the derived LES code to the simulation of mixing processes is presented and discussed in different configurations. In Section 6.1, a spatially developing turbulent mixing layer is considered as starting point for model assessment. Section 6.2 is concerning with a jet in cross flow configuration which represents mixing gas systems characterized by a small Schmidt number. Section 6.3 presents mixing process in a jet in channel flow configuration. This is confined configuration and water steam is considered introducing high Schmidt number effects. The systematical model assessment, which includes the computation and comparison of the numerical results with experimental data, is carried out throughout this chapter.

With these simulation results, Chapter 7 will devoted to mixing analysis, enhancement and optimization. In Section 7.1, the mixing evaluation is carried out by means of mixing parameters and the mixing enhancement study is implemented on the jet in cross flow configuration with variation of different handling conditions. Thereafter mixing optimization procedure is presented and applied to an impinging jet configuration. The improvable issues and the unclosed problems will be summarized in Section 7.2.

Chapter 8 summarizes the thesis, addresses open questions and presents future issues.

Chapter 2
Turbulent Flow and Mixing

All the CFD effort contributes to achieve qualitative and quantitative descriptions of fluid behaviors. The first step toward providing a categorization of these studies responses to theorize the physical nature of fluids. Between different states of fluid flows, turbulent flows gain more attention because of their importance. Mixing processes caused by the turbulence shares some common features as turbulent flows, yet has own physical properties. Therefore, the following section begins with an introduction of the physical nature of turbulent flows and mixing processes. The mathematical equations used to describe the important quantities in scalar mixing processes as well as in the flow field will be summarized afterwards.

2.1 The Physical Nature of Turbulent Flows and Mixing Processes

Fluid flow can be classified into one of two broad categories or regimes: laminar flow and turbulent flow. Most of flows encountered in nature as well as in industrial applications are turbulent. However, turbulent flows are among the most mathematically complex phenomena in nature. Capricious and chaotic, they present a formidable challenge to the researcher seeking to form abstract theory from empirical observation. Important observations can be obtained by experimental observations. Reynolds, at the end of the nineteenth century (1883), observed the instability of transition and turbulence in a pipe flow. He noticed in his experiments that the flow behavior is dependent upon a non-dimensional parameter. This parameter, which also provides a criterion for dynamic similarity, is the Reynolds number [72]:

$$\mathrm{Re} = \frac{U_c L_c \rho}{\mu} = \frac{U_c L_c}{\upsilon}, \tag{2.1}$$

where U_c and L_c are characteristic velocity and length scales of the mean flow, ρ is fluid density and μ, ν are the dynamic and kinematic fluid viscosity. The physics of Reynolds number is the ratio of inertial forces ($U_c\rho$) to viscous forces (μ/L_c) and is used for determining whether a flow is laminar or turbulent. Laminar flow occurs at low Reynolds numbers, where viscous forces are dominant, and is characterized by smooth, constant fluid motion, while turbulent flow, on the other hand, occurs at high Reynolds numbers and is dominated by inertial forces.

The physical nature of turbulence has been introduced in many works (e.g. [91]), which can be summarized as the fluid motion in which the flow properties, such as velocity, are varying randomly both in time and in space resulting in a wide range of flow scale structures. Thereby the turbulence energy is dissipated from larger scales to small scales. At the smallest scales, due to viscous effects the kinetic energy of the fluid is converted into heat. However the smallest scales are much larger than the molecular mean free path, so that turbulence is a continuum phenomenon. This phenomenon is intrinsically three-dimensional and diffusive which causes mixing and rates of mass, momentum, and heat transfer much more effectively than a comparable laminar flow.

That turbulence can produce rapid mixing is one of important dynamics of turbulent flows. A mixing problem can be described as a configuration that is initially composed of two distinct and segregated scalar constituents which may be differentiated by different chemical compositions, different temperatures, different trace elements, or any other scalar marker. The mixing process, throughout its development, is to mix these different constituents at the molecular level to produce a homogeneous mixture, as shown in Figure 2.1, which is experimental picture of a turbulent jet of water plus dye discharging in a square, transparent, long duct [33]. The ability of turbulent flows to effectively mix entrained fluids to a molecular scale has wide-ranging consequences in nature and engineering.

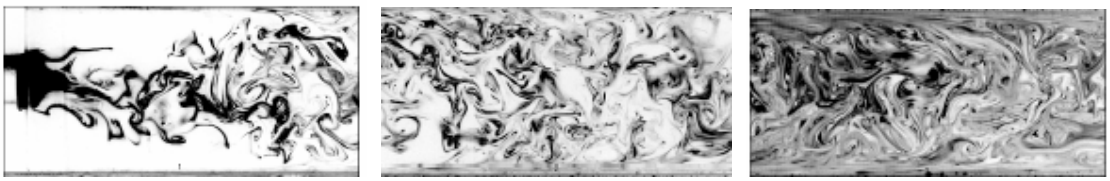

Figure 2.1: Successive mixing states of a dye discharging from a jet in a square duct [33]

In general, there are two distinctly different physical processes involved in turbulent mixing: turbulent stirring (convection), and molecular diffusion. If chemical phenomena are involved, a third process, the chemical reaction rate, involving yet another contribution must be accounted for. Chemical reaction, of course, can occur only when the mixing already is achieved at the molecular level.

With regard to the turbulent convection, let's consider a turbulent flow field containing two different constituents, initially unmixed. The action of this flow field on the scalar field is to disorder and increase the surface area of the interface between the two constituents, As a result, the gradients of the scalar constituents will be increased and the scalar length scale will be decreased. As a result of this "stirring" process a complex structure of the scalar field evolves. Stirring has the effect of redistributing the scalar field throughout the flow field.

Mixing at the molecular level is a diffusion process. The turbulent stirring process described above acts only to redistribute or convect scalar throughout the flow domain. Without molecular diffusion, intermixing of separate constituents will not occur. The macroscopic view of molecular diffusion is a result of random motion (Brownian motion) of fluid particles at the molecular level. This process is most effective in regions of high gradients and acts most effectively at the smallest scales of the flow.

A little time spent thinking these processes reveals the difficulties in mathematically describing and predicting the turbulent mixing process. Today it's still a considerable experimental, theoretical, modeling, and computational challenge to capture and represent turbulent mixing processes. It can not be parameterized easily in terms of the features of flow. As a result, an additional equation to describe of the scalar field is, in principle, necessary.

2.2 Governing Equations of Fluid Motion and Mixing

The foundational axioms of fluid dynamics are the conservation laws, specifically, conservation of mass, momentum (also known as Newton's second law) and total energy. These are based on classical mechanics and can be extended to relativistic mechanics, which we do not consider here.

In addition, a general scalar transport equation is used to predict the scalar motion in mixing

processes. In order to characterize mixing processes, mixture ratios quantities will be introduced along with the mixture fraction formalism.

Detailed mathematical derivative procedures are recalled in Section 2.2.1 in order to introduce mathematical notations. The sections afterwards will only focus on the formulas which will be used later on in the thesis.

2.2.1 Conservation of Mass

The conservation of mass stems from the principle that mass can not be created or destroyed inside the control volume. Obviously, we may have situations (e.g. nuclear reactions) involving the conversion of mass into energy. This case is not considered in this work.

Let V be a control volume, a balloon like shape in space. By assumption, it and its surface S remain fixed in space. The surface is permeable so that fluid can freely enter in and leave. The continuity equation says that the time rate of change of the mass within the control volume V equals to the rate at which mass enters V through the boundary S.

The control volume V may be made of several infinitely small (infinitesimal) volume elements dV. The mass of the fluid inside each of these elements is ρdV . The density ρ is free to change from point to point, from one sub-element to another within V. Thus,

$$\text{Total mass within V} = \iiint_V \rho dV \,. \tag{2.2}$$

In the above equation, the three integral signs simply indicate that we are doing a three-dimensional integration, or volume integration. Then,

$$\text{Time rate of change of mass within the control volume V} = \frac{\mathrm{d}}{\mathrm{dt}} \iiint_V \rho dV \,. \tag{2.3}$$

In calculus, the order of integration or differentiation may be interchanged so that these operations do not interfere with each other. Since the volume is fixed in space, the limits of the volume integral are not functions of time, and there is no interaction between the two operations. Thus,

$$\text{Time rate of change of mass within the control volume V} = \iiint_V \frac{\partial \rho}{\partial t} dV \,. \tag{2.4}$$

Notice that the partial derivative inside the integral is used since ρ is a function of (*x, y, z, t*) and the only interest is its variation inside each sub-element *dV* with respect to time, while the spatial location (*x, y, z*) of the sub-element *dV* remains fixed.

Similar, the surface *S* is made of many quilt-like infinitesimal patches *dS*. At the center of each element is a unit normal vector (i.e. a vector of length unity, normal to the surface) $\vec{n}$. By common convention, this normal is pointing away from the surface *dS*. The normal component of fluid velocity $\vec{U}$ pointing towards the control volume (entering the control volume) is given by $-\vec{U} \bullet \vec{n}$.

Therefore, the rate at which mass enters the control volume through *dS* as the product of density times normal velocity times area. Thus,

$$\text{Rate at which mass enters the control voume through dS} = -\rho\vec{U} \bullet \vec{n}dS \,. \tag{2.5}$$

Then,

$$\text{Rate at which mass enters the control voume through the entire surface S} = -\iint_S \rho\vec{U} \bullet \vec{n}dS \,. \tag{2.6}$$

Equating the relation (2.4) and (2.6),

$$\iiint_V \frac{\partial \rho}{\partial t} dV = -\iint_S \rho\vec{U} \bullet \vec{n}dS \,, \tag{2.7}$$

moving the right side to left, it becomes the conservation of mass equation in integral form:

$$\iiint_V \frac{\partial \rho}{\partial t} dV + \iint_S \rho\vec{U} \bullet \vec{n}dS = 0 \,. \tag{2.8}$$

Note that equation (2.8) holds for steady or unsteady, viscous or inviscid, compressible or incompressible, two-dimensional or three-dimensional flow.

According to divergence theorem, the surface integral in the continuity equation changes to

$$\iiint_V \frac{\partial \rho}{\partial t} dV + \iiint_V \nabla \bullet \left(\rho\vec{U}\right) dV = 0 \,, \tag{2.9}$$

or

$$\iiint_V \left[\frac{\partial \rho}{\partial t} + \nabla \bullet \left(\rho\vec{U}\right)\right] dV = 0 \,. \tag{2.10}$$

Consider the above volume integral. It must hold for any arbitrarily shaped control volume *V*, at any instance in time for all flows. The only way this can be true is if the integrand is zero. Therefore,

$$\frac{\partial \rho}{\partial t} + \nabla \bullet \left(\rho \vec{U} \right) = 0 . \tag{2.11}$$

Equation (2.11) is called the differential form of continuity equation. In this case of constant density flows (i.e. flows in which ρ is independent both of space and of time), the evolution equation above degenerates to the kinematical condition that the velocity field be solenoidal or divergence-free

$$\nabla \bullet \left(\vec{U} \right) = 0 . \tag{2.12}$$

For the three dimensional flow, the fluid velocity vector $\vec{U}$ contains three components u_i ($i = 1, 2, 3$) denoted the velocity at x_i direction. Equation (2.11) and (2.12) can be written for the component *i* as:

$$\frac{\partial \rho}{\partial t} + \frac{\partial \rho u_i}{\partial x_i} = 0 , \tag{2.13}$$

and

$$\frac{\partial u_i}{\partial x_i} = 0 . \tag{2.14}$$

To be consistent, the equations presented afterwards all follow the expressions like equation (2.13) and (2.14). Their derivations can be achieved in the similar way as demonstration above.

2.2.2 Conservation of Momentum

The Conservation of momentum states that the fluid particle will not change its velocity unless a force is experienced by the fluid. The forces may be surface forces described by the stress tensor τ_{ij}. The body force of interest is gravity acceleration g_i, which denotes the body force per unit mass These forces cause the fluid to accelerate according to the momentum equation

$$\frac{\partial \rho u_i}{\partial t} + \frac{\partial \rho u_i u_j}{\partial x_j} = -\frac{\partial p}{\partial x_i} + \frac{\partial \tau_{ij}}{\partial x_j} + \rho g_i , \tag{2.15}$$

where p is pressure. The specific fluid studied in this thesis is Constant-property Newtonian fluid in which shear stress is linearly proportional to the velocity gradient in the direction perpendicular to the plane of shear. The constant of proportionality is known as the viscosity. For a Newtonian fluid, the viscosity by definition depends only on temperature and pressure, and also on the chemical composition of the fluid if the fluid is not a pure substance. If the fluid is incompressible and viscosity is constant across the fluid, the stress tensor in this flows can be expressed by (based on Stokes hypothesis [52])

$$\tau_{ij} = \rho\upsilon\left(\frac{\partial u_j}{\partial x_i} + \frac{\partial u_i}{\partial x_j}\right) - \frac{2}{3}\rho\upsilon\frac{\partial u_\kappa}{\partial x_\kappa}\delta_{ij}, \tag{2.16}$$

where δ_{ij} is the Kronecker delta ($i = j \rightarrow \delta_{ij} = 1; i \neq j \rightarrow \delta_{ij} = 0$). Inserting equation (2.16) into equation (2.15) and exploiting equation (2.13), for the isothermal incompressible flow of a Newtonian fluid, the Navier-Stokes equation can be obtained

$$\frac{\partial \rho u_i}{\partial t} + \frac{\partial \rho u_i u_j}{\partial x_j} = -\frac{\partial p}{\partial x_i} + \frac{\partial}{\partial x_j}\left[\rho\upsilon\left(\frac{\partial u_j}{\partial x_i} + \frac{\partial u_i}{\partial x_j}\right) - \frac{2}{3}\rho\upsilon\frac{\partial u_\kappa}{\partial x_\kappa}\delta_{ij}\right] + \rho g_i. \tag{2.17}$$

2.2.3 Scalar Transport Equation

As mentioned in section 2.1, by turbulent mixing, two main processes will bring separate constituents of flow together to finally interact at the molecular level. The governing equation of scalar transport equation is formulated as:

$$\underbrace{\frac{\partial \rho\Phi}{\partial t}}_{accumulation} + \underbrace{\frac{\partial \rho\Phi u_i}{\partial x_i}}_{convection} = \underbrace{\frac{\partial}{\partial x_i}\left(\Gamma_\Phi \frac{\partial \Phi}{\partial x_i}\right)}_{diffusion} + \underbrace{Q_\Phi}_{source}. \tag{2.18}$$

In equation (2.18), Φ represents a general scalar field and the first term describes the accumulation of the scalar at any point and any time. The scalar is convected by the velocity u_i and diffused with the diffusion coefficient Γ_Φ. Φ is conserved if there is no source tem or sink term Q_Φ. When a chemical reaction process is involved, the source term Q_Φ accounts for the chemical product generation or suppression.

Equation (2.18) is a general transport equation, which can be used to predict any scalar quantities,

such as energy, enthalpy, temperature, mass fraction of species, etc. For specific problems in the work, the utility of the equation will be used to predict a conserved and passive scalar motion in mixing processes. It is passive because (by assumption) its value has no effect on material properties (i.e. ρ, υ and Γ_{Φ}) and hence it has no effect on the flow. Passive scalar mixing processes [109] are relevant in many engineering applications as they are demonstrated throughout this work.

2.2.4 Mixture Ratio and Mixture Fraction Transport Equation

One of most vital operation parameters of a mixer or combustion system is the mixture ratio. That is the ratio either locally or overall, in which two separate inflows, e.g. the fuel and air are present in system. This will affect the mixing or combustion system performance, efficiency and product characteristics.

In the case where air and fuel are initially separated (non-premixed combustion) there is an infinite range of ratios ranging from pure fuel to pure air. In the case where fuel and air are initially mixed, there is only one mixture ratio throughout. How do we define this mixture ratio? The answer can be found in many different ways:

- **Air/Fuel Ratio (AFR)**

This is the most common method of mixture definition and is simply the ratio by mass of the air and fuel at the point of interest.

- **Fuel/Air Ratio (FAR)**

This is the inverse of AFR but is not so common because in the majority of cases, it is significantly less than unit.

- **Equivalence Ratio (Θ)**

This is also a very common one. It is defined as the ratio between the actual FAR and the stoichiometric FAR at given location. Hence, if we have a stoichiometric mixture ratio, then the equivalence ratio is one. If the mixture is lean, the value is less than one. If the mixture is rich, the value is greater than one. This value is somewhat more difficult to calculate than others but is ideal for situations where the fuel might change. Its value is independent of fuel unlike AFR or

FAR where the stoichiometric value is a function also of fuel itself.

– **Excess Air (XSA)**

Especially for correlation, the majority of combustion systems operate with a slight excess of air. This prevents the formation of products of incomplete combustion (also termed unburned hydrocarbons, UHC, or volatile organic component, VOC) which can be very toxic and are legislates against. The "excess air" is defined as the percentage of air in the system by mass which is surplus to requirements for complete combustion. This property has no meaning if the system is rich.

– **Mixture Fraction (f)**

This is a relative newcomer to the field and has been derived by combustion modelers who need to have property which is bounded. The problem with all the parameters so far is that they have a value of infinity at either the pure air or pure fuel side (AFR, FAR, Θ) or they do not map the complete mixture spectrum (XSA). This is no good to computer modeler since computers get very upset when they try to calculate infinity.

Mixture fraction, equation (2.19), is defined as the ratio by mass of mixture which originated from the fuel stream (stream 1) as opposed to the oxidant stream (stream 2). Thus,

$$f = \frac{stream1}{stream1 + stream2} = \frac{1}{1 + \dfrac{stream2}{stream1}} = \frac{1}{1 + AFR}. \tag{2.19}$$

In the air steam, AFR=∞, and thus $f = 0$; in the fuel steam, AFR=0, and thus $f = 1$.

All investigation of mixing considered in this work is based on the concept of mixture fraction. Based on equation (2.19), the mixture fraction is usually calculated as a normalization of any conserved scalar, i.e. non-reactive scalar (mass fraction of element, enthalpy, passive scalar concentrate, etc.). At its most basic level, mixture fraction is a generic mixing variable that represents the relative amount that each inflow stream contributes to the local mixture. In the case we considered two separate inflows 1 and 2, feed into the mixing system with scalar concentration ϕ_1 and ϕ_2, then the mixture fraction f is rewritten as:

$$f = \frac{\phi_1}{\phi_1 + \phi_2}, \tag{2.20}$$

with bounded values between *0* and *1*. To describe the transport of *f*, equations (2.18) for

conserved scalars with $Q_\Phi = 0$ can be directly used for the mixture fraction as:

$$\frac{\partial \rho f}{\partial t} + \frac{\partial \rho f u_i}{\partial x_i} = \frac{\partial}{\partial x_i}\left(\rho D_f \frac{\partial f}{\partial x_i} \right). \tag{2.21}$$

The only parameter that needs to be determined is the diffusion coefficient for mixture fraction D_f. Diffusion coefficient is a parameter expressing the transfer rate of a substance by random molecular motion. It is expressed, as a ratio of viscosity ν and molecular Schmidt (Prandtl) number *Sc* as:

$$D_f = \frac{\nu}{Sc}. \tag{2.22}$$

Sc is a dimensionless parameter and is proportional to the ratio: kinetic viscosity/molecular diffusivity, which is used in mass transfer in general and diffusion in flowing systems calculation in particular. Analogous to the Schmidt number, the Prandtl number is proportional to the ratio: thermal diffusivity/molecular diffusivity and is used in heat transfer in general and free and forced convection calculation in particular.

Equation (2.13), (2.17) and (2.21) are sufficient to describe the passive scalar motion in a (turbulent) mixing system. They are termed as “governing equations” in this thesis.

Chapter 3
Turbulent Modeling and Simulation

A solution to the problem of turbulence remains elusive despite the intensive research effort of the past century (see e.g. [99]). While the basic equations of the turbulence are known (Chapter. 2), they cannot be solved directly in the high Reynolds number turbulent flows of technology importance due to the wide range of length and time scales that are present.

In this regard, experimental studies (see e.g. [29] and [46]) are intensively carried out to gain insight in the understanding of the structure of turbulent flows. Flow visualization has been particularly useful in the identification of the coherent eddies that are responsible for most of the energy production, especially in regions of high shear. Measurement techniques have progressed significantly: it is now possible to obtain single-point measurements of velocity and velocity gradient components using Laser-Doppler Velocimetry or multiple wire anemometers, or velocity distributions in a plane, through Particle-Image or Particle-Tracking Velocimetry. Experiments have proved to be an efficient means of measuring global parameters, like drag, lift, pressure drop, or heat coefficient, etc. However, experiments are very difficult if not impossible in other cases. For example, the measuring equipment might disturb the flow or the flow may be inaccessible (e.g. flow of a liquid silicon in a crystal growth apparatus). Some quantities are simply not measurable with present techniques or can be measured only with an insufficient accuracy. In many cases where details are important, or when new high technology applications or design processes demand predication of flows for which the database is insufficient, comprehensive experiments may be too costly and/or time consuming. In this regard, numerical solutions are particularly essential.

By the 1960s, high speed computers become widely available and numerical solutions of Navier-Stokes equations started to appear regularly in the literature. In this chapter, a general overview of mathematical formulations and numerical techniques used for the solution of turbulent flows and mixing is presented. Among different strategies for analysis of turbulent phenomena, the

statement below focuses on presenting the state of the development of RANS, DNS and LES, and on outlining some challenges that lie ahead, in terms of applications, numerical and modeling issues. The major difference of these analysis methodologies is stemmed from the resolution degree of turbulent scales. The first two sections therefore begin with an introduction of the scales of turbulent motion and mixing. Section 3.3 will focus on DNS followed by RANS in Section 3.4. The last section in this chapter, Section 3.5, is devoted to LES which is the method applied in this work.

3.1 Scales of Turbulent Motion

As reviewed by A. Maltsev, 2003, turbulent flow consists of a superposition of eddies of every smaller sizes. The rate at which the turbulent kinetic energy is transfer from bigger eddies to smaller eddy is called the dissipation rate ε. The energy cascade, however, can not be extended infinitely because of the viscous forces. The smaller an eddy, the greater the velocity gradient inside the eddy and the greater the viscous stress that counteracts the eddying motion. Consequently, there is a statistical lower limit of smallest eddy size that corresponds to a minimum scale of turbulence and maximum frequency in the turbulent motion. At this limit this kinetic energy of the fluctuating motion dissipates completely into the internal energy of the flow. The length scales of such smallest eddy are called Kolmogorov scale and it defined as:

$$L_K = \frac{\nu^{3/4}}{\varepsilon^{1/4}}. \tag{3.1}$$

The correspond Kolmogorov time scale is

$$T_k = \frac{\nu^{1/2}}{\varepsilon^{1/2}}. \tag{3.2}$$

The major part of the turbulent kinetic energy is contained in the large but not the largest eddies. The large eddies are, therefore, often called energy containing eddies. The length and time scale of those eddies are further important scales. The size of energy containing eddies depends on the geometry of a spatial domain and on the local intensity of turbulence. This size can be related (it is not exactly the same) to the integral turbulent length scale that can be determined from the two-point spatial correlation function R_{ij}^L for statistical steady (time independent) turbulence.

$$R_{ij}^L(x, x+\Delta x) = \frac{\left\langle u_i'(x) u_j'(x+\Delta x) \right\rangle}{\sqrt{\left\langle u_i'^2(x) \right\rangle} \sqrt{\left\langle u_j'^2(x+\Delta x) \right\rangle}}, \tag{3.3}$$

as

$$L_{ij}(x) = \frac{1}{2}\int_{-\infty}^{+\infty} R_{ij}^{L}(x, x+\Delta x)d(\Delta x)\,, \tag{3.4}$$

where $u_i'(x)$ is the velocity fluctuation at spatial location x, $u_j'(x+\Delta x)$ is the velocity fluctuation at a distance Δx from x and the bracket denotes averaged values. Here, L_{ij} denotes the length scale tensor. For homogenous isotropic turbulence the integral length scale is independent of the direction and is given by

$$L_I = \frac{1}{3}L_{ii}\,. \tag{3.5}$$

This two-point velocity correlation function for homogenous isotropic turbulence and the corresponding integral turbulent length scale are schematically shown in Figure 3.1.

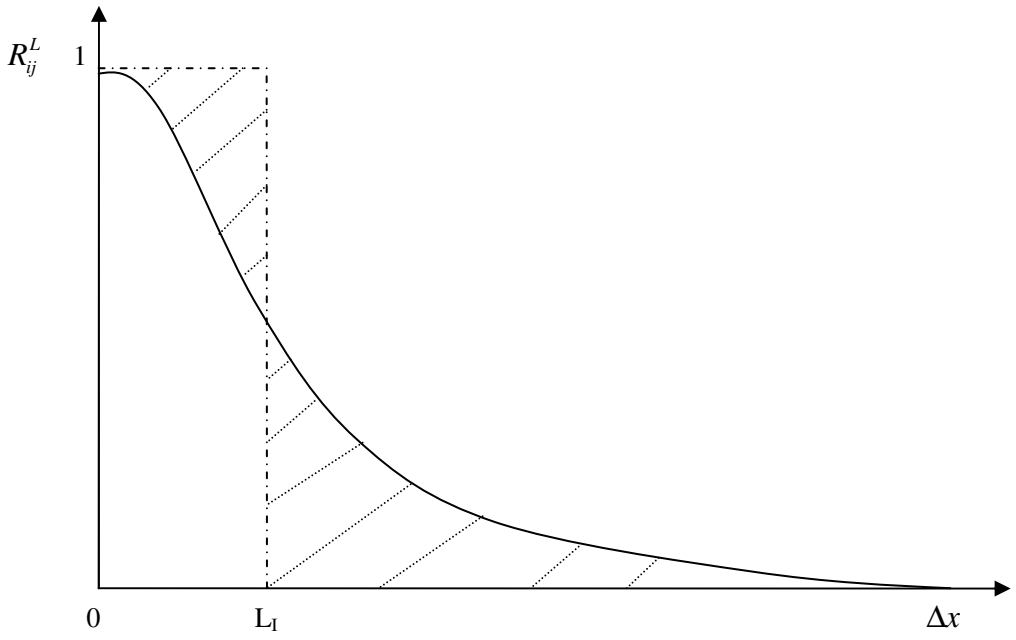

Figure 3.1: Two-point velocity correlation function versus the distance between two points Δx for homogenous isotropic turbulence

R_{ij}^{L} is a measure for the correlation of velocity fluctuation at the point x and $x+\Delta x$, thereby indicating to which degree the turbulent proportion of two points with distance Δx influence each other. L_I is located where the shaded areas above and below the two-point velocity correlation are of equal size. Hence the integral length scale L_I can be interpreted as the length scale from which point on the velocity fluctuation are predominantly uncorrelated.

The corresponding time scale can be determined from the known time correlation function

$$R_{ij}^{T}(x,t,x+\Delta x)=\frac{\left\langle u_i'(t)u_j'(t+\Delta t)\right\rangle}{\sqrt{\left\langle u_i'^2(t)\right\rangle}\sqrt{\left\langle u_j'^2(t+\Delta t)\right\rangle}}, \tag{3.6}$$

as

$$T_{ij}(x)=\frac{1}{2}\int_{-\infty}^{+\infty}R_{ij}^{T}(t,t+\Delta t)d(\Delta t). \tag{3.7}$$

Assuming isotropy and homogeneity leads to

$$T_I=\frac{1}{3}T_{ii}. \tag{3.8}$$

Qualitatively the integral turbulent time scale can be interpreted as an averaged inverse rotational frequency of the typical big eddy appearing in the spatial location *x*.

Though turbulence in practical flows is neither isotropic nor homogenous, the idealized integral length scale provides at least coarse quantitative information about spatial correlation and sizes of typical energy containing eddies in turbulent flows. Quantitatively the integral turbulent length scale can be interpreted as an averaged radius of typical big eddy appearing in the spatial location.

Other widely used length scales are Taylor microscales L_T, which can be determined by autocorrelation functions near the origin. In terms of the longitudinal autocorrelation function $R_f(r,t)$ and the transversal autocorrelation function $R_g(r,t)$ (S. Pope 2000), two corresponding quantities can be defined at the Taylor microscale level as:

$$L_T^{11}(t)=\left(-\frac{1}{2}\frac{\partial^2 R_f}{\partial r^2}(0,t)\right)^{-1/2}, \tag{3.9}$$

and

$$L_T^{22}(t)=\left(-\frac{1}{2}\frac{\partial^2 R_g}{\partial r^2}(0,t)\right)^{-1/2}=\frac{1}{\sqrt{2}}L_T^{11}(t), \tag{3.10}$$

where L_T^{11} is longitudinal Taylor microscale and L_T^{22} is the transversal Taylor microscale. A Taylor-time microscale can also be defined analogously.

The turbulent kinetic energy spectrum obtained from the Fourier transfer of the spatial isotropic two-point correlation R_{ij}^{L} function is schematically plotted in Figure 2.1. $E_w(K_w)$ is kinetic energy density per wave number K_w or the inverse turbulent length scale. The maximal value of $E_w(K_w)$ corresponds to the energy containing scale that related to the turbulent length scale L_I. The

eddies of size smaller than the energy containing eddied build the inertial sub-range, where Taylor microscale is located between L_I and L_K, according to $L_T = \sqrt{\mathrm{Re}} L_K$. As it was shown by Kolmogorov, the energy transfer from the large to small scale within the inertial subrange is independent on the scale size and followed to the $\sim K_w^{-5/3}$. At the right side of the inertial subrange the wave number corresponding to the Kolmogorov scale is located.

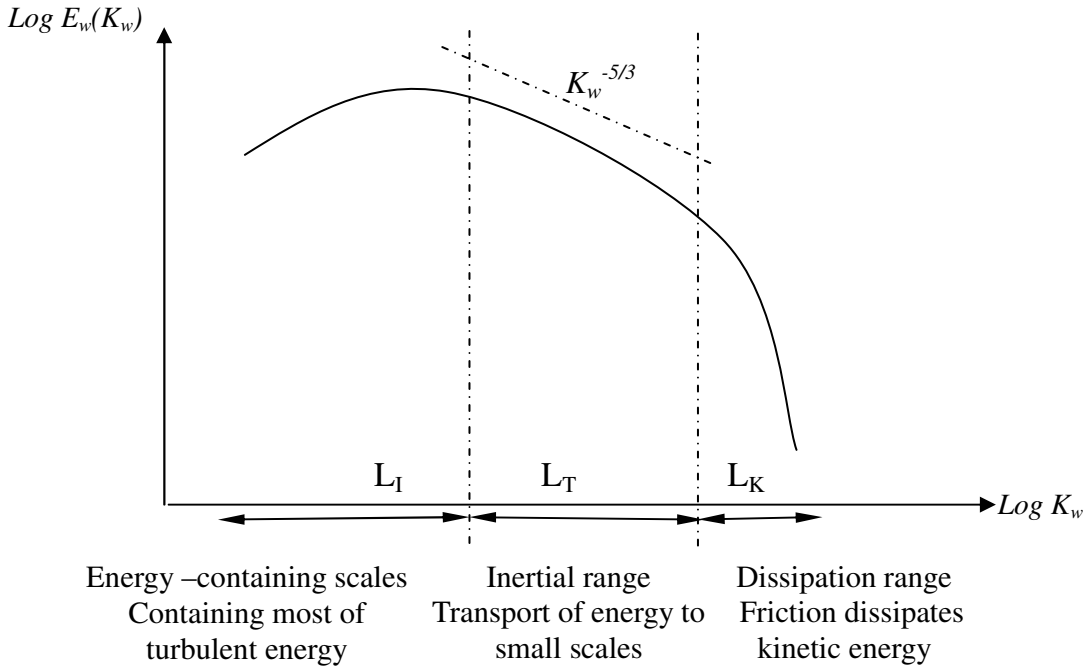

Figure 3.2: Schematic turbulent kinetic energy spectrum

3.2 Scales of Turbulent Mixing

In many physical situations one encounters a scalar ϕ advected by turbulent flow fields like temperature and pollutants in air and water. Similar to the velocity field, there is a statistical lower limit of smallest scale of turbulent mixing and maximum frequency in mixing processes. Such smallest scale is called Batchelor scale $L_{\phi B}$ and defined in terms of the Kolmogorov scale and Schmidt number, *Sc*, by [62]

$$\mathrm{L}_{\phi \mathrm{B}} = Sc^{-1/2} L_K , \tag{3.11}$$

Like the Kolmogorov scale in a turbulent flow, the Bachelor scale characterizes the smallest scalar eddies wherein molecular diffusion is balanced by turbulent mixing. For most gases, the Schmidt

number is approximately one, so the smallest scalar lengths are approximately equal to Kolmogorov scale. For liquids, *Sc* can be on the order of 10^3 or greater, so that the scalar field contains much more fine-structures than the velocity field. The scales at which diffusion is occurring are much smaller. Then computational requirements to numerically solve these scales and thus accurately describe the mixing process are correspondingly increased. For scalar eddies much larger than the Batchelor scalar, molecular diffusion is negligible. Thus, initially non-premixed scale fields will remain segregated at scales larger than the Batchelor scale. This has important consequences for turbulent reaction flows because it implies that the chemical source term will be strongly coupled to turbulent mixing for many chemical reactions of practical importance. At high Reynolds numbers, the small scales of scalar field are usually assumed to be nearly isotropic (H.S. Kang & C. Meneveau, 2001 showed that scalar fields at small level are not so isotropic as assumed.) and will evolve on a time scale that is much smaller than that of the large scales. Moreover, for a passive scalar, the characteristic time scales for mixing at length scales above the Batchelor scale will be determined solely by turbulent flow.

The largest structures in the scalar field is also named as scalar integral scale, and is primarily determined by two processes: (1) initial condition — the scalar field can be initialized with a characteristic $L_{\phi I}$ that is completely independent of turbulence field, and (2) turbulent mixing — the energy containing range of a turbulent flow will create "scalar eddies" with characteristic length scalar $L_{\phi I}$ that is approximately equal to L_I. Like the velocity spatial correlation function discussed in section 3.1, the scalar spatial correlation function provides the length scale information about the underlying scalar field. For a homogeneous isotropic and statistical steady (time independent) scalar field, the spatial correlation function can be written in terms of the fluctuating scalar field ϕ' as:

$$R_\phi^L(\Delta x) = \frac{\langle \phi'(x)\phi'(x+\Delta x)\rangle}{\langle \phi'(x)\phi'(x)\rangle}. \tag{3.12}$$

In terms of this function, the scalar integral scale is defined by

$$\mathrm{L}_{\phi I} = \int_0^\infty R_\phi(\Delta x) d(\Delta x). \tag{3.13}$$

and similar to the velocity field, the scalar Taylor microscale is defined by

$$L_{\phi T} = \left(-\frac{1}{2}\frac{\partial^2 R_\phi^L}{\partial(\Delta x)^2}(0) \right)^{-1/2}. \tag{3.14}$$

For homogenous scalar fields, the scalar spectrum is related to the scalar spatial correlation function through the Fourier transform. Figure 3.3 is an example of scalar energy spectrum for a range of Schmidt numbers plotted for *Re=500* [84]. The schematic velocity spectrum is included in the figure for comparison. Analogous to the velocity field, the scalar mixing in inertial convective subrange can be interpreted as a cascade process. The inertial sub-range exhibits the same profile (~5/3) similar to velocity field for moderate Schmidt numbers. For low Schmidt number, the scale spectrum falls off much faster than the velocity spectrum. For high Schmidt number, viscous convective/diffusive subrange (Batchelor spectrum) with (~1) scaling is evident.

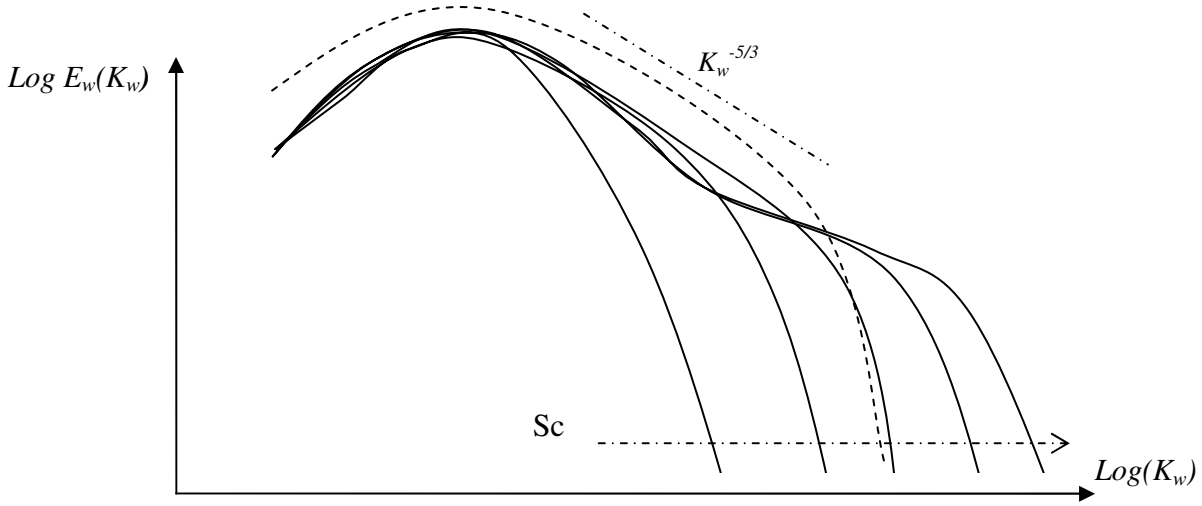

Figure 3.3: Schematic scalar energy spectrum normalized by the integral scales [84]
Schmidt numbers range from $Sc=10^{-4}$ to $Sc=10^{4}$ in powers of 10^{2}
(—scalar --- velocity)

Having defined the model scalar spectrum, this can be now used to compute the scalar mixing time T_ϕ as a function of *Sc*. In the turbulent mixing literatures, the scalar mixing time is usually reported in a dimensionless form referred to as the mechanical-to-scalar time-scale ratio R_ϕ^T, defined by

$$R_\phi^T = \frac{k\varepsilon_\phi}{\varepsilon\left\langle \phi'^2 \right\rangle}, \tag{3.15}$$

and

$$T_\phi = 2\frac{\left\langle \phi'^2 \right\rangle}{\varepsilon_\phi}. \tag{3.16}$$

where ε_ϕ is the scalar dissipation rate and ϕ'^2 is the scalar variance. The question is now how this wide range of scales can be accounted for in modeling and simulation.

3.3 Direct Numerical Simulation

The main purpose of Direct Numerical Simulations (DNS) is to solve (to best of computers ability) for the turbulent variables without the use of "turbulent modeling" by resolving all the scales of turbulence, see Figure 3.4. DNS can be used to compute a specific fluid flow state, to create simplified situations that are not possible in an experimental facility, and to isolate specific phenomena in the transition process. Therefore, DNS is stressed as a research tool with the objective to perform controlled studies that allow better insight, scaling laws, and turbulent models to develop. The earliest use of DNS began in the 1970's and with the growth in the computational power today, it is getting more and more popular day by day. However, the main technical challenges of DNS remain the memory and computational speed requirements. By using equation (3.1), one can derive an expression for the number of grid points required by DNS for an adequate resolution and a three dimensional computation [70]:

$$N_{DNS} = \left(\frac{\text{Characteristic Length}}{\text{Smallest Length Scale}} \right)^3 = \left(\frac{L_c}{L_K} \right)^3 \sim \text{Re}_t^{-9/4}, \tag{3.17}$$

where Re_t is turbulent Reynolds number. A DNS of the flow past a complete airfoil, for example, would require a computer with 1018 flops capacity to be practical, which is still not available now. The instantaneous range of scales in turbulent flows increases rapidly with the Reynolds number and hence most practical engineering problems have too wide range of scales to be directly computed using DNS. This makes the application of DNS possible only for relatively low Reynolds number flows and simple geometries of any relevance in engineering or industrial applications.

3.4 Reynolds Averaging Based Numerical Simulation

To face the difficulties in DNS, Reynolds averaging based Numerical Simulation (here RANS) method is based on the statistically averaged governing equations with appropriate turbulence models. By using the Reynolds' averaging, any instant value of flow parameter Φ is represented by

the mean value $\langle\Phi\rangle$, and a fluctuating part, Φ' as:

$$\Phi(x_i,t)=\langle\Phi(x_i,t)\rangle+\Phi'(x_i,t)\,. \tag{3.18}$$

The long-time average of a quantity Φ is defined by

$$\langle\Phi(x_i,t)\rangle=\langle\Phi(x_i)\rangle=\frac{1}{t_1}\int_0^{t_1}\Phi(t,x_i)\,dt\,, \tag{3.19}$$

where t_1 is a time interval much longer than all the time scales of the turbulent flow. Note that the mean value can also be obtained by an ensemble averaging more appropriate for unsteady flow processes. Thus,

$$\langle\Phi(x_i,t)\rangle=\frac{1}{N}\sum_{n=1}^{N}\Phi_n(x_i,t)\,, \tag{3.20}$$

where N is large number of experiments with same inlet and outlet conditions. If the averaging operation is applied to the governing equations, one obtains:

$$\frac{\partial\langle\rho\rangle}{\partial t}+\frac{\partial\langle\rho\rangle\langle u_i\rangle}{\partial x_i}=0\,, \tag{3.21}$$

$$\frac{\partial\langle\rho\rangle\langle u_i\rangle}{\partial t}+\frac{\partial\langle\rho\rangle\langle u_i\rangle\langle u_j\rangle}{\partial x_j}=-\frac{\partial\langle p\rangle}{\partial x_i}+\frac{\partial\langle\tau_{ij}\rangle}{\partial x_i}-\frac{\partial\langle\rho\rangle\langle u_i'u_j'\rangle}{\partial x_j}+\langle\rho\rangle g_i\,, \tag{3.22}$$

$$\frac{\partial\langle\rho\rangle\langle f\rangle}{\partial t}+\frac{\partial\langle\rho\rangle\langle u_i\rangle\langle f\rangle}{\partial x_i}=\frac{\partial}{\partial x_i}\left(\langle\rho\rangle D_f\frac{\partial\langle f\rangle}{\partial x_i}\right)-\frac{\partial\langle\rho\rangle\langle u_i' f'\rangle}{\partial x_i}\,, \tag{3.23}$$

The averaging process obviously leads to a loss of some information contained in the instantaneous equations and corresponding new unknown terms appear. This lack of information can be overcome by means of approximations of those unknown terms (i.e. the turbulent stresses tensor (or Reynolds tensor) $\langle u_i'u_j'\rangle$ and turbulent flux $\langle u_i'f'\rangle$) as a function of the averaged variables (closure problem). The approximations or models used in the closure problem must be as general and accurate as possible so as to be able to model different turbulent phenomena. Different procedures used to handle the closure problem lead to different RANS turbulent models, such as:

- Differential Reynolds Stress models, where a differential equation for each unknown is derived;
- Algebraic Reynolds Stress models, which convert the differential equations to algebraic equations;
- Eddy Viscosity models, where a turbulent viscosity is defined and postulated in addition to

the molecular one.

The recently developed higher order models can be found in K. Hanjalic 2005.

The main limitation of this approach is that RANS provides only limited information about the flow and all the information of turbulence is modeled (see Figure 3.4), which brings a high challenge on modeling. Even for time-accurate simulations of unsteady flows, the RANS simulations are designed to include only the largest flow structures (those that scale with the dominant flow-length/time scale) in the flow and the smaller scales are not included. The extent to which the absence of the smaller flow structures affects the prediction of the larger vortex structures is quite open question in this framework. This problem is however configuration dependent and usually cannot be judged a priori.

3.5 Large Eddy Simulation

As pointed out in S. Pope 2000 and R.O. Fox 2003, at high Reynolds number, over 99 percentage of the computational expense of DNS is used to resolve the dissipation range of the turbulent energy spectrum. However, the energy-containing scales determine most of the flow-dependent transport properties. Thus, in this way, DNS wastes most of the computational effort on resolving scales that are not very important for determining second order quantities such as the Reynolds stresses and the scalar flux components.

Large-eddy simulation (LES) is a technique intermediate between the direct simulation of turbulent flows (with no model) and the solution of the Reynolds-averaged equations (where all the structures of the turbulence are modeled). In LES the contribution of the large, energy-carrying structures is computed exactly, and only the effect of the small scales of turbulence is modeled through subgrid scale (SGS) models. The idea of LES is based on the understanding of the turbulent scales characteristics which, in general, can be summarized in the Table 3.1.

This shows that the large scales are difficult to model and the universal model is impossible, while the small scales tend to be more homogeneous and universal, and less affected by the boundary conditions than the large ones. There is hope that their models can be simpler and require fewer adjustments when applied to different flows than similar models for the RANS.

Due to the consideration of advanced models, which allowed more accurate computations to be performed with less empiricism than before, LES is now being used not only to calculate standard, well-documented test cases, but also to study the physical phenomena that occur in more complex,

engineering-like applications, at Reynolds numbers that could not be reached by DNS. The resolution degree of the turbulent scales with respect to the energy spectrum of the velocity and scalar (when Sc~1) for the three methods (DNS, RANS and LES) is depicted in Figure 3.4.

Large scales	Small scales
■ generated by the mean flow	■ produced by large eddies
■ strongly depending on the flow configuration considered and its boundary conditions	■ almost universal (not the case for scalar)
■ ordered (coherent structures)	■ random
■ inhomogeneous and anisotropic	■ almost homogeneous and isotropic (not the case for scalar)
■ long-living	■ short-living
■ high energy content	■ low energy content
■ diffusive	■ dissipative

Table 3.1: Characters of large scales and small scales of turbulence

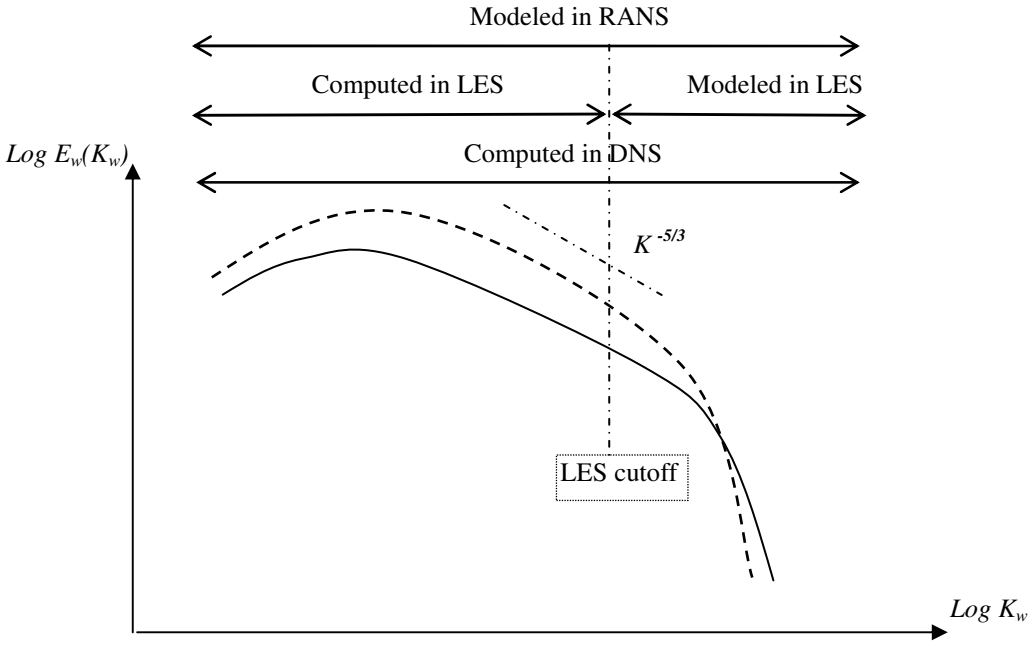

Figure 3.4: Turbulent scales resolved/modeled by RANS, LES, and DNS

(—scalar ---velocity)

The computational effort required by LES can be estimated considering that the smallest resolved scale has to be situated in the inertial subrange of turbulent kinetic energy spectrum, where the effect of SGS is expected to be problem-independent. A measure of these scales is the Taylor microscale. The number of grid points needs to be resolved in three dimensions can be expressed as [70]:

$$N_{LES} \sim \left(\frac{L_c}{L_T} \right)^3 \sim \mathrm{Re}_t^{3/2}. \tag{3.24}$$

This is much less than in the case of DNS. Thus, to maximize the returns, LES should be applied to problems in which its cost is comparable to that of the solution of the RANS equations, or to problems in which lower-level turbulence models fail. Such problems include unsteady or three-dimensional boundary layers, separated flows and flows involving unsteady mixing processes. For mixing processes in which passive scalar fields have to be computed, the requirement of grid points is similar to the one in velocity field when the gas phase flows (Sc~1) are considered.

A detailed presentation of different issues of LES [102] is beyond the scope of this thesis. However, the basis idea of LES formulation will be outlined in the next chapter which deals in detail with the modeling of the SGS stress tensor and scalar flux vector.

Chapter 4
Large Eddy Simulation (LES) of Scalar Mixing

In this chapter, the present state of the classical Large Eddy Simulation (LES) technique is discussed. Modeling issues that are under study will be described to highlight the response of the subgrid scale (SGS) models to important features of the resolved field. A state-of –the-art study of SGS scalar flux models is presented to introduce the new developed anisotropy SGS scalar flux model. Applications are subsequently treated in Chapter 6 and 7.

4.1 Classical LES Formulation

There are different formulations of LES in the literatures (e.g. [91] and [100]). In this work, we focus on the so called classical LES approach based on the filtering operations.

4.1.1 Filtering Operation

In LES [4], the entire field variables $\Phi(x_i,t)$ are decomposed into resolved and SGS parts. This is done by low pass filtering the governing equations with a filtering function *G*. This filter removes all the finer fluctuations, so that the governing equations only describe the space-averaged fields. The filtered field $\overline{\Phi}$ is determined by convolution with filter. As a result, the product of the local filter and field are averaged in space with

$$\overline{\Phi(x_i,t)} = \iiint_{-\infty}^{\infty} \Phi(x_i - x_i')G(x_i')dx_1'dx_2'dx_3'. \tag{4.1}$$

The difference between the filtered values and its unfiltered value is called fine structure contribution, small scale portion or SGS portion Φ' following

$$\Phi - \overline{\Phi} = \Phi' \Leftrightarrow \Phi = \overline{\Phi} + \Phi' . \tag{4.2}$$

For example, one typical filter function is a rectangle (top-hat filter) of the widths three Δ_i, which is defined by

$$G(x_i - x_i') = \begin{cases} \prod_{i=1}^{3} \frac{1}{\Delta_i} : & |x_i'| \le \frac{\Delta_i}{2} \\ 0 : & |x_i'| > \frac{\Delta_i}{2} \end{cases} . \tag{4.3}$$

In general, any low pass filter can be chosen for LES, although only some make sense. Filtering of the governing equations results in unclosed terms that need to be modeled. Although constant density flows are being investigated in this work, let's mention that for the density variable flows, it is recommendable to apply a Favre (density-weighted) decomposition

$$\Phi = \tilde{\Phi} + \Phi', \tag{4.4}$$

where

$$\tilde{\Phi} = \frac{\overline{\rho\Phi}}{\overline{\rho}} . \tag{4.5}$$

Schumann Filtering: In LES, a special filter may be used to simplify the further proceeding. The Schumann filter is a top hat filter on the cubic base of the local mesh cell having a filter width Δ_i that is identical to the size of the cell. With finite volume discretization, this concept of implicit filtering (Schumann Filtering) will reduce the effort to make a DNS code suited for LES code by adding some additional terms to the governing equations.

With Schumann filtering, the integration interval in equation can be narrowed to the interval of $-\Delta x_i / 2 \le x_i' \le \Delta x_i / 2$. With the substitutions $x_i^- = -\Delta x_i / 2$ and $x_i^+ = \Delta x_i / 2$, as well as the filter out of the integral, we obtain

$$\overline{\Phi(x_i, t)} = \left(\prod_{k=1}^{3} \frac{1}{\Delta x_k} \right) \int_{x_3^-}^{x_3^+} \int_{x_2^-}^{x_2^+} \int_{x_1^-}^{x_1^+} \Phi(x_i - x_i') dx_1' dx_2' dx_3' . \tag{4.6}$$

In this equation, the product in front of the integral is just the inverse volume of the local CFD cell.

4.1.2 Filtered Governing Equations

According to the above decompositions, the LES equations for the resolved fields are formally derived by subjecting the governing equations to the filter (Schumann Filtering is implied in the

denotation). The instantaneous small-scale contributions are removed by the filter, but their effects remain in unclosed residual terms representing the influence of the subgrid scales on the resolved scales. Detail derivations can refer to [4]. Applying this procedure to the governing equations, LES filtered equations are obtained for a general density variable case as:

$$\frac{\partial \overline{\rho}}{\partial t}+\frac{\partial \overline{\rho}\tilde{u}_i}{\partial x_i}=0, \tag{4.7}$$

$$\frac{\partial}{\partial t}(\overline{\rho}\tilde{u}_i)+\frac{\partial}{\partial x_j}(\overline{\rho}\tilde{u}_i\tilde{u}_j)=\frac{\partial}{\partial x_j}\left[\overline{\rho}\tilde{\nu}\left(\frac{\partial \tilde{u}_i}{\partial x_j}+\frac{\partial \tilde{u}_j}{\partial x_i}\right)-\frac{2}{3}\overline{\rho}\tilde{\nu}\frac{\partial \tilde{u}_k}{\partial x_k}\delta_{ij}-\overline{\rho}\tau_{ij}^{sgs}\right]-\frac{\partial \overline{p}}{\partial x_i}+\overline{\rho}\,g_i, \tag{4.8}$$

and

$$\frac{\partial}{\partial t}\overline{\rho}\tilde{f}+\frac{\partial}{\partial x_i}\left(\overline{\rho}\tilde{u}_i\tilde{f}\right)=\frac{\partial}{\partial x_i}\left(\overline{\rho}D_f\frac{\partial \tilde{f}}{\partial x_i}\right)-\frac{\partial}{\partial x_i}\left(\overline{\rho}J_i^{sgs}\right). \tag{4.9}$$

These equations govern the evolution of the large, energy-carrying, scales of motion. In the flow field, the effect of the small scales appears through

$$\text{SGS stress: } \tau_{ij}^{SGS}=\widetilde{u_iu_j}-\tilde{u}_i\tilde{u}_j, \tag{4.10}$$

and in scalar field through

$$\text{SGS Scalar Flux: } J_i^{SGS}=\widetilde{u_if}-\tilde{u}_i\tilde{f}, \tag{4.11}$$

that must be molded.

The subgrid kinetic energy k^{SGS} is defined as $k^{SGS}=\left(\widetilde{u_iu_i}-\tilde{u}_i\tilde{u}_i\right)\big/2$. Dealing with passive scalar, it is necessary to introduce, analogously to k^{SGS}, the subgrid "scalar energy" also referred as the SGS scalar variance [73]. It is defined as:

$$\theta_\phi=\widetilde{ff}-\tilde{f}\tilde{f}. \tag{4.12}$$

The scalar variance in turn observes the transport equation

$$\begin{aligned}\frac{\partial}{\partial t}\theta_\phi+\frac{\partial}{\partial x_i}\left(\tilde{u}_i\theta_\phi\right)-\frac{\partial}{\partial x_i}\left(D\frac{\partial \theta_\phi}{\partial x_i}\right)=&\\ \underbrace{-\frac{\partial}{\partial x_i}\left(\widetilde{u_if^2}-\tilde{u}_i\tilde{f}^2\right)}_{1}&\underbrace{-2D\widetilde{\frac{\partial f}{\partial x_i}\frac{\partial f}{\partial x_i}}}_{2}+2D\frac{\partial \tilde{f}}{\partial x_i}\frac{\partial \tilde{f}}{\partial x_i}+\underbrace{2\frac{\partial}{\partial x_i}\left(\tilde{f}\,J_i^{sgs}\right)}_{3}-\underbrace{2J_i^{sgs}\frac{\partial \tilde{f}}{\partial x_i}}_{4}.\end{aligned} \tag{4.13}$$

The four unclosed terms represent turbulent convection of scalar (term 1), SGS dissipation of scalar (term 2), large scale diffusion (term 3) and production of θ_ϕ at large scales (term 4). Terms 3 and 4 can be closed by using SGS scalar flux models. Term 1 can be closed by using a series expansion or

an appropriate model. The SGS scalar dissipation (term 2) defined as

$$\varepsilon_{\phi}^{SGS} = 2D\widetilde{\frac{\partial f}{\partial x_i}\frac{\partial f}{\partial x_i}}, \tag{4.14}$$

which requires an additional model.

The SGS scalar dissipation modeling is not an issue in this work. It will be nevertheless needed for determination of the scalar mixing as introduced in Chapter 3. The section below therefore will only focus on SGS models both in the velocity and scalar field.

4.2 SGS Stress τ_{ij}^{SGS} Models

The SGS stress, see equation (4.10), accounts for the unresolved scales that are filtered out and it can be decomposed as [100]:

$$\tau_{ij}^{SGS} = \widetilde{u_i u_j} - \tilde{u}_i\tilde{u}_j = L_{ij}^{v} + C_{ij}^{v} + R_{ij}^{v}, \tag{4.15}$$

where

$$L_{ij}^{v} = \widetilde{\tilde{u}_i\tilde{u}_j} - \tilde{u}_i\tilde{u}_j, C_{ij}^{v} = \widetilde{\tilde{u}_i u_j'} - \widetilde{u_i'\tilde{u}_j}, \quad R_{ij}^{v} = \widetilde{u_i' u_j'}. \tag{4.16}$$

L_{ij}^{V} is the Leonard stress, C_{ij}^{v} is the cross term and R_{ij}^{v} is the SGS Reynolds stress. The Leonard stresses represent interactions between resolved scales that result in subgrid-scale contributions; they can be computed explicitly. The cross terms represent interactions between resolved and unresolved scales, whereas the SGS Reynolds stresses represent interactions between small, unresolved scales. The subgrid-scale cross and Reynolds-stresses need to be modeled. To develop SGS models, some guidance has been provided in the past by approaches traditionally used in modeling of the Reynolds stresses. In the following classical SGS stress models will be outlined, which assume that the influence of the small structures can be described as a function of the large scale quantities.

The simplest class of models consists of the linear models, which are based on the eddy viscosity approach. A very common model is the one developed by J. Smagorinsky in 1963. It is very simple and shows good numerical properties, however, it tends to dissipate too much turbulent kinetic energy. Another popular model is the Bardina model (J. Bardina, 1980). This scale similarity based model yields accurate SGS stresses. However Bardina's model does not dissipate sufficient turbulent kinetic energy, so simulation tends to be unstable. To overcome this problem, the model has often been combined with the Smagorinsky model, which leads to mixed model.

All the models mentioned here are scaled by a model parameter. However, the ideal values of this

parameter depend on the configuration and on the location in the flow. A recent development is that of the dynamic procedure originating from M. Germano 1991 and D. Lilly 1992, which can be used to automatically determine e.g. the Smagorinsky suited model parameter. The resulting approach is often referred to as Germano model (or dynamic procedure).

A further class of models comprises the nonlinear models. Algebraic stress models have been proposed by C. Speziale 1997 and B. Kosovic 1997. However, these models are too complex to match the elegance and simplicity of LES theory.

Within this framework, a very powerful approach for the modeling of the SGS stress τ_{ij}^{SGS} is to solve a transport equation for the turbulent kinetic energy, k^{SGS}. This has been suggested by A. Yoshizawa et al. 1982 and has been applied very effectively by S. Menon et al. 1996.

Eddy Viscosity Approach

The eddy viscosity approach is based on the assumption that small scale turbulence affects the flow in the same way as the molecular viscosity. Therefore, the fine structure term τ_{ij}^{SGS} may be modeled by adding a turbulent viscosity ν_t to the molecular viscosity ν, resulting in an effective viscosity $\nu_{ef} = \nu_t + \nu$.

Adding the turbulent viscosity ν_t model the SGS stress in the filtered Navier-Stokes equation corresponds to applying the following model

$$\tau_{ij}^{SGS} = -\upsilon_t \left(\frac{\partial \tilde{u}_j}{\partial x_i} + \frac{\partial \tilde{u}_i}{\partial x_j} \right) + \frac{2}{3} \upsilon_t \frac{\partial \tilde{u}_\kappa}{\partial x_\kappa} \delta_{ij} + \frac{2}{3} k^{SGS} \delta_{ij}, \tag{4.17}$$

where the tensor τ_{ij}^{SGS} has been decomposed in a deviatoric part and a isotropic part.

This work relies on a pressure correction scheme to determine the value of the pressure so that the equation of continuity is satisfied. This pressure correction is able to compute the sum of the pressure and the trace-term of the stress-tensor. Therefore, the pressure-parameter $\overline{P}$ is introduced as:

$$\overline{P} = \overline{p} - \frac{1}{3} \overline{\rho} \tau_{kk}^{SGS}. \tag{4.18}$$

One should be aware that solving equation (4.20) will only yield that the pressure parameter $\overline{P}$, while the physical pressure $\overline{p}$ remains unknown.

The filtered Navier-Stokes equation becomes

$$\frac{\partial}{\partial t}(\bar{\rho}\tilde{u}_i)+\frac{\partial}{\partial x_j}(\bar{\rho}\tilde{u}_i\tilde{u}_j)=\frac{\partial}{\partial x_j}\left[\bar{\rho}\tilde{\nu}_{ef}\left(\frac{\partial \tilde{u}_i}{\partial x_j}+\frac{\partial \tilde{u}_j}{\partial x_i}\right)-\frac{2}{3}\bar{\rho}\tilde{\nu}_{ef}\frac{\partial \tilde{u}_k}{\partial x_k}\delta_{ij}\right]-\frac{1}{3}\frac{\partial}{\partial x_i}\bar{\rho}\tau_{ij}^{sgs}+\frac{\partial \bar{p}}{\partial x_i}+\bar{\rho}\,g_i\,. \quad (4.19)$$

With the substitution equation (4.18), equation (4.19) becomes

$$\frac{\partial}{\partial t}(\bar{\rho}\tilde{u}_i)+\frac{\partial}{\partial x_j}(\bar{\rho}\tilde{u}_i\tilde{u}_j)=\frac{\partial}{\partial x_j}\left[\bar{\rho}\tilde{\nu}_{ef}\left(\frac{\partial \tilde{u}_i}{\partial x_j}+\frac{\partial \tilde{u}_j}{\partial x_i}\right)-\frac{2}{3}\bar{\rho}\tilde{\nu}_{ef}\frac{\partial \tilde{u}_k}{\partial x_k}\delta_{ij}\right]+\frac{\partial \bar{P}}{\partial x_i}+\bar{\rho}\,g_i\,. \quad (4.20)$$

k^{SGS} ($k^{SGS}=1/3\tau_{kk}^{SGS}$) can be described either by Lilly method or by a transport equation as:

$$\frac{\partial k^{SGS}}{\partial t}+\frac{\partial \tilde{u}_i k^{SGS}}{\partial x_i}=\underbrace{-\frac{\tau_{ij}^{SGS}\partial \tilde{u}_i}{\partial x_j}}_{production}\underbrace{-\frac{\partial}{\partial x_j}\left(\frac{1}{2}\widetilde{u_i'u_i'u_j'}+\frac{1}{\rho}\widetilde{p'u_j'}\right)+\nu\frac{\partial^2 k^{SGS}}{\partial x_i^{\,2}}}_{diffusion}\underbrace{-\nu\left(\widetilde{\frac{\partial u_i'}{\partial x_i}\frac{\partial u_j'}{\partial x_j}}\right)}_{dissipation}. \quad (4.21)$$

Smagorinsky Model

To solve the momentum equation (4.20), a model providing an approximation for the turbulent viscosity υ_t is needed. As mentioned before, Smagorinsky proposed the postulation

$$\nu_t=\left(C_{sm}\Delta\right)^2\left|\tilde{S}\right| \quad \text{with} \quad \left|\tilde{S}\right|=\left(2\tilde{S}_{ij}\tilde{S}_{ij}\right)^{\frac{1}{2}}. \quad (4.22)$$

where Δ is the filter width and C_{sm} is model coefficient. The model relates the eddy viscosity to the large-scale strain-rate tensor

$$\tilde{S}_{ij}=\frac{1}{2}\left(\frac{\partial \tilde{u}_i}{\partial x_j}+\frac{\partial \tilde{u}_j}{\partial x_i}\right). \quad (4.23)$$

This model uses a typical length scale $C_{sm}\Delta$ and a typical time scale (determined by the contraction of the deformation velocity tensor) to compute the turbulent viscosity. The length scale is chosen proportional to the local cell width, which is coherent with the idea that only the unresolved structures are to be modeled. One of the model's main drawbacks is the strong deviation of the model constant. Lilly showed the model to be consistent with the Kolmogorov spectrum if the correct model coefficient, *0.173* [27], is chosen. The value of C_{sm} mainly depends on the region of the flow field: e.g. in the center of a channel, C_{sm} = *0.2* is known to be reasonable, whereas in the vicinity of a wall, C_{sm} should be reduced to *0.065*. This can be achieved with the damping function by E. van Driest, 1956. However, van Driest damping is not possible in complex configurations. A truly desirable approach would automatically determine the correct parameter for each location of

the flow field, as the dynamic procedure.

Dynamic Procedure

To avoid the model coefficient choose for every flow, Germano proposed a dynamic procedure for the calculation of the model coefficient. In dynamic models, the coefficient of the model is determined as the calculation processes, rather than input a priori as in the standard Smagorinsky model. This is accomplished by defining a test filter (denoted by a caret) whose width $\hat{\Delta}$ is larger than the grid filter-width Δ (typically, $\hat{\Delta} = 2\Delta$). Dynamic adjustment of the model coefficients is based on the identity [100]

$$B_{ij} = \widehat{\widetilde{u_i u_j}} - \hat{\tilde{u}}_i \hat{\tilde{u}}_j = T_{ij} - \widehat{\tau_{ij}^{SGS}} \,, \tag{4.24}$$

which relates the "resolved turbulent stresses" B_{ij} (the contribution from the region between test-filter and grid-filter scale), the SGS stresses τ_{ij}^{SGS} and the subtest stresses $T_{ij} = \widehat{\widetilde{u_i u_j}} - \hat{\tilde{u}}_i \hat{\tilde{u}}_j$, which are obtained by applying the test filter of characteristic width $\hat{\Delta}$, to the filtered Navier-Stokes equation.

Consider now an eddy viscosity model to parameterize both subgrid and subtest stresses, of the form (Υ_{ij} and γ_{ij} following equation (4.17) and (4.22) with test-filter and grid-filter)

$$T_{ij} = -2C_{dy}\Upsilon_{ij} \text{ and } \tau_{ij}^{SGS} = -2C_{dy}\gamma_{ij} \,. \tag{4.25}$$

Upon substituting equation (4.25) into equation (4.24), the identity can be satisfied only approximately, since the stresses are replaced by modeling assumptions, and the system is overdetermined (five independent equations are available to determine a single coefficient). Lilly [28] proposed that the error incurred when a single coefficient is used be minimized in a least-squares sense. The error is

$$e_{ij} = B_{ij} - T_{ij} + \widehat{\tau_{ij}} = B_{ij} + 2C_{dy}M_{ij} \,, \tag{4.26}$$

with $M_{ij} = \Upsilon_{ij} - \widehat{\gamma_{ij}}$ .The least-squares minimization procedure requires

$$\frac{\partial \langle e_{ij} e_{ij} \rangle}{\partial C_{dy}} = 2\left\langle e_{ij} \frac{\partial e_{ij}}{\partial C_{dy}} \right\rangle = 0 \,, \tag{4.27}$$

where the brackets indicate an appropriate ensemble average. This implies

$$\left\langle \left(B_{ij} + 2C_{dy} M_{ij} \right) M_{ij} \right\rangle = 0, \tag{4.28}$$

which gives

$$C_{dy} = -\frac{1}{2} \frac{B_{ij} M_{ij}}{M_{ij} M_{ij}}. \tag{4.29}$$

In general, an eddy viscosity form model is adequate for approximating the interaction between given turbulent scales and distinctly smaller scales, in which the main function of the SGS is to remove energy from the grid scale, but it is inadequate for representing the backward scatter of SGS energy into the grid scale. Another drawback is the alignment of τ_{ij}^{SGS} and $\tilde{S}_{ij}$ which is not confirmed experimentally [50]. All Smagorinsky based models also assume the equilibrium between production and dissipation of kinetic energy in small scales which is difficult to be met in complex configurations. Nevertheless, they appear to be satisfactorily implemented in a number of engineering flows. To overcome the shortcomings, related to the "alignment" assumption in these models, the so called scale similarity based models, the nonlinear gradient model have been suggested.

Scale Similarity Model

An alternative SGS model for the eddy viscosity model is the scale-similarity model which is based on the hypothesis that the smallest grid scale and the largest SGS are similar. Scale-similarity models employ multiple filtering operations to identify the smallest resolved scales as:

$$\tau_{ij}^{SGS} = C_{ss} \left(\widehat{\tilde{u}_i \tilde{u}_j} - \hat{\tilde{u}}_i \hat{\tilde{u}}_j \right), \tag{4.30}$$

where C_{ss} is model is coefficient. This model has been shown to be the most active in the interaction with the unresolved subgrid scales. They can provide backscatter in a numerically stable and physically realistic manner, and predict SGS stresses in regions that are well correlated with the locations where large Reynolds stress occurs. There are many modifications of scalar similarity model (e.g. [11] and [38]). For example, the mixed models include an eddy-viscosity part as well as a scale-similar contribution in order to overcome the drawback inherent to the scalar similarity model, which is that the predicted magnitude of the backward scatter contribution is larger than the exact DNS predicted value [34].

Besides these classical models mentioned above, the new developed models tried to overcome the "local equilibrium" assumption. For this end one equation model and anisotropy model try to model

the unclosed term in more physically consistent way. Second order SGS models have also been proposed, (see C. Fureby et al. 1997, L. Davidson 1997 and K. Horiuti 1993). However, because of difficulties of implementation and cost on computation, these higher order models didn't gain wide applications. A recent overview on SGS stress tensor modeling can be found in C. Meneveau & J. Katz 2000.

4.3 SGS Scalar Flux J_i^{SGS} Models

The focus of this work is to accurately represent the SGS term in scalar field. The SGS scalar flux $J_i^{SGS} = \widetilde{u_i f} - \tilde{u}_i \tilde{f}$ represents the contribution of the small scales (smaller than the filter scale) to the total transport and it will be parameterized as a function of the resolved field.

4.3.1 Known Models

Traditional Eddy Diffusivity SGS Model

According to standard gradient diffusion hypothesis, eddy diffusivity models (T. Eidson, 1985) parameterize the SGS fluxes that are being proportional to the resolved scalar gradient, equation (4.31). Their simplicity has made them most popular since the eddy viscosity assumption was first introduced by Smagorinsky 1963.

$$J_i^{SGS} = -D_{ed} \frac{\partial \overline{f}}{\partial x_i}, \tag{4.31}$$

where D_{ed} is the model coefficient (turbulent diffusivity). It is related to the turbulent viscosity by Schmidt/Prandtl number Sc_t as:

$$D_{ed} = \frac{\upsilon_t}{Sc_t}. \tag{4.32}$$

Since the turbulent viscosity is related to velocity field, here the value of turbulent Schmidt number must be defined. Most of previous works (e.g. B. Wegner, 2004) kept this parameter as a constant value. For air flow, experiment has shown that typical values of the turbulent Schmidt number should be $Sc_t \sim 0.5 - 0.7$ and most accepted value is 0.7, while for the water flow, a constant turbulent Schmidt number is hard to be achieved.

Eddy Diffusivity SGS Model with Dynamic Procedure

Analogous to the so called dynamic procedure (M. Germano et al. 1991), D. Lilly 1992 used information from the resolved scalar field to optimize the value of the free parameter as a function of time and position. The turbulent Schmidt number can therefore be calculated by applying a test filter with filter width $\hat{\Delta}$. The dynamic procedure in scalar field following the same procedure as in velocity field (Section 4.2) results in the turbulent Schmidt number computed as:

$$\frac{1}{Sc_t} = \frac{1}{2C_{dy}} \frac{F_i H_i}{H_i H_i} = \frac{M_{ij} M_{ij}}{B_{ij} M_{ij}} \frac{F_i H_i}{H_i H_i}, \tag{4.33}$$

where

$$H_i = \widehat{\Delta^2 \left|\tilde{S}\right| \frac{\partial \tilde{f}}{dx_i}} - \hat{\Delta}^2 \left|\hat{\tilde{S}}\right| \frac{\partial \hat{\tilde{f}}}{dx_i} \quad \text{and} \quad F_i = \widehat{\tilde{u}_i \tilde{f}} - \hat{\tilde{u}}_i \hat{\tilde{f}} \,. \tag{4.34}$$

Although successfully implemented in a number of engineering flows (see e.g. W. Cabot & P. Moin 1993), the application of the dynamic procedure in scalar field has not yet become common. Furthermore the scale similarity assumption used in the formulation of dynamic procedure becomes more and more questionable. F. Porté-Agel et al. 1998 have proposed a generalized scale-dependent dynamic procedure and compared it to the traditional dynamic models in LES. The result was encouraging.

In this work, a classical dynamic procedure is implemented to calculate the turbulent Schmidt number in various configurations. As an example to demonstrate the variation of Sc_t within a simple flow configuration, Figure 4.1 presents the instant results of the turbulent Schmidt number with the dynamic procedure. The computation is carried out in a counter flow configuration [3]. The sampling position is on the mixing layer where two flows encounter and begin to mix. Just from the results presented in the figure, the turbulent Schmidt number varies throughout positions, where the mean value may be around *0.7* for this configuration (with gas).

The gradient assumption (or isotropic eddy diffusivity assumption) has the same disadvantages as the Boussinesq approximation for flow field. So, such an eddy-diffusivity model is not able to predict realistic values of all components of the scalar flux, since it assumes the SGS scalar flux to be aligned with the resolved scalar gradient. This may be valid if the scalar flux vector is collinear to the scalar gradient. The model is regarded as being fully dissipative (the scalar variance at the filter scales can only be dissipated by the subgrid scales).

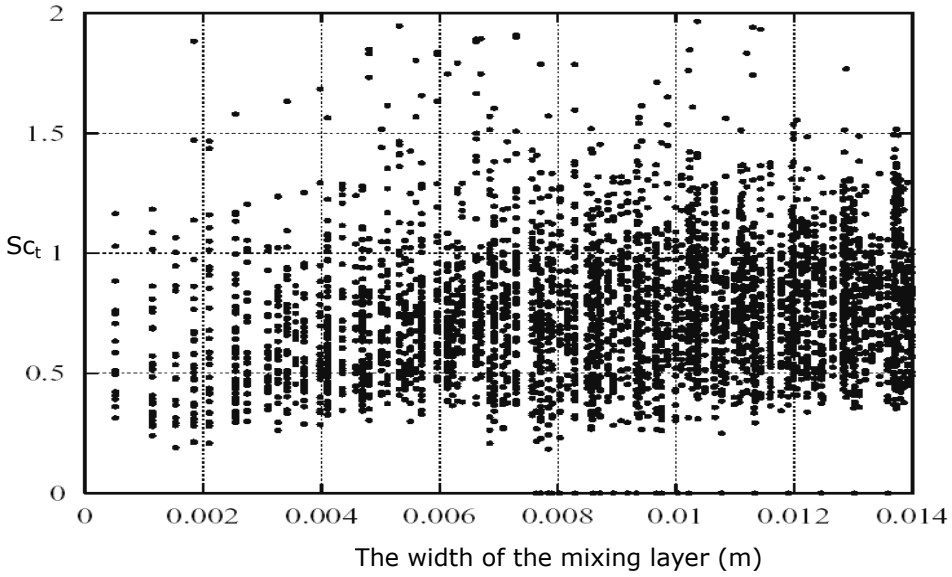

Figure 4.1: Turbulent Schmidt/Prandtl number on the mixing layer of a counter flow configuration calculated by a Dynamical Procedure

Scale Similarity Model

The similarity idea was originally developed for flow field. Applied to scalar field, the SGS contribution is assumed to be similar, in position and order of magnitude, to the contribution evaluated at the resolved quantities. The procedure is as following. A test filtering operation is introduced with filter size $\hat{\Delta}$. Based on the assumption of scale invariance, the SGS scalar flux is proportional to the flux on the test filter level as:

$$J_i^{SGS} = D_{ss}\left(\widehat{\tilde{u}_i\tilde{f}} - \hat{\tilde{u}}_i\hat{\tilde{f}}\right). \tag{4.35}$$

D_{ss} is an model coefficient, which can be a constant depending on configurations or calculated by a dynamic procedure as well. The improvement on this SGS models mostly focuses on the choice of test filters and the modification on the model coefficient. Some test simulations (e.g. reviewed in [35]) complained that the similarity model alone does not dissipate enough scalar variance and typically leads to inaccurate results. Therefore, "mixed models" are developed with a combination of the eddy diffusivity model.

Mixed Model

F. A. Jaberi, 2003 used a priori assessment and indicated a well implemented "mixed model"

$$J_i^{SGS} = D_{ed}\frac{\partial \overline{f}}{\partial x_i} + D_{ss}\left(\widehat{\tilde{u}_i \tilde{f}} - \hat{\tilde{u}}_i \hat{\tilde{f}}\right), \tag{4.36}$$

is closer to ''true'' values than those obtained by the dynamic-diffusivity model.

To simplify, most simulations choose the coefficient of the scale similarity part as one [73]. The model is therefore called as mixed, one parameter model as:

$$J_i^{SGS} = D_{ed}\frac{\partial \overline{f}}{\partial x_i} + \left(\widehat{\tilde{u}_i \tilde{f}} - \hat{\tilde{u}}_i \hat{\tilde{f}}\right). \tag{4.37}$$

All the models mentioned above are isotropic models. The modeled SGS scalar flux in the *i*th direction is proportional to the derivative of the resolved scalar in that direction. However, the new research findings notice that the skewnesses of scalar increments (and derivatives) are inherently anisotropic quantities, and are not suitable indicators of the tendency towards isotropy (H.S. Kang 2001). With regard to the scalar flux transport, various models have been proposed including the probability function, the linear eddy model and diverse algebraic models as reviewed in Chapter 1. Focus on the latter, new models have been suggested besides the linear eddy diffusivity model going from the serial decomposition closures and nonlinear gradient models to the one equation transport model. For complex configurations, this work draws therefore the attention on describing the SGS scalar fluxes with anisotropic behavior and the new developed models are inclined to anisotropic forms.

4.3.2 Anisotropy Based Models

Nonlinear Model

It is well known that the generation of turbulent energy is essentially accomplished through large scales. The energy is then transferred in a cascade manner to the smaller and ever smaller scales and eventually dissipated by the smallest structures of Kolmogorov scales, see Chapter 3. In LES, we assume to have the filtering cutoff in the inertial subrange of energy spectra. The SGS scale itself would neither generate nor destroy but transfers (forward and backward) turbulent kinetic energy. Turning to turbulent scalar fluxes, analogous interchanges exist between the large and small scales.

The transport equation for the SGS scalar flux can be symbolically written as [86]:

$$\frac{\partial J_i^{SGS}}{\partial t}+\frac{\partial \tilde{u}_j J_i^{SGS}}{\partial x_j}=\mathrm{P}_{i\phi}+D_{i\phi}+D^{\nu}{}_{i\phi}+D^{\mathrm{P}}{}_{i\phi}-\varepsilon_{i\phi}^{\nu}, \tag{4.38}$$

where the right-hand side includes subsequently the shear production, the SGS diffusion, the viscous diffusion, the pressure transport and viscous dissipation. The production term in the transport equation takes the following form

$$\mathrm{P}_{i\phi}=J_j^{SGS}\frac{\partial \tilde{u}_i}{\partial x_j}+\tau_{ij}^{SGS}\frac{\partial \tilde{f}}{\partial x_j}. \tag{4.39}$$

Unlike in the RANS transport equation for turbulent scalar fluxes, the production term for the SGS scalar fluxes, $\Psi_{i\phi}^{SGS}\sim \mathrm{P}_{i\phi}$, represents actually the SGS scalar fluxes dissipation. If $J_i^{SGS}>0$, this SGS dissipation indicates the net scalar fluxes exchange of forwards ($\Psi_{i\phi}^{SGS}>0$) and backwards ($\Psi_{i\phi}^{SGS}<0$) transfer between resolved large-scale and SGS scalar structures. If $J_i^{SGS}<0$, forward (backward) transfer corresponds to $\Psi_{i\phi}^{SGS}<0$ ($\Psi_{i\phi}^{SGS}>0$).

It is thus reasonable to assume that the SGS scalar flux is proportional to this net scalar flux exchange. An alignment between J_i^{SGS} and $\Psi_{i\phi}^{SGS}$ can then be directly invoked as follows:

$$\begin{aligned} J_i^{SGS} &= D_\phi T_{SGS}\mathrm{P}_{i\phi} \\ &= -D_\phi T_{SGS}\left(J_j^{SGS}\frac{\partial \tilde{u}_i}{\partial x_j}+\tau_{ij}^{SGS}\frac{\partial \tilde{f}}{\partial x_j}\right), \end{aligned} \tag{4.40}$$

where D_ϕ is an adjustable parameter and T_{SGS} is an appropriate SGS time scale. This equation forms an implicit algebraic formulation for the SGS scalar flux vector, J_i^{SGS}. However, singularities can occur for certain types of behavior in the large-scale velocity and scalar gradient. Therefore, S.H. Peng et al. 2002 considered a simplified form of the equation by only taking the deviatoric part of SGS stress tensor, τ_{ij}^{SGS*}, and the large-scale scalar gradients. This renders

$$J_i^{SGS}=-D_\phi T_{SGS}\tau_{ij}^{SGS*}\frac{\partial \tilde{f}}{\partial x_j}, \tag{4.41}$$

where

$$\tau_{ij}^{SGS*}=\tau_{ij}^{SGS}-\frac{1}{3}\delta_{ij}\tau_{kk}^{SGS}=-2\nu_t\tilde{S}_{ij}. \tag{4.42}$$

Formulating the SGS time scale in terms of the filter size, and the SGS viscosity as $T_{SGS} \sim \Delta^2/\nu_t$, it becomes

$$J_i^{SGS} = D_{no}\Delta^2 \tilde{S}_{ij} \frac{\partial \tilde{f}}{\partial x_j}, \tag{4.43}$$

where D_{no} is the model coefficient that can be determined using a dynamic procedure.

Unlike the isotropic models, the proposed scalar model invokes a tensor diffusivity and takes into account the scalar gradients in all directions for each scalar flux component, The model is able to sustain the streamwise SGS scalar flux through a cross-stream large-scale scalar gradient in presence of SGS shear stresses, even when the scale gradient is vanished in the streamwise direction.

This model is a first step to use a tensor diffusivity in the literatures. It is to some extent similar to a scale similarity model subject to a Taylor expansion for the filtering operation. This model was examined in LES for a buoyant flow in an infinite vertical channel with two different headed side walls. It was shown that the proposed nonlinear model could reproduce reasonable results as compared with isotropic SGS diffusivity model and DNS data [86]. However, some important features related to simple configurations could not be well captures as demonstrated in M. Klein et al. 2004. To be more general, a new method is proposed in this work.

Anisotropy Model

In the models presented above, we noted some of the shortcomings in the prediction capacity when a scalar or isotropic eddy diffusivity hypothesis is used. The linearity also excludes any dependence on system rotation in the scalar flux relation. Furthermore, the assumption of alignment between the scalar flux vector and the mean filtered scalar gradient is often not well satisfied in real flows (see P.M. Wikstronem et al. 2000 and M. Klein et al. 2004). In contrast to S.H. Peng et al. who assumed, the alignment of scalar flux vector J_i^{SGS} and the production, the idea of constructing a more general valid expression for the scalar flux vector is here in a manner similar to that for explicit algebraic SGS stress tensor following the explicit algebraic Reynolds stress modeling (EARSM) or explicit algebraic scalar flux modeling (EASFM) in RANS (see B.E. Launder et al. 1975, C. Speziale 1991, A. Sadiki et al. 2003 and A. Yun 2005).

- The first step is here to consider a filtered transport equation for the scalar flux vector, equation (4.38).

- In contrast to S.H. Peng et al., here the weak equilibrium assumption is made and accounts for neglecting advection minus the SGS diffusion of the scalar flux vector in the transport equation. This is well satisfied for instance, for the case of homogeneous shear flow with an imposed mean scale gradient.
- The production vector term is explicit in the SGS stress tensor and scalar flux vector, but one needs to specify a model for the pressure-scalar gradient correlation and the destruction rate vector.

The model can be very complex. We rely to the experience in RANS (see A. Sadiki et al. 2003) and choose the expression in A. Yun 2005, rewritten for non-filtered quantities. One obtains then implicit expression for scalar flux vector. From this expression one can now derive the solution for the explicit J_i^{SGS} in terms of the original scalar flux vector in the form

$$J_i^{SGS} = D_{ij}^{an} \frac{\partial \tilde{f}}{\partial x_j}, \tag{4.44}$$

with

$$D_{ij}^{an} = D_\beta T_{SGS} \tau_{ij}^{SGS}, \tag{4.45}$$

as anisotropic diffusivity. D_β is an adjustable parameter and T_{SGS} is appropriate SGS time scale. It generalizes the model by S.H. Peng et al. 2002. Further consideration of the equation (4.45) consists in decomposing τ_{ij}^{SGS} (according to equation (4.17)) into a deviatoric part and an isotropic part. This results in the expression

$$J_i^{SGS} = D_\beta^1 \frac{\partial \tilde{f}}{\partial x_i} + D_\beta^2 T_{SGS} \tau_{ij}^{SGS*} \frac{\partial \tilde{f}}{\partial x_j}. \tag{4.46}$$

This general model consists obviously in two parts: linear part 1, which corresponds to the linear eddy diffusivity methods, and an anisotropic part 2, which includes the nonlinear, anisotropic contribution. When the SGS time scalar are formulated in terms of the filter size and the SGS viscosity following Smagorinsky, and the linear part is modeled according to equations (4.31) and (4.32), one obtains

$$J_i^{SGS} = \frac{C_{sm}}{S_{ct}} \Delta^2 \left|\tilde{S}\right| \frac{\partial \tilde{f}}{\partial x_i} + D_{an} \Delta^2 \tilde{S}_{ij} \frac{\partial \tilde{f}}{\partial x_j}, \tag{4.47}$$

where D_{an} is the anisotropic model coefficient.

A dynamic procedure is applied to calculate model coefficient D_{an}. It is accomplished by defining a

test filter (denoted by a caret), whose width $\hat{\Delta}$ is larger than the grid filter-width Δ. Dynamic adjustment of the model coefficients is based on the same theory as Germano proposed [67] and the major steps are presented as following.

According the model in equation (4.47), the SGS scalar flux on the test filter level is:

$$\mathrm{I} = \widehat{\widehat{u_i f}} - \hat{\tilde{u}}_i \hat{\tilde{f}} = \frac{C_{sm}}{S_{ct}} \hat{\Delta}^2 \left| \hat{\tilde{S}} \right| \frac{\partial \hat{\tilde{f}}}{\partial x_i} + D_{an} \hat{\Delta}^2 \hat{\tilde{S}}_{ij} \frac{\partial \hat{\tilde{f}}}{\partial x_j}. \tag{4.48}$$

The SGS scalar flux overlaps a test filter and results in

$$\Pi = \widehat{\widehat{u_i f}} - \widehat{\tilde{u}_i \tilde{f}} = \frac{C_{sm}}{S_{ct}} \widehat{\Delta^2 \left| \tilde{S} \right| \frac{\partial \tilde{f}}{\partial x_i}} + D_{an} \widehat{\Delta^2 \tilde{S}_{ij} \frac{\partial \tilde{f}}{\partial x_j}}. \tag{4.49}$$

To determine D_{an}, the error expression is adopted following Lilly [28] as:

$$\begin{aligned} e_i = {} & \widehat{\tilde{u}_i \tilde{f}} - \hat{\tilde{u}}_i \hat{\tilde{f}} \\ & - \left(\frac{C_{sm}}{S_{ct}} \widehat{\Delta^2 \left| \tilde{S} \right| \frac{\partial \tilde{f}}{\partial x_i}} + D_{an} \widehat{\Delta^2 \tilde{S}_{ij} \frac{\partial \tilde{f}}{\partial x_j}} - \frac{C_{sm}}{S_{ct}} \hat{\Delta}^2 \left| \hat{\tilde{S}} \right| \frac{\partial \hat{\tilde{f}}}{\partial x_i} + D_{an} \hat{\Delta}^2 \hat{\tilde{S}}_{ij} \frac{\partial \hat{\tilde{f}}}{\partial x_j} \right). \end{aligned} \tag{4.50}$$

To simplify the expression, define H_1, H_2 and F_i (equation (4.34)) for each direction component as:

$$H_{1i} = \widehat{\Delta^2 \left| \tilde{S} \right| \frac{\partial \tilde{f}}{\partial x_i}} - \hat{\Delta}^2 \left| \hat{\tilde{S}} \right| \frac{\partial \hat{\tilde{f}}}{\partial x_i} \quad \text{and} \quad H_{2i} = \widehat{\Delta^2 \tilde{S}_{ij} \frac{\partial \tilde{f}}{\partial x_j}} - \hat{\Delta}^2 \hat{\tilde{S}}_{ij} \frac{\partial \hat{\tilde{f}}}{\partial x_j}. \tag{4.51}$$

So equation (4.50) can be written as:

$$e_i = F_i - \frac{C_{sm}}{Sc_t} H_{1i} + D_{an} H_{2i}. \tag{4.51}$$

Following Lilly [28] who proposed that the error incurred when a single coefficient is used be minimized in a least-squares sense, we obtain

$$\frac{\partial \langle e_i e_i \rangle}{\partial D_{an}} = 2 \left\langle e_i \frac{\partial e_i}{\partial D_{an}} \right\rangle = 0. \tag{4.52}$$

Finally, the model coefficient can be calculated by

$$D_{an} = \frac{\left(F_i - \frac{C_{sm}}{S_{ct}} H_{1i} \right) H_{2i}}{H_{2i} H_{2i}}. \tag{4.53}$$

These SGS models have been implemented in the code FASTEST-3D and tested in several configurations. The results of the new anisotropy model compared with isotropic models will be presented in Charter 6 and 7. Even though the complexity becomes aware by the formulation

procedure, an overall improvement with the anisotropy model is encouraging for the further research work in this direction.

Chapter 5
Numerical Methodology

The conservation equations are more complex than they appear. They are non-linear, coupled, and difficult to solve. Experience shows that Navier –Stokes equations describe the flow of a Newtonian fluid accurately. In most cases, even the simplified equations cannot be solved analytically, one has to use numerical methods. The starting point of any numerical method is the mathematical model. The sets of equations used for flow predication were presented in Chapter. 2. After selecting the mathematical model, one has to consider a suitable discretization method, i.e. a method of approximating the differential equations by a system of algebraic equations for the variables at some sets of discrete locations in space and time. Among different discretization methods, Finite Difference (FD), Finite Volume (FV) and Finite Element (FE) share the credits. For a recent overview of these methods, one can refer to [71]. Each type of method yields the same solution if the grid is very fine. However, some methods are more suitable to some classes' problems than others. The preference is often determined by the attitude of developers.

The discrete locations at which the variables are to be calculated are defined by the numerical grid which is essentially a discrete representation of the geometric domain on which the problem is to be solved. It divides the solution domain into a finite number of sub-domains (elements, control volume, etc.). Following the choice of the grid type, one has to select the approximation to be used in the discretization process. In the finite volume method adopted in this work, one has to select the methods of approximating surface and volume integrals.

Discretization yields a large system of non-linear algebraic equations, and the choice of solver depends on the grid types and the number of nodes involved in each algebraic equation.

Finally one needs to set the convergence criteria for the iterative method. There are two levels of iterations: inner iteration within which the linear equations are solved and the outer iteration, that deals with the non-linear equations and coupling equations. Deciding when to stop the iterative

process on each level is important, from both accuracy and efficiency view.

The procedure described above is the numerical issues needs to be considered in every CFD computational code. The numerical code used in this work is known as FASTEST-3D (see [2] and [36]). It is a code for block-structured grid and based on the finite volume method. The program is well optimized for efficient parallel and vector computations. Some achievements of the code can be found in [2] and [98]. The sections in this chapter provide general numerical procedures and discuss the primary numerical methods used in the code. The numerical error evaluation can refer to the book of M. Peric & J.H. Ferziger 1996. Some special issues such as pressure correlation, TVD (total variation diminishing) scheme etc have been studied extensively in [14], which will not be repeated here. If one wants to end up with a unique solution to these differential equations, suitable boundary conditions have to be formulated. This will be outlined in Section 5.4.

5.1 Finite Volume Method

The finite volume method is a method for representing and evaluating partial differential equations as algebraic equations. To use the finite volume methods, the solution domain is subdivided into a finite number of small control volumes (CV) by grids, in contrast to the finite difference (FV) method, that defines the control volume boundaries, not the computational nodes.

In the Figure 5.1, a typical 3D Cartesian (the coordinates in a three dimensional system are of the form (*x, y, z*)) control volumes are shown with the notation to be used. The CV surface can be subdivided into six plane surfaces, denoted by lower case letters corresponding to their directions (e, w, n, s, t, and b) with respect to the central note (P).

Taking into account the non-orthogonal of the grid used, it is plausible to use in each CV and on each CV face a local coordinate system and then to transform the operators (derivatives) from local into the global (Cartesian) coordinate system. In FASTEST-3D a hexahedron control volume is used. The derivative of field variable Φ with respect to Cartesian coordinates can be expressed in terms of the local coordinates with a transformation matrix (the transformation method can refer to [5]). Every hexahedral control volume contains grid points and a central point, representing the mean over the full control volume (Mid-point rule). The standard Cartesian coordinates are used below for denotation.

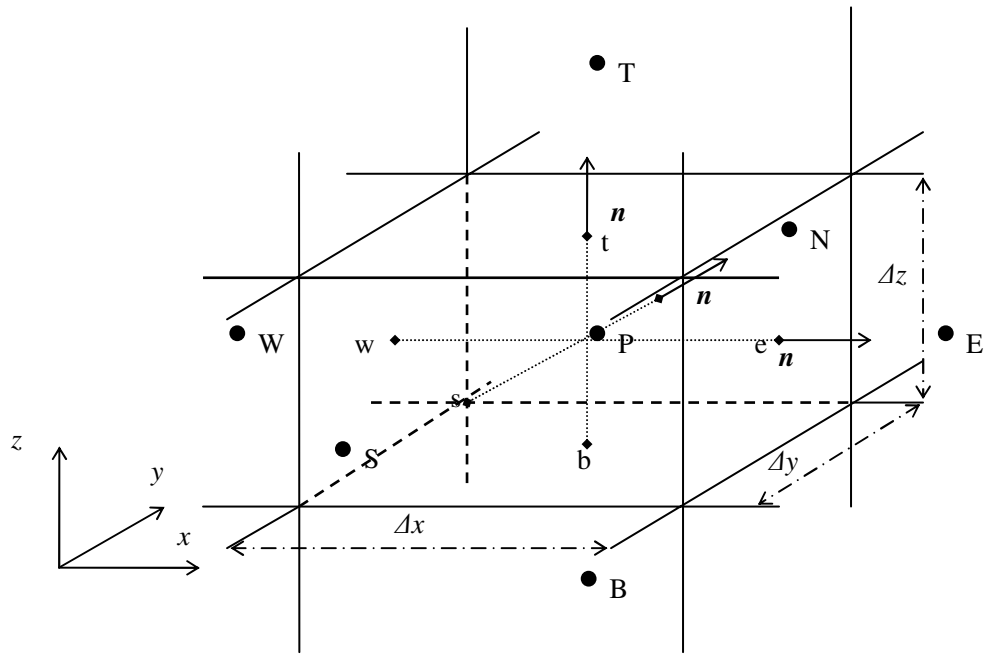

Figure 5.1: A typical CV and the notation used for a Cartesian 3D grid

All the governing equations can be expressed in a general transport equation for Φ ($\Phi = 1, u_i, f$ respectively) and integrated in a control volume, *V*:

$$\underbrace{\int_V \frac{\partial}{\partial t}(\rho\Phi)\,dV}_{\text{unsteady term}} + \underbrace{\int_V \frac{\partial}{\partial x_i}(\rho u_i \Phi)\,dV}_{\text{convective term}} - \underbrace{\int_V \frac{\partial}{\partial x_i}\left(\Gamma_\Phi \frac{\partial \Phi}{\partial x_i}\right)dV}_{\text{diffusive term}} = \underbrace{\int_V Q_\Phi dV}_{\text{source term}} . \tag{5.1}$$

The equation can be divided into an unsteady, convective, diffusive and source term. The convective and diffusive term can be transformed, by means of Gauss divergence theorem, into flux over the surface *S*, so that equation (5.1) becomes

$$\int_V \frac{\partial}{\partial t}(\rho\Phi)\,dV + \int_S \rho u_i \Phi n_i dS - \int_S \Gamma_\Phi \frac{\partial \Phi}{\partial x_i} n_i dS = \int_V Q_\Phi dV , \tag{5.2}$$

where *S* is the surface enclosing the volume *V* and n_i (*i=1,2,3*) represents the components of the unit vector $\vec{n}$ normal to the surface *S* and directed outwards the surface (see Figure 5.1).

5.2 Discretization in Space

The differential equation (5.2) should be converted into algebraic form for each control volume (known as discretization procedure) and then solved it. The sections below will introduce the spatial

discretization procedure for each term of the general transport equation (5.2). The temporal discretization will be introduced in Chapter. 6 along with its application in the mixing layer configuration.

5.2.1 Unsteady Term Discretization

In this work, the volume integral is approximated by the value in the central of the cell (denote by P) cumulated over the volume. The unsteady term is approximated as:

$$\int_V \frac{\partial \rho\Phi}{\partial t} dV \approx \left(\frac{\partial}{\partial t} \rho\Phi\Delta V \right)_P , \tag{5.3}$$

where ΔV is the volume of the CV. To approximate the term in the right hand side, one can use first order scheme

$$\left(\frac{\partial \rho\Phi}{\partial t} \Delta V \right)_P^{n+1} \approx \frac{(\rho\Phi)_P^{n+1} - (\rho\Phi)_P^n}{\Delta t} \Delta V , \tag{5.4}$$

or second order scheme

$$\left(\frac{\partial \rho\Phi}{\partial t} \Delta V \right)_P^{n+1} \approx \frac{3(\rho\Phi)_P^{n+1} - 4(\rho\Phi)_P^n - (\rho\Phi)_P^{n-1}}{2\Delta t} \Delta V_p . \tag{5.5}$$

Here, Δt denotes a time interval and the superscripts and $n, n-1$ and $n+1$ are related to the actual, previous and following time steps. The method to evaluate the dependent values (e.g. Φ and Γ_Φ) on which time step can be categorized as explicit scheme

$$\left(\frac{\partial}{\partial t} \rho\Phi\Delta V \right)_P^{n+1} = f^n(\Phi, \Gamma_\Phi, \cdots) , \tag{5.6}$$

or implicit scheme

$$\left(\frac{\partial}{\partial t} \rho\Phi\Delta V \right)_P^{n+1} = f^{n+1}(\Phi, \Gamma_\Phi, \cdots) . \tag{5.7}$$

Explicit schemes are characterized by calculating values of the dependent variables at one time level entirely in terms of values calculated previously, making them relatively easy to implement. However, they tend to require restrictions on the interval of the time step to avoid numerical instability, and this can be expensive in terms of computation time.

Implicit schemes are characterized by calculating values of the dependent variables simultaneously

so that a system of equations must be solved at each time level. This leads to complicated code and can also be computationally expensive. However, implicit schemes tend to have much better stability properties than their explicit counterparts and so have been preferred for many commercial applications.

In FASTEST-3D, a hybrid scheme (Crank-Nicholson Scheme) is implemented for solving both the accuracy and the stability problem as:

$$\left(\frac{\partial}{\partial t}\rho\Phi\Delta V\right)_P^{n+1} = \frac{f^{n+1}(\Phi,\Gamma_\Phi,\cdots)+f^{n}(\Phi,\Gamma_\Phi,\cdots)}{2}. \tag{5.8}$$

5.2.2 Convective Term Discretization

The integral of the convection term over the surfaces around the control volume can be written as the sum of the six around surfaces

$$\int_S \rho u_i \Phi n_i dS = \sum_d \int_{S_d} \rho u_i \Phi n_i dS_{i,d}\ . \tag{5.9}$$

Here *d* points to the six surfaces around a control volume (e, w, n, s, t, and b). Then a 3D problem (volume) becomes a 2D problem (surface) as represented in Figure 5.2. In a surface, the surface central point represents the mean over the surface (Mid-point rule).

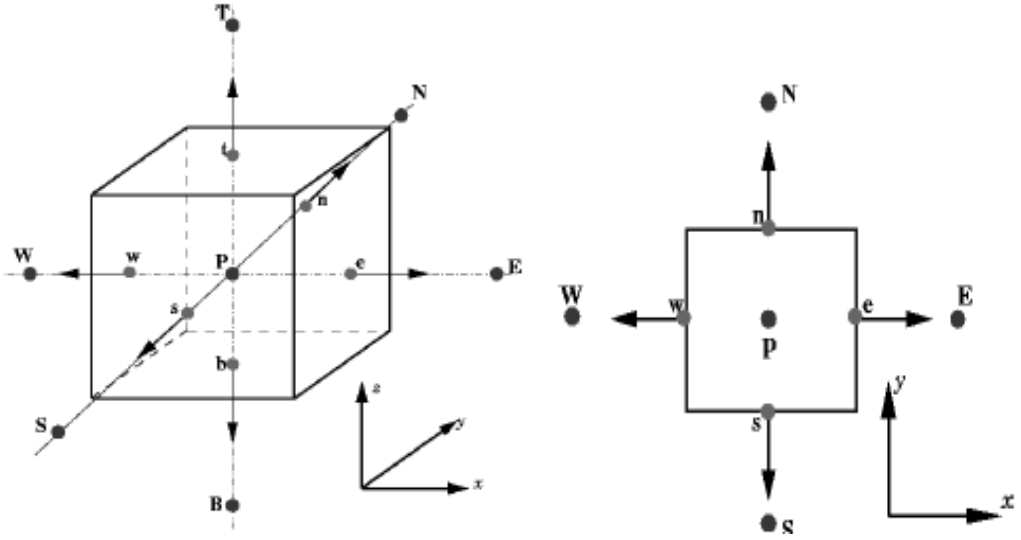

Figure 5.2: A typical CV and notations used for a Cartesian surface

For the face “East” (“e”), the following representation is therefore used as:

$$\int_{S_e} \rho u_i \Phi n_i dS_{i,e} = \left(\rho u_i \Phi n_i \Delta S_i\right)_e = \left(\rho u_x \Phi\right)_e \cdot \left(\Delta S_x\right)_e + \left(\rho u_y \Phi\right)_e = \underbrace{\left(\rho u_x\right)_e}_{\mathbb{F}_e^c} \Phi_e \Delta y \,. \qquad (5.10)$$

The next step should be interpolation of variable Φ_e because the quantity on the cell faces may not be given in the collocated grid. For the convective flux two interpolation practices of different order of accuracy are introduced here.

Approximates the Φ_e by its value at the node upstream of "e" is equivalent to using backward or forward difference approximation for the first derivative (depending on the flow direction, see Figure 5.3), hence the named upwind difference scheme (UDS) for this approximation is defined by

$$\Phi_e^{UDS} = \max(\mathbb{F}_e^c, 0)\Phi_P + \max(-\mathbb{F}_e^c, 0)\Phi_E \,. \qquad (5.11)$$

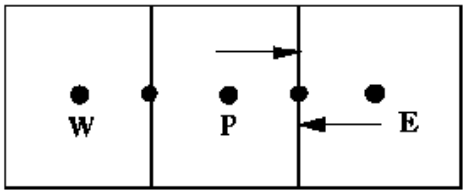

Figure 5.3: Upwind Difference Scheme

Even though it never yields oscillatory solutions, this scheme produces numerical diffusion because it is only a first order scheme. Thus very fine grids are required to obtain accurate solutions. An improvement can be achieved by a second order accuracy. For that purpose a central difference scheme (CDS) is introduced as:

$$\Phi_e^{CDS} = \Phi_E \lambda_e + \Phi_P (1 - \lambda_e), \quad \lambda_e = \frac{x_e - x_P}{x_E - x_P} \,. \qquad (5.12)$$

The central value is interpolated between the two nearest nodes (*P* and *E*) as in Figure 5.4.

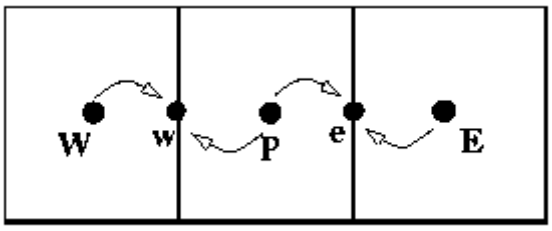

Figure 5.4: Central Difference Scheme

This is the simplest second order scheme and the most widely used. While with all approximations of order higher than one, this scheme may produce oscillatory solutions. The use of higher order interpolation leads to large computational molecules. Therefore, the deferred correlation approach is introduced. One can use a flux blending factor o to blend the lower order scheme and higher order scheme, e.g. $\Phi_e^h = \Phi_e^{UDS} + o(\Phi_e^{CDS} - \Phi_e^{UDS})$. The o can be adjusted between zero, which is same as UDS, to one, which is same as CDS. This is a hybrid method. Other schemes (e.g. QUICK, Power Law Scheme [71]) will not be explained here.

5.2.3 Diffusive Term Discretization

Similar to convective term, the diffusive part over the "East" ("e") face can exemplarily be discretized as:

$$\int_S \left(\Gamma_\Phi n_i \frac{\partial \Phi}{\partial x_i} \right) dS = \int_{S_i} \left(\Gamma_\Phi n_i \frac{\partial \Phi}{\partial x_i} \right) dS_{i,e} \approx \Gamma_\Phi \frac{\partial \Phi}{\partial x_i} \Delta S_{i,e} \,. \tag{5.13}$$

In the frame of CDS method, the diffusive flux is implemented as (see Figure 5.2):

$$\left(\Gamma_\Phi \frac{\partial \Phi}{\partial x_1} \right)_e dS_{x,e} = \underbrace{\left(\frac{\Gamma_\Phi}{\Delta x} \right)_e}_{\mathbb{F}_e^d} (\delta \Phi)_e \Delta y = \frac{\Gamma_\Phi}{x_E - x_P} (\Phi_E - \Phi_P) \Delta y \,. \tag{5.14}$$

In the general transport equation, the convective and diffusive term on the east surface can be summarized as:

$$\begin{aligned}
\left(\int_S \rho u_i \Phi n_i dS - \int_S \Gamma_\Phi \frac{\partial \Phi}{\partial x_i} n_i dS \right)_e &= \mathbb{F}_e^c \Phi_e^{UDS} \Delta y + \underbrace{o \mathbb{F}_e^c (\Phi_e^{CDS} - \Phi_e^{UDS}) \Delta y}_{Q_e^{DF}} + \mathbb{F}_e^d (\Phi_P - \Phi_E) \Delta y \\
&= \mathbb{F}_e^c \Delta y \max\left(\mathbb{F}_e^c, 0 \right) \Phi_P + \mathbb{F}_e^c \Delta y \max\left(-\mathbb{F}_e^c, 0 \right) \Phi_E + \mathbb{F}_e^d \Delta y \Phi_P - \mathbb{F}_e^d \Delta y \Phi_E + Q_e^{DF} \\
&= \underbrace{\left(\mathbb{F}_e^c \Delta y \max\left(\mathbb{F}_e^c, 0 \right) + \mathbb{F}_e^d \Delta y \right)}_{A_P^e} \Phi_P + \underbrace{\left(\mathbb{F}_e^c \Delta y \max\left(-\mathbb{F}_e^c, 0 \right) - \mathbb{F}_e^d \Delta y \right)}_{A_E} \Phi_E + Q_e^{DF} \\
&= A_P^e \Phi_P + A_E \Phi_E + Q_e^{DF} \quad .
\end{aligned} \tag{5.15}$$

And for all surfaces, this yields

$$\sum_d \left(\int_S \rho u_i \Phi \cdot n dS - \int_S \Gamma_\Phi \frac{\partial \Phi}{\partial x_i} \cdot n dS \right) = \underbrace{\left(A_P^e + A_P^w + A_P^n + A_P^s + A_P^t + A_P^b \right)}_{A_P} \Phi_P +$$
$$A_E \Phi_E + A_W \Phi_W + A_N \Phi_N + A_S \Phi_S + A_T \Phi_T + A_B \Phi_B +$$
$$\underbrace{Q_e^{DF} + Q_w^{DF} + Q_n^{DF} + Q_s^{DF} + Q_t^{DF} + Q_b^{DF}}_{Q_P^{DF}}$$
$$= A_P \Phi_P + \sum_{Nb} A_{Nb} \Phi_{Nb} + Q_P^{DF} \quad , \tag{5.16}$$

where *Nb* points to the neighbor notes of a CV.

5.2.4 Source Term Discretization

According to the Mid-point rule, the source term can be simply written as:

$$\int_V Q_\Phi dV == \left(Q_\Phi \Delta V \right)_P = Q_\Phi . \tag{5.17}$$

To sum all the discretization procedure mentioned above, in the frame of implicit formulation, the general transport equation can be formulated as:

$$\left(\int_V \frac{\partial}{\partial t} \left(\rho \Phi \right) dV + \int_S \rho u_i \Phi \cdot n dS - \int_S \Gamma_\Phi \frac{\partial \Phi}{\partial x_i} \cdot n dS - \int_V S_\Phi dV \right)^{n+1} =$$
$$\underbrace{\frac{\Delta V}{\Delta t}}_{A_P^{time}} \Phi_P^{n+1} - \underbrace{\frac{\Delta V}{\Delta t} \Phi_P^n}_{Q_P^{time}} + A_P \Phi_P^{n+1} + \sum_{Nb} A_{Nb} \Phi_{Nb}^{n+1} + \left(Q_P^{DF} \right)^{n+1} - Q_P^{n+1} \Delta V_p \quad , \tag{5.18}$$

and

$$\underbrace{\left(A_P^{time} + A_P \right)}_{A_P} \Phi_P^{n+1} + \sum_{Nb} A_{Nb} \Phi_{Nb}^{n+1} = \underbrace{Q_P^{time} - \left(Q_P^{DE} \right)^{n+1} + Q_P^{n+1}}_{Q_P} \quad . \tag{5.19}$$

The final discretized equation for a CV center in the computational domain becomes

$$A_{\mathrm{P}} \Phi_{\mathrm{P}} + \sum_{\mathrm{Nb}} A_{Nb} \Phi_{\mathrm{Nb}} = Q_P \quad . \tag{5.20}$$

Each node results into above kind of an algebraic equation and can be formulated into a matrix form as:

$$\underbrace{\begin{bmatrix} & A_E & A_N & A_T \\ \ddots & \ddots & \ddots & \ddots \\ \ddots & A_P & \ddots & \\ \ddots & \ddots & \ddots & \\ & A_W & A_S & A_B \end{bmatrix}}_{A} \begin{bmatrix} \\ \\ \Phi \\ \\ \\ \end{bmatrix} = \begin{bmatrix} \\ \\ Q \\ \\ \\ \end{bmatrix}. \tag{5.21}$$

The coefficient matrix A should be diagonally dominant. How to solve the system will be addressed in the section below.

5.3 Solution Method

Discretization yields a large system of algebraic equations. The matrix version of the complete system is given in section 5.2, which is repeated here

$$A\Phi = Q, \tag{5.22}$$

where A is coefficient matrix built from the coefficients for each CV. To solve the system, a solution method needs to be considered. Because the direct solver (Gauss elimination or LU decomposition) cost very high (the triangular factors of sparse matrices are not sparse), indirect solver (iterative method) can be used. With this method, some initial solutions is guessed and then systematically improved.

Supposing after n iterations we have an approximated solution Φ^n which doesn't satisfy these equations exactly. Instead, there is a non-zero residual $\imath^n$:

$$A\Phi^n = Q - \imath^n. \tag{5.23}$$

The convergence error may be defined as:

$$e^n = \Phi - \Phi^n, \tag{5.24}$$

where Φ is the converged solution and thus,

$$Ae^n = \imath^n. \tag{5.25}$$

The purpose of the iteration procedure is to drive the residual to zero and in the process e also becomes zero. To see how this can be done, consider an iterative scheme for a linear system, such a scheme can be written as:

$$M\Phi^{n+1} = N\Phi^n + B. \tag{5.26}$$

Obvious, the iterative method must converge to equation (5.22), by definition, at convergence, we

must have

$$A = M - N \text{ and } B = Q . \tag{5.27}$$

The structures of M and N matrices depend on the type of solver. Different solvers are available namely: Gauss-Siedel, SIP (or incomplete LU decomposition). Details of the solvers can refer to [71] and [44]. M should be a dominant matrix to achieve faster convergence. Usually, one has to define convergence criteria. Once the magnitude of the error vector is less than the defined convergence criteria, iterations are stopped. Usually, for convergence, error is brought down to at least to four orders of magnitude.

5.4 Treatment of Boundary Conditions

For solving the governing equations and having a completely determined problem, additional information are necessary on all boundary points. Usually, there are two kinds of boundary conditions. When the quantity value is directly specified on the boundary, it is classed into Dirichlet boundary condition (e.g. inlet, wall) and treated as:

$$A_P\Phi_{\mathrm{P}} + A_E\Phi_{\mathrm{E}} + A_W\Phi_{\mathrm{W}} + A_N\Phi_{\mathrm{P}} + A_B\Phi_{\mathrm{B}} = Q_P , \tag{5.28}$$

and

$$A_P\Phi_{\mathrm{P}} + A_E\Phi_{\mathrm{E}} + A_W\Phi_{\mathrm{W}} + A_N\Phi_{\mathrm{P}} = \underbrace{Q_P - A_B\Phi_{\mathrm{B}}}_{Q_P} . \tag{5.29}$$

When the boundary values are presented as gradient forms, they are Neumann boundary conditions (e.g. symmetry or flux boundary) and treated as:

$$\frac{\partial\Phi}{\partial y} = 0, \rightarrow \frac{\Phi_P - \Phi_B}{y_P - y_B} = 0, \rightarrow \Phi_P = \Phi_B , \tag{5.30}$$

and

$$\underbrace{(A_P + A_B)}_{A_P}\Phi_{\mathrm{P}} + A_E\Phi_{\mathrm{E}} + A_W\Phi_{\mathrm{W}} + A_N\Phi_{\mathrm{P}} = Q_P . \tag{5.31}$$

In the present computations, the fluid velocity and mixture fraction are specified at the inlet based on the two kinds of boundary conditions. At the solid surfaces, no-slip boundary condition for the velocity is set. A flux conserving zero gradient boundary condition is applied at the outlet. Additionally, initial conditions must be specified at the beginning of the computations according to specific configuration conditions.

Chapter 6
Applications

In this Chapter, some applications of the derived LES code to the simulation of mixing processes are presented and discussed. Distinct aspects concerning modeling, simulation and validation have been investigated, first separately simple systems and thereafter collectively increasing the complicity of the investigated systems.

The systematical model assessment should actually include the computation and comparison of the numerical results to experimental data in configurations of various complexities. For these reasons, the configurations chosen for the model assessment are presented and discussed in the following order:

- A spatially developing turbulent mixing layer is considered first as starting point for model assessment. Study on sensitivity of LES is carried out to evaluate the "error factors" in the reference simulation.
- Mixing processes in jet in cross flow will be considered for its practical importance in gas turbine, fuel injection applications, V/STOL aircraft chemical units, etc. and its complexities due to the strong unsteady interaction of jet flow and cross flow. This represents gas mixing systems characterized by a small Schmidt number.
- The next configuration consists of mixing process in a jet in channel flow. This system is confined and water stream is considered introducing high Schmidt number effects, which represents a challenging issue for mixing models.

6.1 LES of a Spatially Developing Turbulent Mixing Layer

In this section a three-dimensional mixing layer in a confined flow is simulated with LES. It is of great importance to first have a detailed understanding of the determinant factors that accomplish a LES when developing the methodology to describe the turbulent mixing phenomena. This configuration is computationally affordable on the current computers. It therefore allows a thorough investigation of the sensitivity of the LES regarding resolution, time-averaging method and variations in the inflow conditions. Subsequently, the different SGS scalar flux modeling approaches are considered and the corresponding results are compared to each other and to experimental data.

6.1.1 Configuration Description

Numerical simulation follows the experimental setup from L.K. Hjertager et al. 2002, see Figure 6.1. The measurements were performed in a mixing channel with a cross section of $60*60\ mm^2$. The first part of the channel is divided into two smaller feed channels with a cross section of $20*60\ mm^2$ by an obstruction of size $20*60*330\ mm^3$. This is done to allow mixing of two streams in the main channel. The fluid in the channel is water at room temperature. The channel has a total length of *970 mm*, and the length available for mixing is *640 mm*.

The combined Particle Image Velocimetry (PIV) and Planar Laser Induced Fluorescense (PLIF) techniques were used for the measurements. PIV was used to measure the instantaneous velocity field and PLIF was used to measure the instantaneous concentrations. In Figure 6.2, the basic geometric parameters and flow conditions are presented.

There are three investigation positions located at the initial mixing zone (Position 1 & Position2) and in the area at the end of the channel (Position 3). The experimental data are available in the x-z-planes, yielding the U and W velocity components in x and z direction, respectively. The bulk velocities in the feed channels were *0.17 m/s*, which correspond to a Reynolds number based on the feed channel hydraulic diameter of *5100*. The bulk velocity in the main channel was *0.11 m/s*, which gave a Reynolds number based on main channel hydraulic diameter of *6600*. The bulk

concentration in feed channel A, is normalized to one and the bulk concentration in feed channel B, to zero.

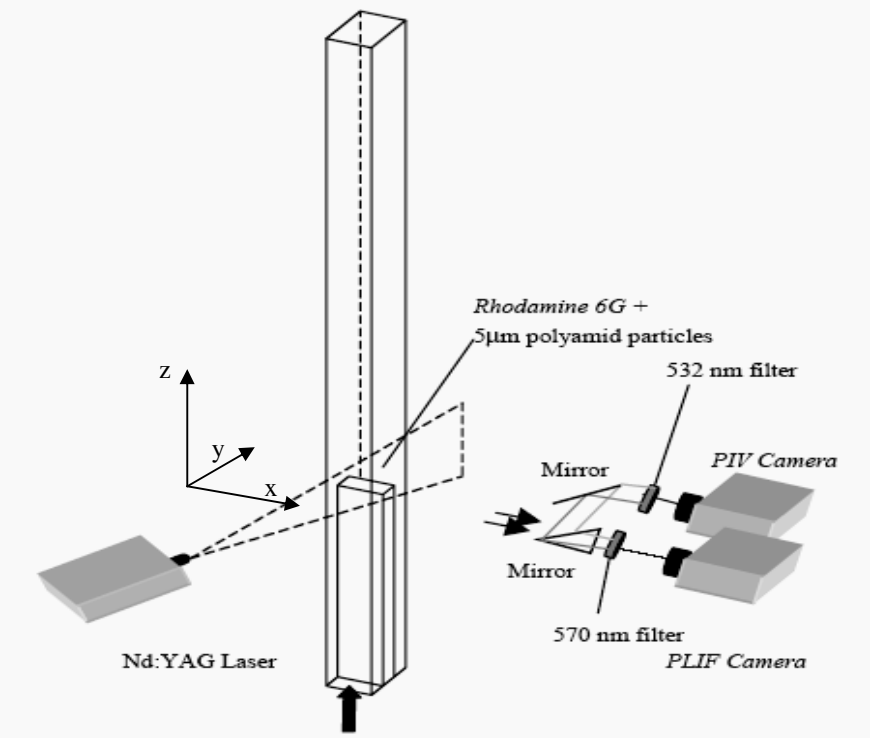

Figure 6.1: Schematic drawing of the experimental setup and the PIV/PLIF system of the mixing layer configuration

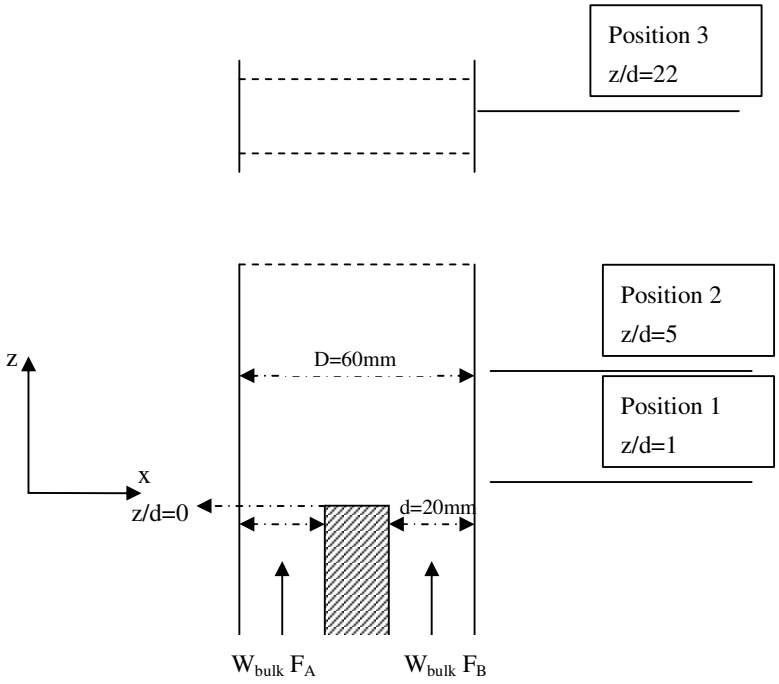

Figure 6.2: Geometric conditions and investigated positions

6.1.2 Sensitivity of Reference LES

Although LES is computationally much less expensive than DNS and provides more information of the turbulence flow properties than RANS simulation, it has the disadvantage to leave open the possibility of significant errors resulting from the choice of filter (grid resolution), approximation of boundary conditions and the time-averaging process. Moreover, the unknown SGS term needs to be assessed in detail in order to manage well the possible contamination from the numerics.

To infer the sensitivity of the reference LES, the section therefore discuses LES of mixing layer in which relevant "error factors" are systematically analyzed.

6.1.2.1 Grid Resolutions

The numerical geometry resembles with experiments, while the total length of the channel is shorter than the one in the experiments for saving computational time. The error brings by this curtailment can be overcome by an accurate implementation of inflow and outflow boundary conditions. The geometry date and grid resolutions are summarized as in Table 6.1. Both a coarser (N1) and a finer resolution grid (N2) are computed to point out the influence of grid resolution.

Direction	Length	Coarse grid (N1)	Fine grid (N2)
Wall normal	x/D, y/D= -0.5,0.5	41	55
Streamwise	Z/D= -1.5, 8	180	230
		CV : 302580	CV : 605000

Table 6.1: Geometry data and grid resolutions of the mixing layer configuration

D is the hydraulic diameter of the mixing chamber. The numerical grid is block-structured grids generated by the software-ICEMCFD.

There have two opinions to evaluate the grid resolution of LES. One states that a LES resolution

should be situated in the inertial sub-range of turbulent kinetic energy spectrum. The measure of scales in inertial sub-range may be the Taylor microscale L_T. The number of grid points related to the characteristic length scale *Lc* should be around (as pointed out in Chapter. 3)

$$N1^1_{LES\_L_c} \sim \frac{L_c}{L_T} \sim \mathrm{Re}_t^{1/2}. \tag{6.1}$$

Another opinion is that the grid resolution should be around 5-10 time of DNS resolution, which means the smallest resolved scales should be *5-10* time Kolmogorov scale. In this case, the number of grid points related to the characteristic length scale *Lc* should be around

$$N1^2_{LES\_L_c} \sim \frac{1}{(5\sim 10)}\frac{L_c}{L_K} \sim \frac{1}{(5\sim 10)}\mathrm{Re}_t^{3/4}. \tag{6.2}$$

These two opinions originate from the same theory and approximate to the same level of grid resolutions (N1 in the reference case). In this case, we assume that L_K is approximately equal to the Batchelor length scale $L_{\phi B}$. This is rather valid only for molecular Schmidt number equal to one.

When the molecular Schmidt number is larger than one, the smallest scale for the mixing, the Batchelor scale $L_{\phi B}$, is smaller than the Kolmogorov scale: $L_{\phi B} \sim Sc^{-1/2} L_K$. Because the working fluid is water (for room temperature water, the molecular Schmidt number is around *10*) in this setup, this relation implies that the Batchelor scale approximates to *1/3* of the Kolmogorov scale. Then computational requirement on the grid resolution is correspondingly increased. Following the theory based on the velocity field requirement (LES resolution should be around *5-10* time smallest scales), *5-10* times Batchelor scale required to be resolved in the scalar field and thus a finer gird (N2 in the reference case) is needed.

Comparing instantaneous solutions is the most severe test when the sensitivity is considered. The instantaneous streamwise velocity (*w*) and mixture fraction (*f*) are compared for different resolutions at the monitoring point A, see Figure 6.3 (*T0* is the time step when the flow become fully turbulent.). The coordinates of the monitoring point are given in the table 6.2. This point is located in the recirculation area and middle of mixing layer.

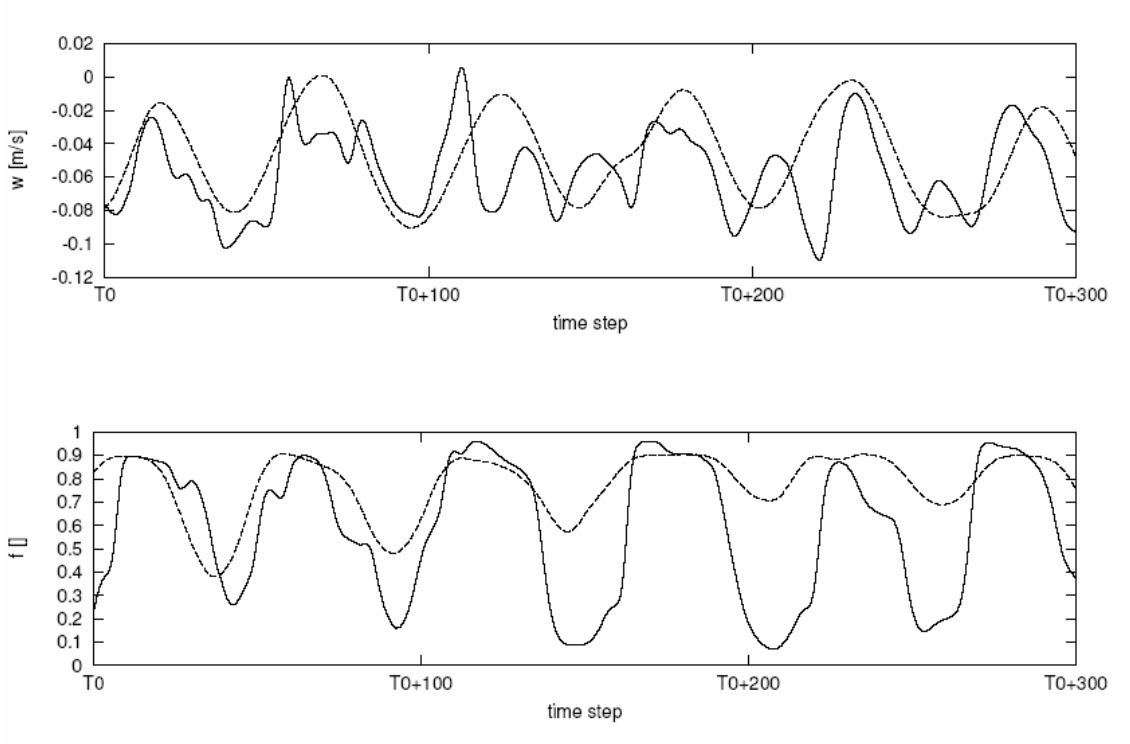

Figure 6.3: Instantaneous streamwise velocity and mixture fraction with different grid resolutions

(—fine grid --- coarse grid)

Monitoring Points	x (m)	y (m)	z (m)
	0	0	0.005

Table 6.2: Coordinates of the monitoring point

It is clear from Figure 6.3 that the velocity solutions arising at the two resolutions coincide in the same fluctuation magnitude. It means they have approximately resolved the same level of the turbulent kinematics energy. However the results of mixture fraction lose the consistency. The fluctuations of fine grid have much larger magnitude than the coarse ones, which means that the coarse grid cannot resolve enough the “scalar energy”. The reason may be ambilateral. One may be due to too coarse grid so that the resolution requirement is not fulfilled in scalar field. Another reason may be due to the low level SGS scalar model (the computation used the eddy diffusivity model) that can not capture enough SGS behavior. This fact certainly influences the statistical results. For these reasons, we decide to use fine grid for further study.

6.1.2.2 Boundary Conditions

Since boundary conditions have important impact on the large scales of flow structures, LES is very sensitive to the boundary conditions. As introduced in the first chapter, the boundary treatment can be classed into two main methods. The simpler one just uses the laminar inflow conditions and leaves the flow freely develop to fully turbulence. A laminar inflow condition is based on the bulk velocity and can be improved to fit into reference inlet configuration. Another method introduces inflow perturbations, with which the flow already becomes turbulent from the inlet. There are many works that deal with the turbulent inflow conditions. The advantages and limitations of different inflow conditions can be referred to the thesis of E. Bohr 2005. Figure 6.4 presents a schematic picture of the laminar and turbulent inflow condition for a channel.

In this work, to emphasize the importance of boundary conditions, there was an adjustment of the boundary conditions in advance. The first try was used the constant boundary conditions which use the bulk velocity for all positions on the boundary. We found the flow was too steady comparing with experimental data (the scope of fluctuation was too small). The second way was to use turbulent inflow generator, [68]. Because the first experimental measured profile is far from inflow boundary, it was difficult to accurate prescribe fluctuations at the inflow which are needed for the turbulent inflow generator. The third strategy was to use a polynomial fit following C. Mengler 2001, hereby a polynomial function to describe the wall effect and the turbulent mean velocity profile on the inflow was defined, in a way to achieve a good agreement with the experimental measures at the position 1.

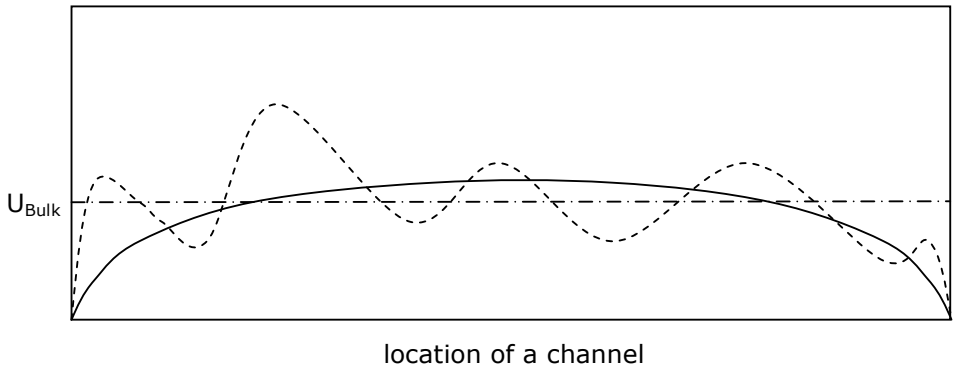

Figure 6.4: Schematic picture of laminar and turbulent inflow conditions for a channel
(— laminar condition --- turbulent inflow condition)

6.1.2.3 Time-Averaging Processes

LES produces a database, in which every data is an instantaneous value at a position (*x, y, z*). To get the statistic results, a time-averaging process and a measure for monitoring convergence of the time-average are needed. Supposing averaging has been performed from time t_0 to time t_1, this time-averaging process depends on both the total sampling time interval and the spatial coordinates:

$$\langle \Phi(x, y, z) \rangle = \frac{1}{(t_1 - t_0)} \int_{t_0}^{t_1} \Phi(x, y, z, t) dt \tag{6.3}$$

To reach an accurate statistical result, there are two problems must take into consideration:

Time Step Width: Like the discretization in space, the discretization in time affects accuracy. Normally, reduced time interval allows for an accurate solution, like the smaller cells resulting in improved precision. With explicit methods a limited time step width is thus a precondition to obtain a stable scheme. A so called Courant, Friedrich and Levy criteria "CFL-condition" is in general used to evaluate the time interval as:

$$CFL = \frac{\Delta t |U|}{\Delta x} \leq 1 \rightarrow \quad \Delta t \leq \frac{\Delta x}{\Delta t}. \tag{6.4}$$

Simply speaking, this criterion requires that, within one time step, information may only travel to the neighboring cell but no further. In this work *CFL=1* is chosen for define the time step width.

Time Independent Sampling: Once simulation starts, we need to decide how often a sampling data has to be read out. The aim is to ensure sampling data to be statistically time independent. This may be clarified by the autocorrelation function. At one special position, the time autocorrelation function $R_A^T(t)$ of a continuous real function $\Phi(t)$ is defined by

$$R_A^T(t) = \lim_{\Delta t \to \infty} \frac{1}{2\Delta t} \int_{-\Delta t}^{\Delta t} \Phi(\tau) \Phi(t + \tau) d\tau, \tag{6.5}$$

where Δt is the time interval. The correlation between two events separated in time diminishes as the interval increases. Figure 6.5 represents the autocorrelation function against time steps for streamwise direction velocity component and mixture fraction. The coordinates of the monitoring point are listed in table 6.2.

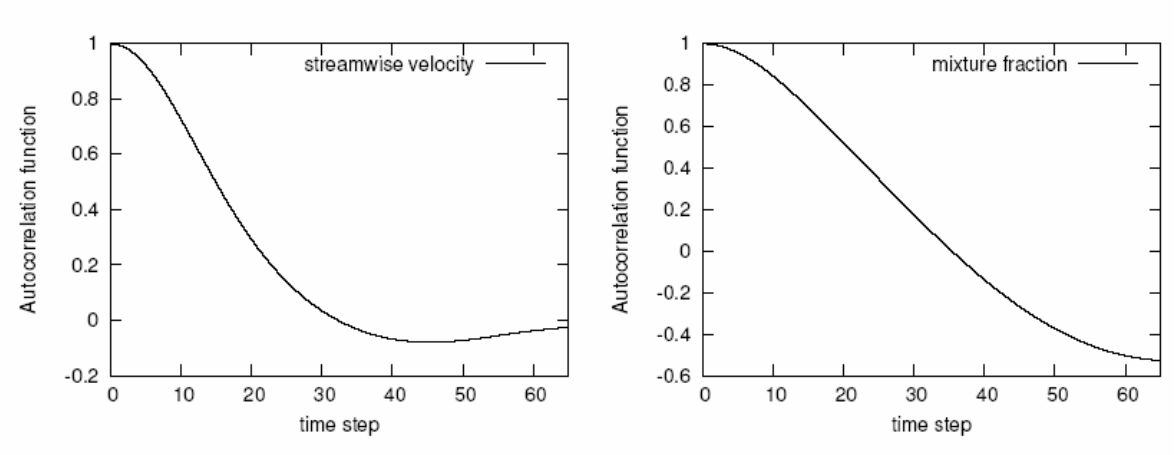

Figure 6.5: Autocorrelation function results of streamwise velocity and mixture fraction

Usually, when the autocorrelation reduces to *0.2-0.3* (integral time scales), the number of time step can be used as the interval to guarantee the time independent samplings. Therefore, from the results presented in Figure 6.5, every *20* time steps a sampling data is read out to perform further statistical calculations.

In analyzing statistical results of a spatially developing flow we should average long enough in time to guarantee a proper estimate of the average solution and its physical properties. It is hard to quantify the criteria. Throughout the simulations in the thesis, the averaging process has always started at time when the flow becomes fully turbulent, and ends at the time when the results presented do not change significantly when the averaging is ended at a later moment in time.

6.1.3 LES Results and Discussion

In the frame of academic applications, the validation of LES can be validated by the means of data from DNS. With DNS database, a priori test can be used to validate the SGS quantities or SGS models directly. However, for most of real turbulent flows with high Reynolds number, DNS data aren't available. The LES validation exercise therefore turns to use experimental data. However, there are three main disadvantages when the LES results are validated against experimental data. First of all, the experimental errors are hard to be noticed by numerical

workers. Secondly, the measured data are usually not enough to validate the numerical data throughout space and time. The third limitation is that, with experimental data, a priori test is almost impossible to perform; instead, a posteriori validation can be accomplished.

Because simulations in this thesis are carried out for complex configurations with high Reynolds number, the DNS data are not available. Therefore, all the validations are achieved by the comparison with experimental data.

6.1.3.1 Velocity Field

Figure 6.6 shows the normalized streamwise velocity (w) and wall-normal velocity (u) at different axial positions compared against experimental data. From the results of the mean velocity, first of all, the good agreement on the first position proves that the polynomial fit can achieve satisfying results in this kind of "young" turbulent flow. From the position 1 to position 3, where the mean velocity is almost a flat profile, an overall agreement can be achieved by LES with Dynamic Smagorinsky SGS stress model. The velocity fluctuations are highest in the shear layers were the mean velocity gradients are largest. The velocity fluctuations also coincide well with the measurements while it has to be noticed that the results of w components is not symmetric (physically it is a symmetric flow in the streamwise direction). The error may due to the numerical scheme. Besides the numerical code, this agreement validates the LES predicting ability with regard to velocity field.

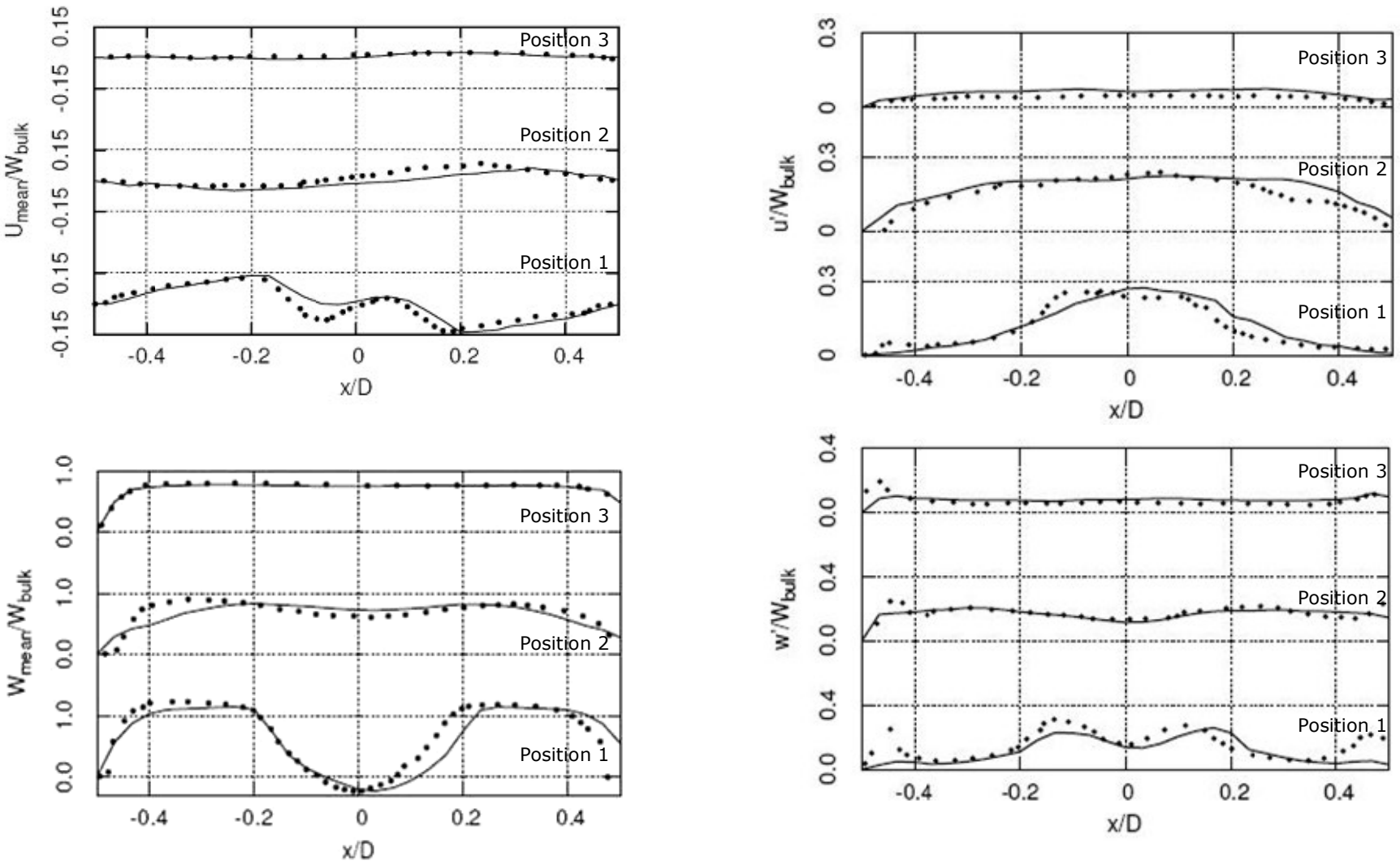

Figure 6.6: Normalized streamwise velocity (mean *W* and fluctuation *w'*) and wall-normal velocity (mean *U* and fluctuation *u'*) at different positions versus experimental data

(−LES ⋯ EXP)

6.1.3.2 Scalar Field

Once the flow field is good reproduced, the LES ability to capture the scalar field behavior can be solely investigated. To have a clear idea of the SGS scalar flux model influence, different SGS scalar flux models are evaluated in coupling to the same SGS stress model in the velocity field, see Table 6.3. The result in Figure 6.6 presents the mean mixture fraction (*F*) and its fluctuation (*f'*) at three positions along the streamwise direction.

SGS model	Case 1	Case 2	Case 3	Case 4
SGS stress	Dynamic	Dynamic	Dynamic	Dynamic
SGS scalar flux	No model	Eddy Diffusivity	Dynamic	Anisotropy

Table 6.3: Different SGS scalar flux models coupling with dynamic SGS stress model implemented in the mixing layer configuration

The calculated mean mixture fraction result includes a computation without any SGS scalar flux model to point out SGS influence in scalar field (case 1). The original eddy diffusivity model is implemented with a constant turbulent Schmidt number ($Sc_t = 1$) (case 2), and then modified it by dynamic procedure (case 3). Because these two models are based on the same assumption, they come to almost same results for the mean quantity in this configuration. Thus only dynamic model result is presented. The new anisotropy model is implemented with dynamic procedure to compute the model coefficient (case 4). From the comparison results, at position 3, there is no big difference between models because at this position the mixture is going uniform and thus the mixing action becomes weak (scalar variances become smaller). At the positions 1 and 2, the difference is sensible because of the important contribution of SGS when the mixing process just starts. At all the positions, the anisotropy model achieves an overall improvement. This model results catch the experimental data in very good detail while this achievement is appended by more computational cost. The computational time used for the new model is around *1.8* times of eddy diffusivity model. Table 6.4 presents the computational cost needed for different SGS scalar flux models. A high computational resource is therefore always required, when higher level model has to be considered.

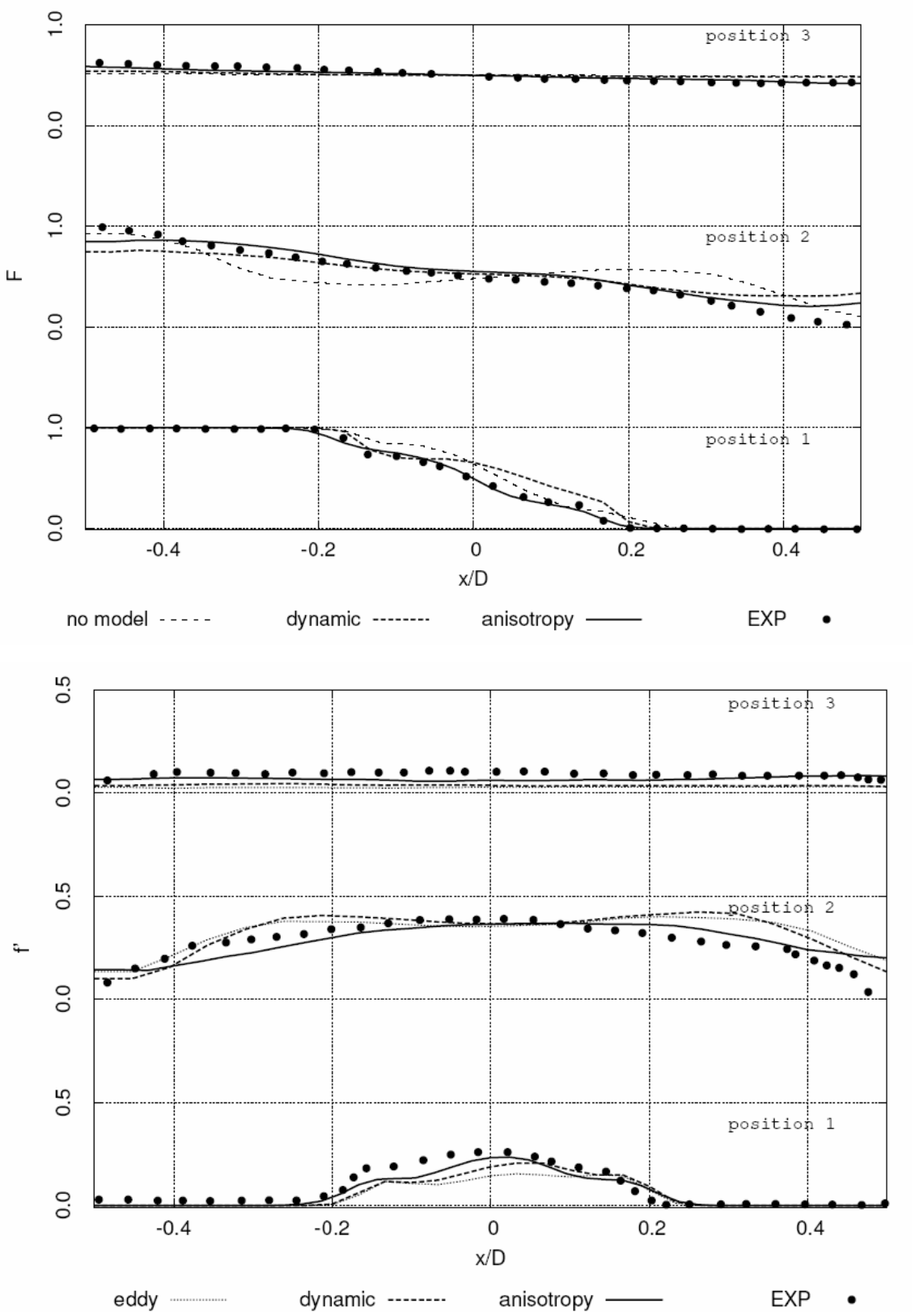

Figure 6.7: Mean mixture fraction (F) and fluctuation (f') with different SGS scalar flux models versus experimental data

The predicting abilities of eddy diffusivity model with and without dynamic procedure are different in the fluctuation results. The difference is stemmed from various turbulent Schmidt numbers applied. The result in Figure 6.8 displays the time averaged turbulent Schmidt number calculated by the dynamic procedure at the position 2. It varies between *0* and *1.7*, and the highest values appear at the mixing "surface" (shear layer) and not at the centerline. From the results obtained, a variable values from the dynamic procedure achieves better predictions than an empirical constant value. This conclusion already applied to the velocity field where the dynamic Smagorinsky model becomes more popular. The main disadvantage of dynamic SGS models is that a dynamic procedure needs artificial restriction for stability purposes, such as cut-off of the model coefficient if negative averaging in a homogenous direction.

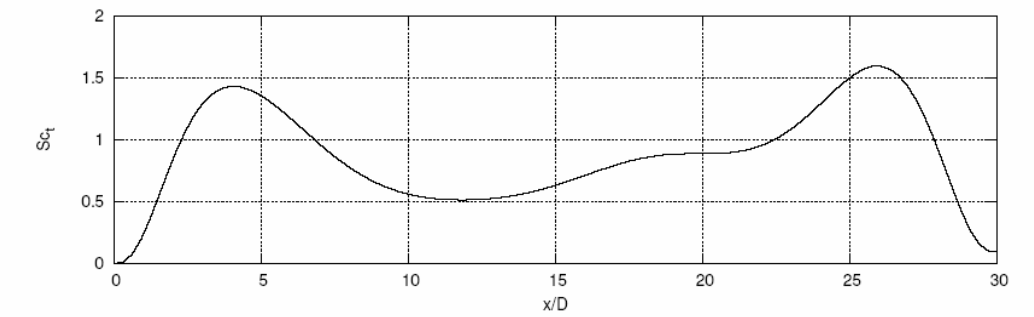

Figure 6.8: Turbulent Schmidt number calculated by the dynamic procedure

Model	Time
No SGS scalar flux model	1
Eddy Diffusivity	1.02
Eddy Diffusivity with dynamical procedure	1.2
Anisotropy model	1.9

Table 6.4: Computational cost of different SGS scalar flux models

6.2 Jet in Cross Flow – Open Configuration with Air

Jet in cross flow is an important flow configuration encountered in gas turbines, fuel injection, V/STOL aircraft, in chemical unit operations and boilers, and waste disposal into water bodies or the atmosphere. Thereby, three dimensional and unsteady vortical structures [104] provide a

rather efficient mechanism for the mixing process. The experiments by T.F. Fric & A. Roshko 1994 and R. Kelso et al. 1996 show that there exists a complex vortical flow structure in the near field of jet in cross flow. In addition to the horse-shoe vortex, ring-like vortices (jet shear–layer vortices) and counter rotating bound vortex pair, Fric and Roshko observed up-right wake vortices which extend vertically from the wall to the jet as Figure 6.9 shows:

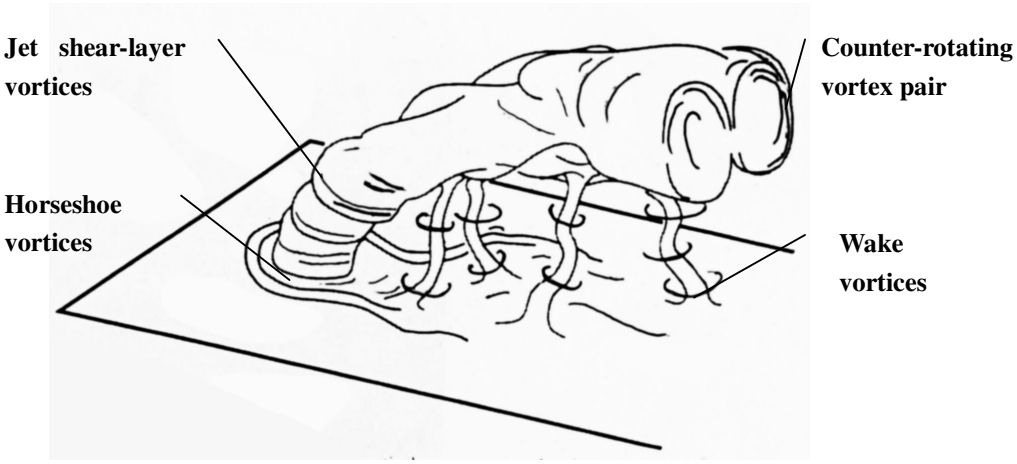

Figure 6.9: Flow structures of the jet in cross flow configuration [97]

This flow complexity is stemmed from the strong interaction of the jet flow and the cross flow which exists in near wall region. Thus, the near wall effect brings challenges to both grid resolution and modeling in particular in the frame of LES. There has been over fifty years' numerical research dealing with this configuration (see [8], [51], [66] and [83]). Many reports are focused on RANS calculations. LES based investigations (e.g. [22], [55]) concentrated mainly on classical turbulent flows. Detailed numerical studies of scalar field and mixing analysis have been first provided by [19], [23], [41] and [105]. However, with regard to optimization issues, it is advisable to well find out the influence of the mixing modeling on the prediction of the scalar field, when credible statement have to be made in complex configurations. For such engineering process, systematic analyses are not yet available. Therefore, in this study, in addition to acquiring detailed and accurate velocity and scalar data by LES, it is the objective to gain further insight into the topology of such mixing processes and relevant factors which may influence them.

Focusing on the mixing processes, the influence of the SGS scalar flux models on the prediction

of the mixing is examined throughout this section. This will allow selecting the SGS scale flux model that is capable of providing reliable results for further investigations in Chapter 7 focusing on mixing analysis, enhancement and optimization.

6.2.1 Configuration and Numerical Setup

The numerical setup of jet in cross flow, as depicted in Figure 6.10, was chosen to resemble the experiments of J. Andreopoulos & W. Rodi 1984 with a jet inflow velocity V_{jet}=*6.95m/s* and a cross stream approaching along a flat plate with a velocity U_{cf}=*13.9m/s*. The velocity ratio is *0.5*. The corresponding Reynolds number based on the jet velocity and pipe diameter (*D=50mm*) is *20500*. The basic geometrical parameters and boundary conditions are presented in Figure 6.10. The experiments of J. Andreopoulos & W. Rodi provide detailed hot wire measurements of the mean velocity components, the turbulent kinetic energy, the Reynolds stresses and measurements on the turbulent kinetic energy budget. Furthermore they made measurements on a slightly heated jet to obtain statements on the mixing behavior by measuring the temperature field.

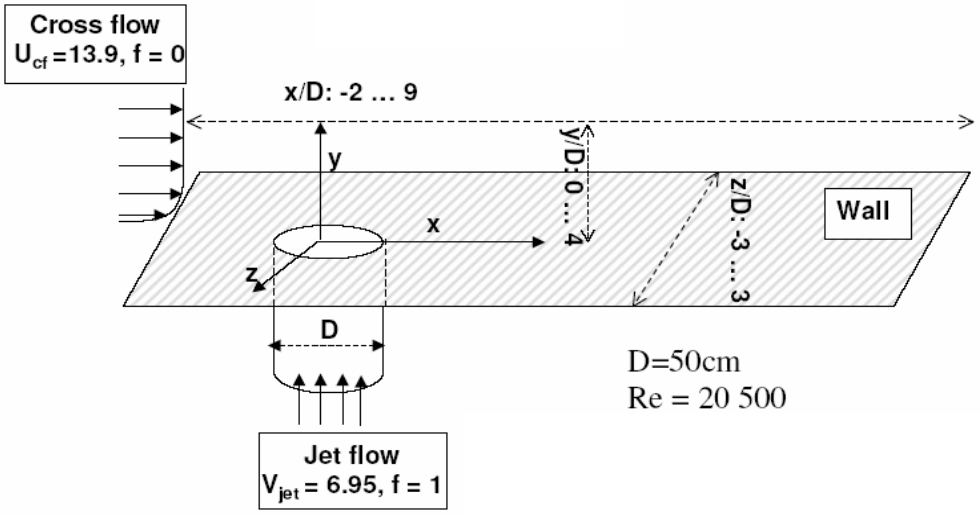

Figure 6.10: Numerical setup of the jet in cross flow configuration

Grids were generated with ICEMCFD and O-grid is used to model the pipe. The total control volume is *430000* cells. The inflow velocity of the jet is described by Inflow-Generator [68] using the DNS-Data from a developed pipe flow (AGARD-PCH00 [65]). The inflow generator based on the idea of creating spatially and temporally correlated signals prescribes one-point

statistics (mean values and Reynolds stresses) and time/length scale at inlet. For the cross flow, after comparing different inflow conditions, the laminar inflow condition with a polynomial function [22]

$$\frac{\langle u \rangle}{U_{cf}} = 1 - \left(\frac{y}{H} - 1 \right)^{60}, \tag{6.6}$$

where H is the height of cross flow, to describe the mean velocity profile at the inlet have been proved to reach plausible result. In order to find out the different predicting ability of SGS scalar flux models, different models combinations have been applied. They are summarized in Tabled 6.5.

SGS model	Case 1	Case 2	Case 3	Case 4
SGS stress	Dynamic	Dynamic	Dynamic	Dynamic
SGS Scalar Flux	Eddy Diffusivity	Dynamic	Scale Similarity	Anisotropy

Table 6.5 Different SGS scalar flux models coupling with dynamic SGS stress model implemented in the jet in cross flow configuration

As mentioned above, the near wall effect plays an important role in the strong interaction of the jet flow and the cross flow. In the modeling, no special wall treatment is used. Instead, we resolve the boundary layer and rely on the ability of the dynamic procedure to capture the correct asymptotic behavior of velocity profile when approaching the wall.

6.2.2 LES Results and Discussion

As first simulation results, the U and V components of the mean velocity as well as the shear stress component ($u'v'$) are compared in the Figure 6.11 with the experimental data at different positions downstream for the symmetric plane ($z/D=0$). The computed mean streamwise and transverse velocities show a very good overall agreement with the experimental data. The existing deviations can be explained by the fact that the hot wire anemometry employed by Andreopolis and Rodi is not able to determine the direction of the flow. The argument has

already been put forward by [55]. In contrast to the measurements, the LES shows a negative axial velocity at $x/D = 1.0$ which is linked to the well-known existence of a recirculation region. Since the magnitude matches well and the positions before and after are in good agreement with the experimental data it must be assumed that a recirculation exists here. The overall agreements establish LES as an alternate method for predicting velocity fields applying the Smagorinsky SGS model using the dynamic procedure.

Dealing now with the scalar field concerning different SGS scalar flux models, the result presented in Figure 6.12 for the mean mixture fraction shows that all the models can achieve an acceptable agreement, where the anisotropy model (case 4) accomplishes an overall palpable improvement especially on the wake of the flow where the flow reaches to fully mixed. But in some area, such as the position of jet brim, the deviation is certainly related to the so-called “near nozzle effect” which still is a point of issue in LES. The use of more realistic boundary conditions in addition to more resolution may yield improvement in the prediction of this region. The results presented with the eddy-diffusivity model (case 1), a dynamic procedure for calculating the model coefficient (case 2) and scalar similarity model (case 3) do not show a significant difference in predicting the mean mixture fraction, as they inherently suffer from the isotropic turbulent viscosity based assumption.

By extending the comparison to fluctuation of mixture fraction, the result in Figure 6.13 shows that the eddy-diffusivity model with dynamic procedure reproduces the observations better than the traditional eddy diffusivity model. The difference between scale similarity model and dynamic procedure results is not significant. Nevertheless, during calculations the dynamic procedure produced some unbounded values, which could contribute to numerical instability. This could be avoided by using an artificial cut-off procedure, while the scale similarity model appears more numerically stable and easier to implement. In the literature, it is known for the flow field that the scale similarity model has to be considered with Smagorinsky model in a mixed mode to yield a stable implementation. In the scalar field, the instability cased by the scale similarity model does not appear in this simulation. With enough computational resources in hand, the anisotropy model is more recommendable. In the Figure 6.13, this anisotropy model shows a better predicting ability, while all other three models underpredict the fluctuation of mixture fraction. Especially, the anisotropy model can accurately grasp the maximum values of

the fluctuation, which are essential quantities for quantifying the mixing degree.

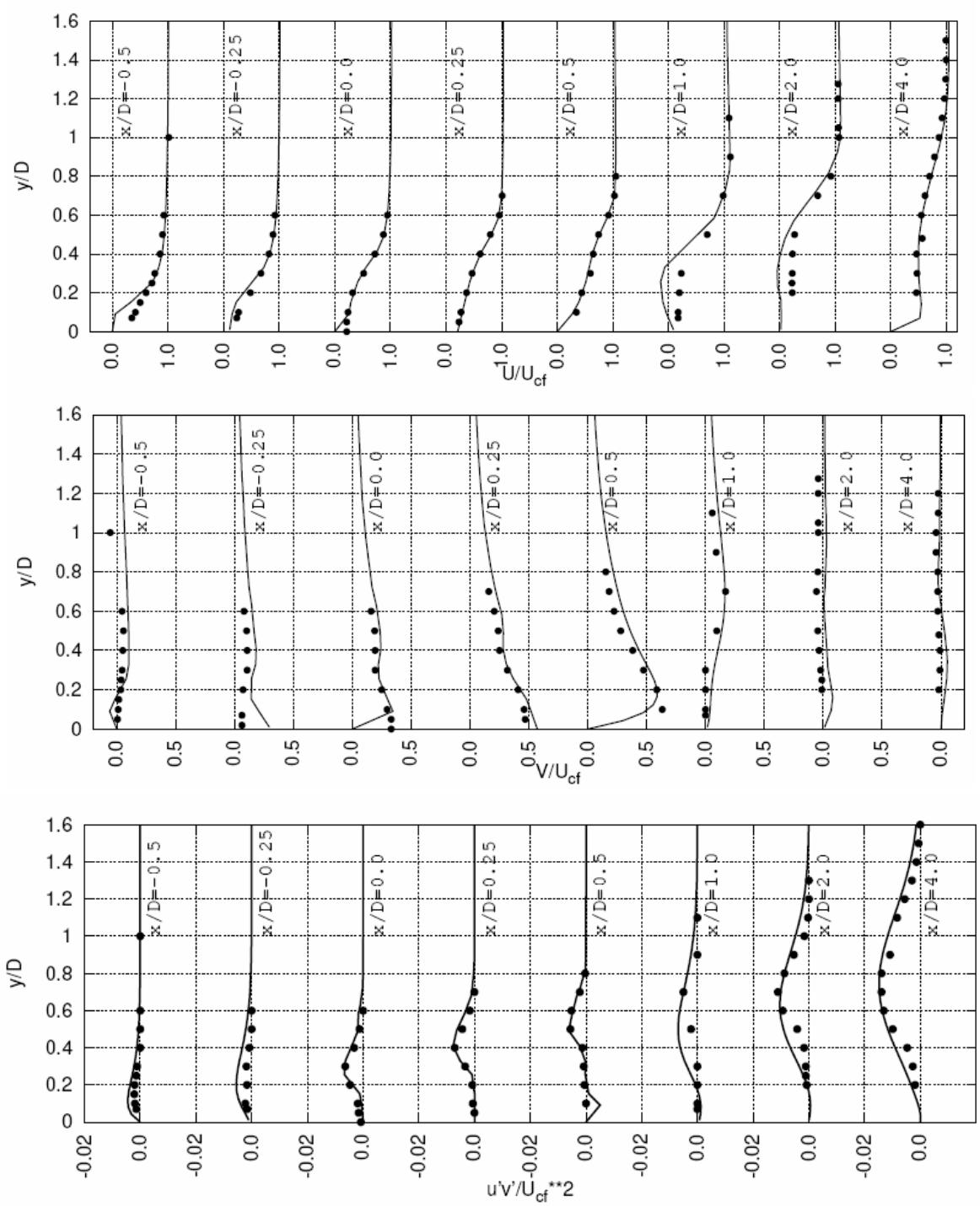

Figure 6.11: Comparison of normalized velocity quantities with experimental data

Mean streamwise velocity (U); Mean wall-normal velocity (V); Shear stress ($u'v'$)

(—LES ··· EXP)

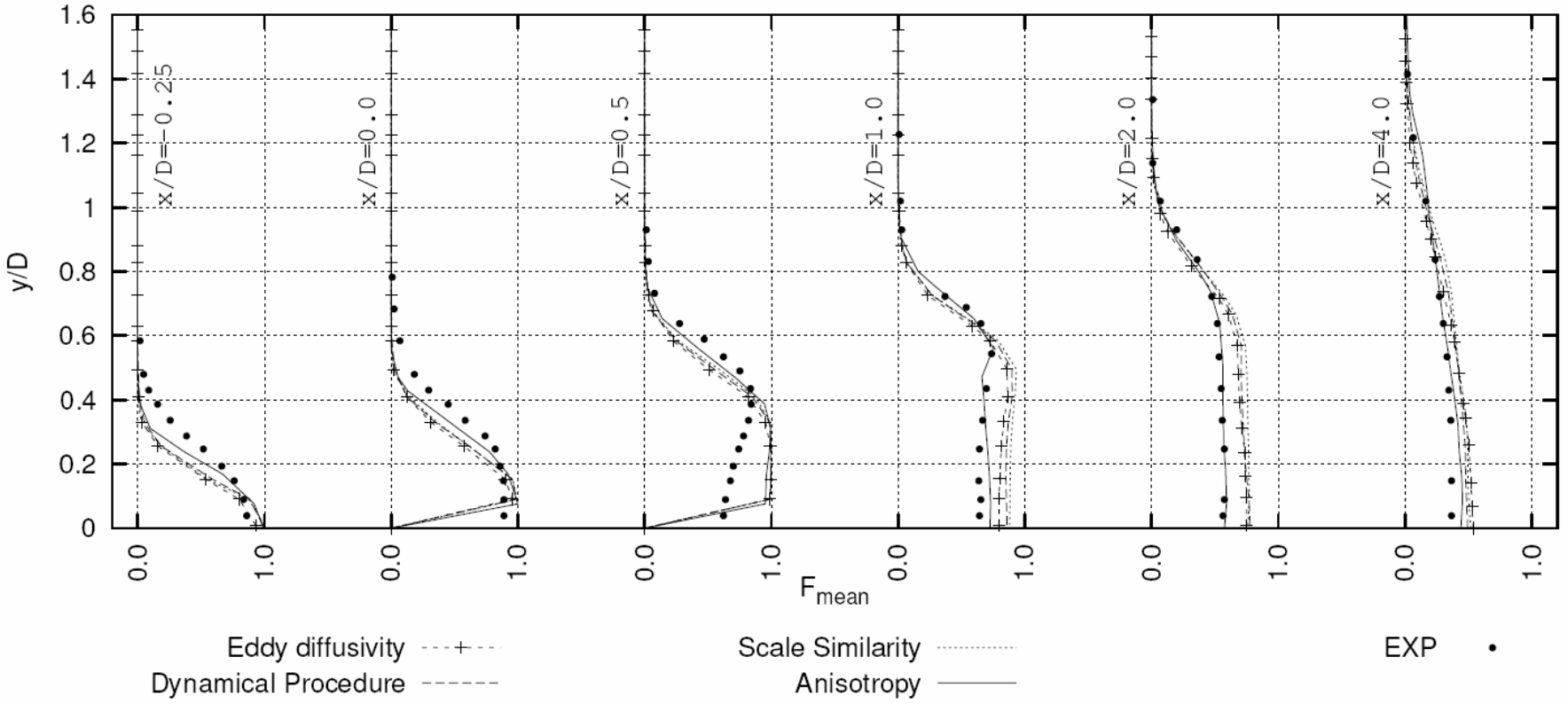

Figure 6.12: Mean mixture fraction with different SGS scalar flux models versus experimental data

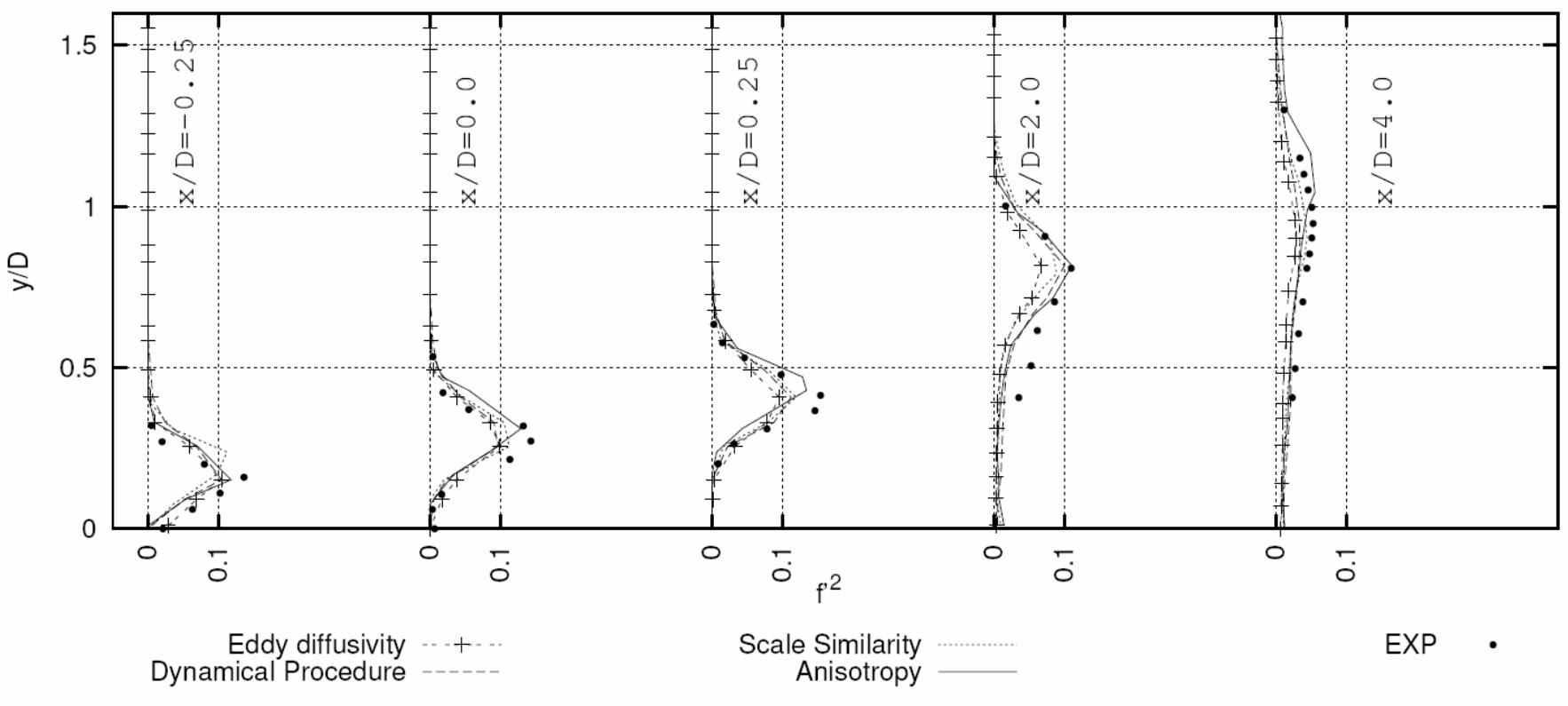

Figure 6.13: Fluctuation of mixture fraction with different SGS scalar flux models versus experimental data

6.3 Jet in Channel Flow – Confined Configuration with Water

There are two common ways to involve a cross flow, one choice was the jet flow injected into an open area and cross fluid flows with a free path (Section 6.2). Another way is to choose the cross flow confined by four sides walls (channel) which means the mixing happens in a closed area (Section 6.3). To cover all the mixing scaling phenomena which can differ through the molecular Schmidt number *Sc*, water flows ($Sc > 1$) are used as working fluids besides air streams ($Sc \leq 1$) employed in Section 6.2.

6.3.1 Configuration and Numerical Setup

The numerical setup was chosen to resemble the experiments of K.E. Meyer et al. 2001. In their experiments, simultaneous measurements of velocities and concentration with Planar Laser Induced Fluorescense (PLIF) combined with Particle Image Velocimetry (PIV) are compared to similar measurements with pointwise Laser Induced Fluorescense (LIF) made with a slightly modified standard Laser Doppler Anemometer (LDA).

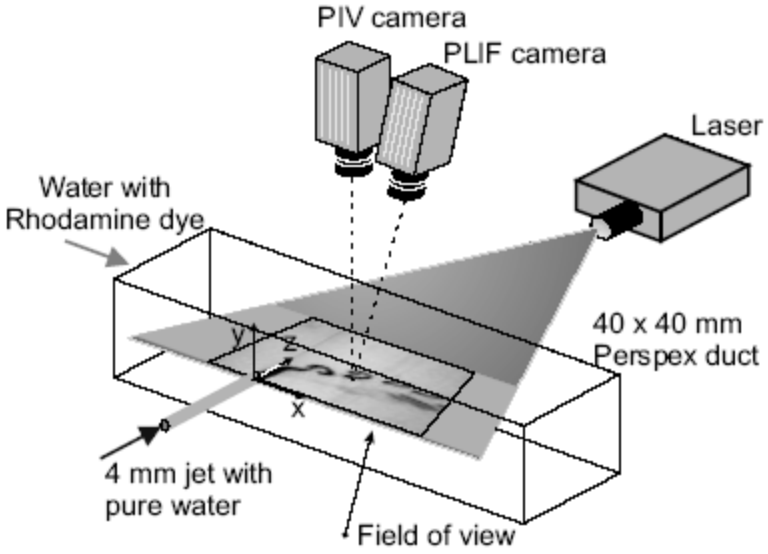

Figure 6.14: Schematic drawing of flow and measurement system setup

The reference geometry consists of a straight duct with a square cross section of *40*40 mm*. The jet, emerging from the mid-point of one side wall and perpendicular to this wall, is created from a pipe with an inner diameter of *D=4* mm and a length of *30 D*. Both channel and jet consists of clean water. The water temperature is *26°C*. The Reynolds number *Re = 33750* base on hydraulic diameter and bulk mean velocity U_{cf} of the duct flow. The basic flow conditions are listed in Table.6.5. The coordinate system is centered at the jet axis at the entrance to the duct, *x* being in the direction of duct flow and *z* in the direction of the jet axis as depicted in Figure 6.14. Experimental data are available in the x-z plane centered in the duct, yielding the *U* and *W* components of velocity in *x* and *z*, respectively.

Velocity Ratio	Channel		Jet	
3.3	U_{cf}=0.75 m/s	Re_{cf}=33750	U_{jet}=2.5 m/s	Re_{jet}=11250

Table 6.5: Flow conditions of the jet in channel flow configuration

Numerical grids were generated with ICEMCFD and the cells are uniformly distributed in all directions whereas in the close wall and near pipe area the finer grids are performed. The specification of grids can be seen in Table 6.6 and Figure 6.15. The total control volumes are *415788*. This may be considered as compromise between the real CV requirement following the equation (6.2) and the available computational capacity.

Direction	Length	Grid points
Streamwise	x/D = -5 … 10	105
Transverse	w/D = -5 … 5	53
Wall-normal	Y/D = -5 … 5	70
Jet	Z/D = -5 …0	50

Table 6.6: Geometry parameters and grid resolution of the jet in channel flow configuration

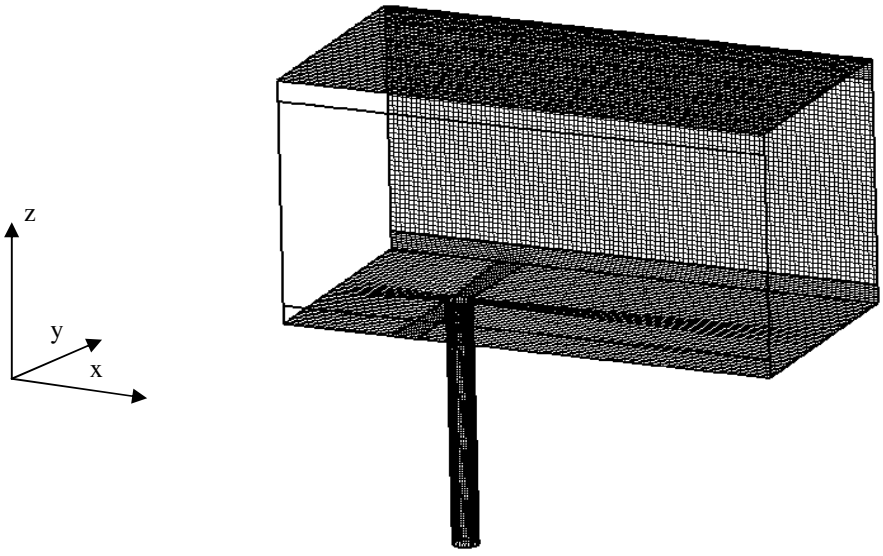

Figure 6.15 Gird resolution of the jet in channel flow configuration

The inflow velocity of the jet is simply a constant bulk velocity because the narrow diameter of jet makes the turbulent inflow condition difficult to implement. To overcome the shortage of laminar inflow, relative long jet geometry should be simulated so that the jet flow can self develop into turbulence before injecting into the channel. The inflow condition of the channel flow uses a polynomial fit method to describe the shape of the inlet velocity profile. A fourth order polynomial function is used in this case, as:

$$\frac{\langle u \rangle}{U_{cf}} = 1 - \left(\frac{z}{H} - 1 \right)^4, \tag{6.7}$$

where H is the height of the channel. The comparison of the channel flow inlet velocity profile with experimental data is shown in Figure 6.16.

This figure shows the mean streamwise velocity U/U_{ce} versus the location across the channel at $x/D = -3$ on the plane of symmetry $(y=0)$. U_{ce} is the centerline cross flow velocity which is equal to $1.20U_{cf}$. From the results presented, the turbulent incoming velocity profile agrees well with the experimental data.

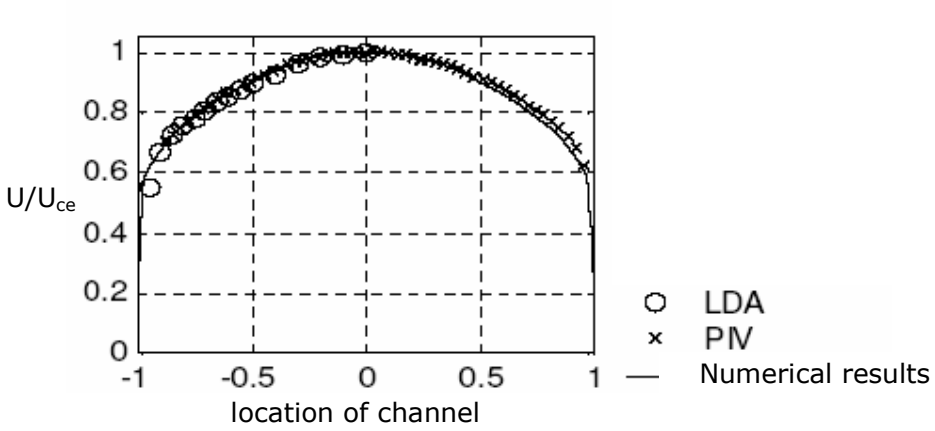

Figure 6.16: Comparison of inlet velocity profile of channel with experimental data

6.3.2 LES Results and Discussion

In order to achieve a fair assessment for the SGS scalar flux models, simulation results are compared to the experimental data. The validation procedure is carried at the symmetric profile. Figure 6.17 and 6.18 show the mean quantity of velocity which is obtained with dynamic Smagorinsky model. From the results, we can see that the LES results agree reasonably well with the experimental data. Especially, the PIV measure yielded detail spatial information of the flow. It showed a recalculating region in the lower half of the flow domain starting with the transitional region. These features are well reproduced by the LES. Comparing this result with Figure 6.11, the wall effect compresses the streamwise velocity and produce larger magnitude of the central line velocity at this direction.

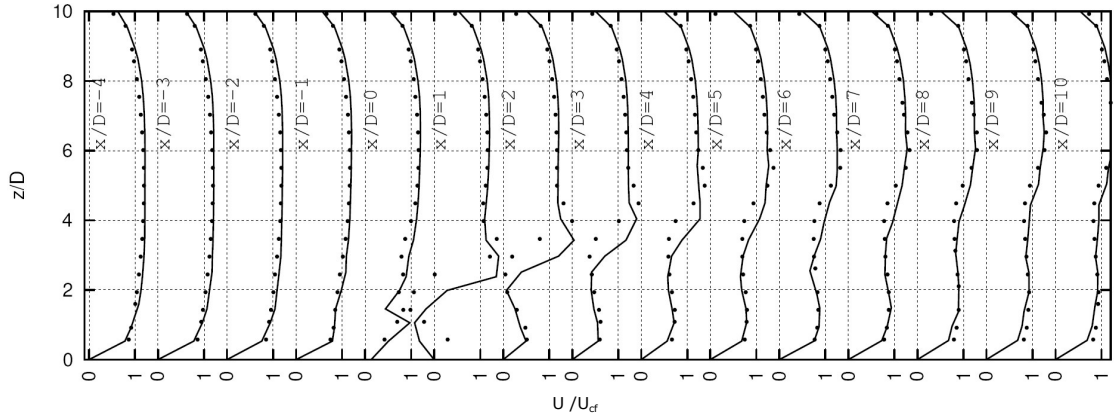

Figure 6.17: Normalized mean streamwise velocity versus experimental data

(—LES ···EXP)

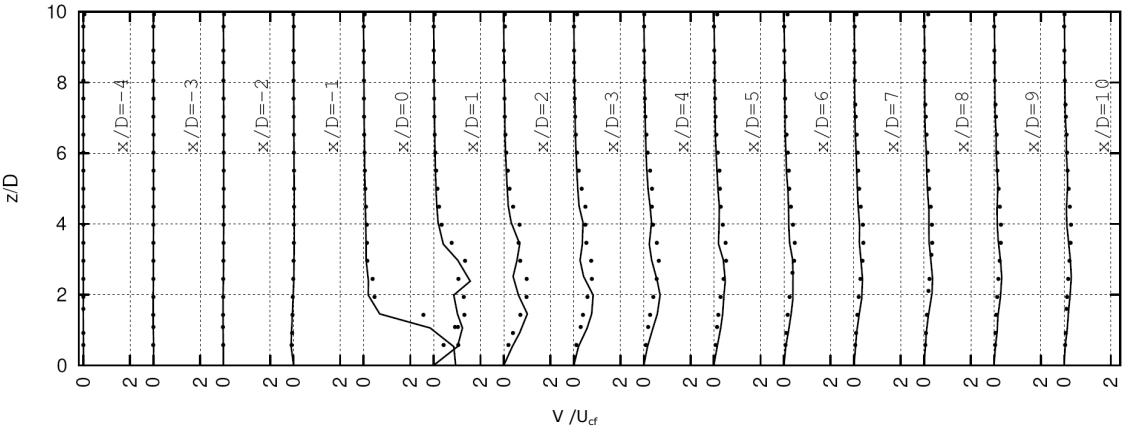

Figure 6.18: Normalized mean wall-normal velocity versus experimental data

(—LES ···EXP)

Let us now present and discuss the LES results for scalar field and classify the predicting ability of different SGS scalar flux models. The same classes of models combinations as in section 6.2 (see Table 6.5) has been applied, except for the case 3 as this performs similarly to case 2. Figure 6.19 shows the calculated values of mean mixture fraction against experimental data. It can be seen that the difference between case 1 and case 2 becomes larger in the wake the flow, the mixture fraction seems to be under-predicted while the qualitative agreement is quite good. This error may be ambilateral. In their paper, K.E. Meyer et al. specified the error for the mean mixture fraction as high as *3.5%*. On the other hand, numerical error may mainly depend on the veracity of SGS scalar flux models. The results of eddy diffusivity model with/without dynamic

procedure produces almost same results for the mean quantity while the anisotropy SGS model appreciably improves the results.

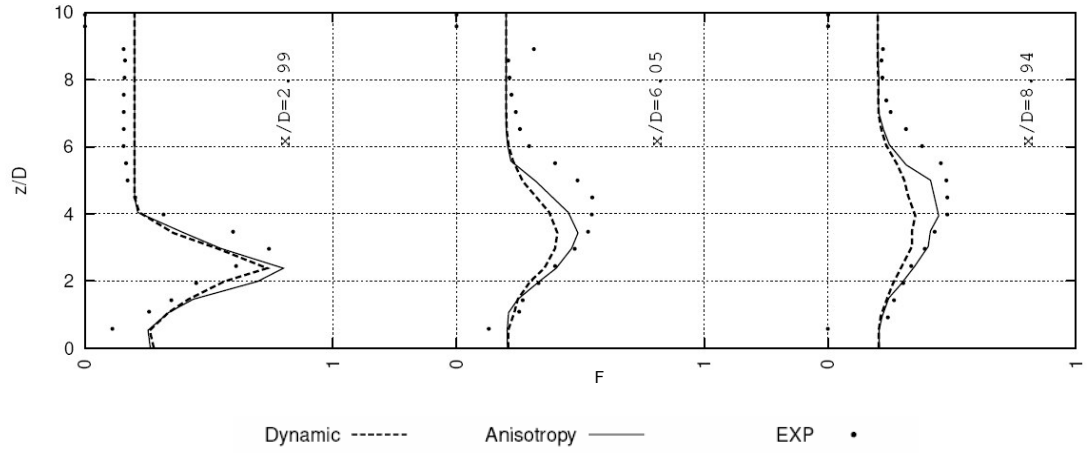

Figure 6.19: Comparison of mean mixture fraction *F* on the Symmetric plane

Concentrated on the most important modeled quantity, the scalar flux, the results obtained by different models are presented in Figure 6.20.

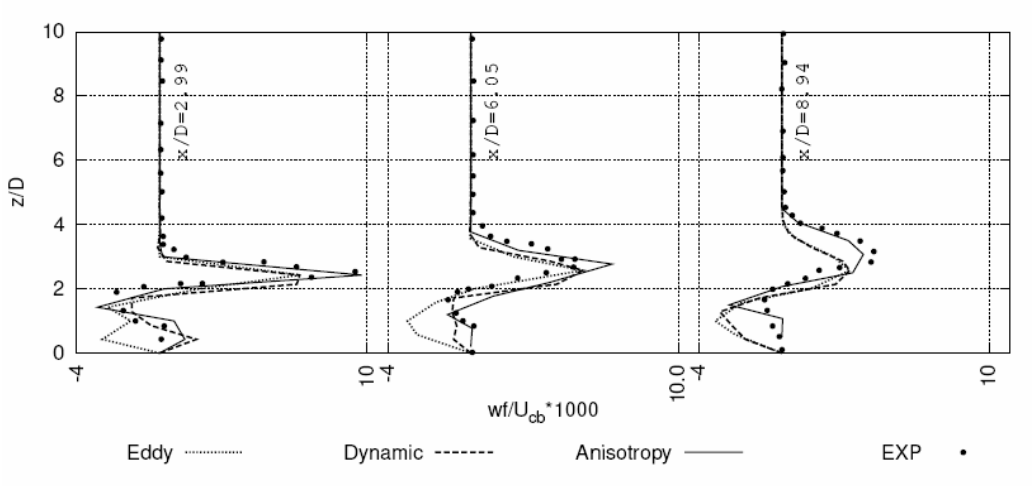

Figure 6.20: Normalized scalar flux $w'f'$ with different SGS models versus experimental data

We can see that the eddy diffusivity model with dynamic procedure (case 2) reproduces the experimental observations better than the traditional eddy diffusivity model (case 1). However, these two models both produce an over fluctuating phenomena near wall. In contrast, the anisotropy model is still more recommendable. In Figure 6.20, the anisotropy model (case 4)

shows a better predicting ability in terms of qualitative and quantitative statements. Comparatively, all other models overpredict the scalar flux at the near wall region and underpredict this quantity in the mixing region. Especially, the anisotropy model accurately grasps the maximum values of the scalar flux, whereas this achievement is appended by more computational cost. It can be mentioned here that a simple version of this anisotropy model has already used in which the empirical constant of the model coefficient has been set (M. Klein et al. 2003).

The simulation results with air for both the mean mixture fraction and fluctuation quantities are better than the case with water. The reason is twofold. First, the Reynolds number in the water case is low, so that the Schmidt number effect which disappears in general for high Reynolds number case, is present. Second, the SGS scalar contains more energy when molecular Schmidt number is larger than one (water). Then computational requirements to numerically solve these scales and thus accurately describe the mixing process are correspondingly increased. When the numerical treatment of air and water mixing keeps in the same level (as the simulations presented here), the results of air mixing are expected to be better than the water mixing. However, it appears that the anisotropy SGS model provides overall more accurate predictions.

Chapter 7
Mixing Analysis, Enhancement and Optimization

Most processes in which mixing is involved require that mixtures are efficient mixed prior to a chemical reaction or other further engineering process treatments. The degree of mixing strongly influences yield and purity of end product. For example, the design and performance of a gas turbine combustor requires good mixing characteristics to achieve high burning rates, low soot and oxides of nitrogen (NOx) formation, and exhaust temperature uniformity. Typically, however, most mixing processes are not running at optimal performance because the mixing has been neglected or designed incorrectly. Therefore, mixing analysis and control are of great importance.

To statistically analyze the mixing rate changes, various mixing parameters have been introduced in the literatures, e.g. [1], [37]. The ability of these parameters to retrieve the mixing mechanism is not clearly established. To acquaint with these mixing parameters, three parameters will be basically introduced and investigated in Section 7.1. They are “mixedness parameter”, which represents the probability of mixed fluids in computational domain, the Spatial Mixing Deficiency (SMD) and the Temporal Mixing Deficiency (TMD) parameters for characterizing the macromixing and micromixing.

These parameters will therefore be first evaluated in the mixing layer configuration. Then, they will be used to measure the development of mixing characteristics due to modifications of different handling conditions in the jet in cross flow configuration. The aim is to gain first insight in order to control and enhance the mixing process.

To this end, in Section 7.2, the resulting knowledge will be applied to optimize a mixing process in an impinging jet configuration.

7.1 Mixing Analysis and Enhancement

7.1.1 Mixing Parameters

A mixedness parameter, here denoted by MIX, similarly to the one proposed by A. Roshko 1976, is considered as a measure of the portion of the mixed fluids in the computational domain and formulated as:

$$MIX_{profile} = \frac{1}{n}\sum_{i=1}^{n} F_i(1-F_i). \tag{7.1}$$

$MIX_{profile}$ is the value of the parameter MIX on a cross section in the computational domain. F_i expresses the temporal average of the mixture fraction, where the subscript i refers to the number of grid points n on the cross section. Because the mixture fraction is bounded, $0 \le F \le 1$, the mixedness parameter $MIX=0$ and $MIX=0.25$ for the completely unmixed and fully mixed fluids on one cross section, respectively.

As noted in Chapter 3, two important length scales, the scalar integral scale $L_{\phi I}$ and Batchelor Scale $L_{\phi B}$, allow to describe two levels of turbulent mixing of an inert scalar: the macromixing (in the range of integral length scales) and micromixing (between the Taylor microscale and Batchelor length scales), respectively. The first occurs due to resolved (or mean) transported structures of velocity spectrum, while the second is controlled by scalar gradient correlations as expressed through the (molecular), dissipation of scalar variance near the Bachelor scale. In the case, the scalar integral scale is less than the turbulent integral scale (in the range of Taylor microscales), the mixing process is known in chemical reaction engineering as mesomixing to emphasize the fact that it occurs primarily due to the turbulent fluctuations in the energy-controlling range of the velocity spectrum.

As the scalar integral scale characterizes the largest structures in the scalar filed, the macromixing or large scale mixing is therefore influenced by these structures. In another word, a spatial description of these resolved structures can provide measure of the macromixing that therefore can be described as the process at which a non-uniform scalar system is made at large scale level.

A measure of uniformity is the so-called Spatial Mixing deficiency (SMD) or Coefficient of Variation (CoV) which is the ratio of the standard deviation in mixture fraction and the cross-sectional average of mixture fraction. It can be expressed as (A. Bakker et al. 1998):

$$SMD = \frac{\sqrt{\sum_{i=1}^{n}\left(F_i - F_{profile}\right)^2 \Big/ n-1}}{F_{profile}}, \tag{7.2}$$

where $F_{profile}$ denotes the cross section averaged mean mixture fraction. A smaller value of SMD means a better macromixing.

To describe the micromixing, it is necessary to consider the process at molecular scale level. If we rely to the scalar energy spectrum where besides the resolved structures, account must be taken for the non-resolved part, i.e. the inertial convective, viscous convective and viscous diffusive subranges of spectrum. This means that the effects of the molecular diffusivity and viscosity on the rate of turbulent mixing must be included. This can be achieved by including fluctuations and their local time variations. To account for this effect, a Temporal Mixing deficiency (TMD) is introduced as the ratio between the cross-sectional average of the mixture fraction fluctuations ($f'_{profile}$) and the cross-sectional average of the concentration (R.B. Bird et al. 2002):

$$TMD = \frac{f'_{profile}}{F_{profile}} \text{ with } f'_{profile} = \frac{1}{n}\sum_{i=1}^{n} f'_i . \tag{7.3}$$

The parameter used to describe the macro-mixing can be normalized by the largest value, SMD_{max}, as:

$$SMD\big|_{\text{normalized}} = \frac{\frac{1}{n}\sqrt{\sum_{i=1}^{n}\left(F_j - F_{profile}\right)^2} \Big/ F_{profile}}{SMD_{\max}}, \tag{7.4}$$

so that the normalized SMD value will vary between one and zero. One means the beginning status of mixing and zero means that the mixture on the investigated profile already reaches uniform. This normalized procedure is aimed to gain better understanding when this parameter is applied and compared in different mixing processes (e.g. by changing the handling parameters, Section 7.1.3).

Same explanation can be converted to normalized TMD as:

$$TMD|_{\text{normalized}} = \frac{f'_{profile} \Big/ F_{profile_i}}{TMD_{\max}}. \tag{7.5}$$

7.1.2 Mixing Layer Configuration: Mixing Evaluation

To begin the mixing evaluation on the mixing layer configuration, a picture of instantaneous mixture fraction and absolute velocity is presented in the Figure 7.1 for giving a visible idea.

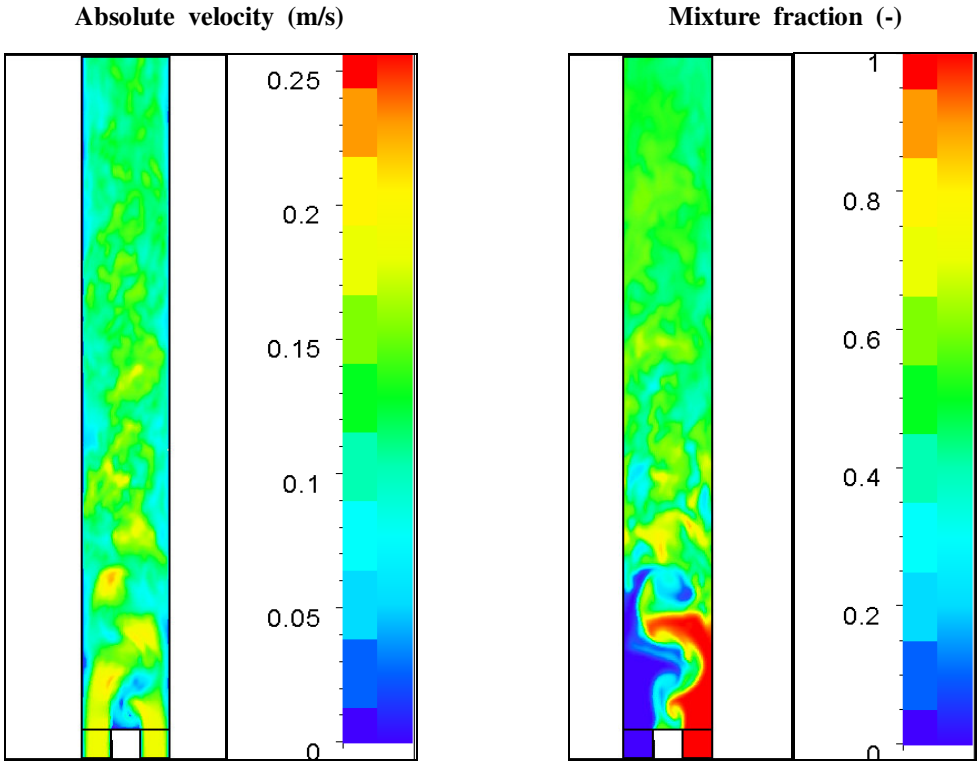

Figure 7.1: Instantaneous mixture fraction and absolute velocity at symmetric profile of the mixing layer configuration

It can be seen that the scalar is inhomogeneously distributed in the initial mixing zone, except for an area right behind the block. Further out in the channel the scalar distribution is more homogeneous. It can also be seen that the distribution of the scalar and the velocity vectors are very closely related. In the flow right behind the block dividing the two streams, there is a zone where the two streams are mixed fairly well compared to further out in the channel. The

recirculation zone that is produced here due to the block causes an increased mixing effect. Applying equation (7.2) and equation (7.3) to describe the macro and micromixing, Figure 7.2 displays the SMD and TMD results. The SMD is expected to start at a high value and decrease along the length of the channel. But as can be seen it increases from *z/D=0* to *z/D=0.5*, this is due to the recirculation zone right behind the block, where there is an increased mixing effect as shown earlier. From *z/D=0.5* it decreases as expected until *z/D=5*, afterwards the macromixing doesn't show any improvement. The TMD result keeps decreased after this point which means micromixing is more active than macromixing at wake of the flow.

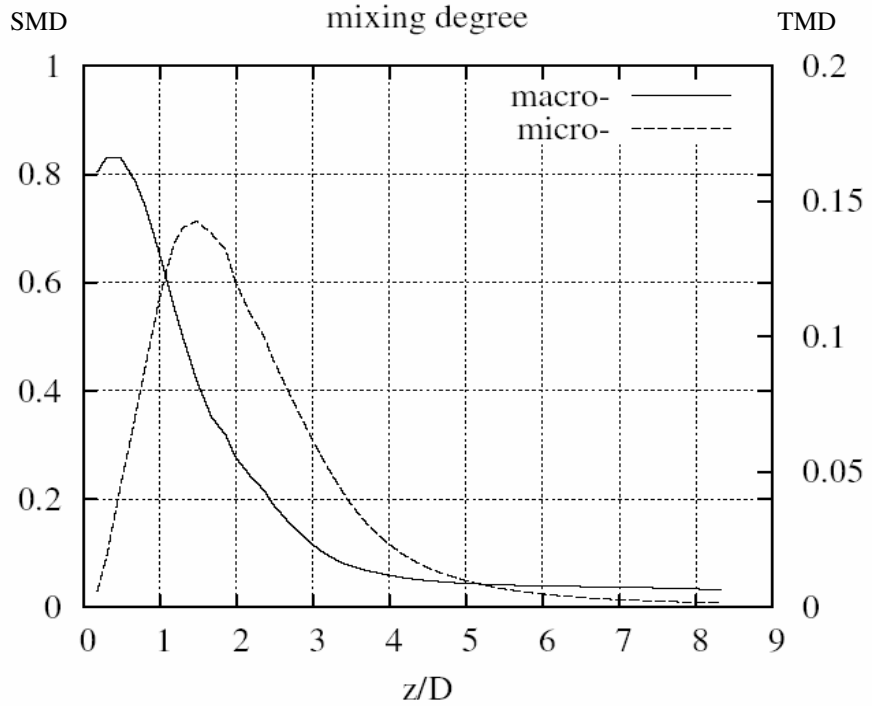

Figure 7.2: Marco and micromixing evaluation (SMD, TMD) of the mixing layer configuration

7.1.3 Jet in Cross Flow: Mixing Enhancement

To control or enhance the degree of mixing, in general, two different approaches can be applied. The first is to change the internal conditions such as flow boundary conditions (active modification). Another is by varying the external conditions, for example, the geometrical parameters (passive modification). In this section, an exemplification study on the jet in cross

flow configuration is carried out for mixing enhancement using active and passive modifications.

Inflow Conditions: Active Modification

a. Velocity Ratio: Different inflow conditions, e.g. different flow Reynolds numbers or velocity ratios of *0.5, 1* and *2* are performed. In Figure 7.3 different paths of the jet flow (iso-surface with $f = 0.5$) after exiting from the pipe are shown.

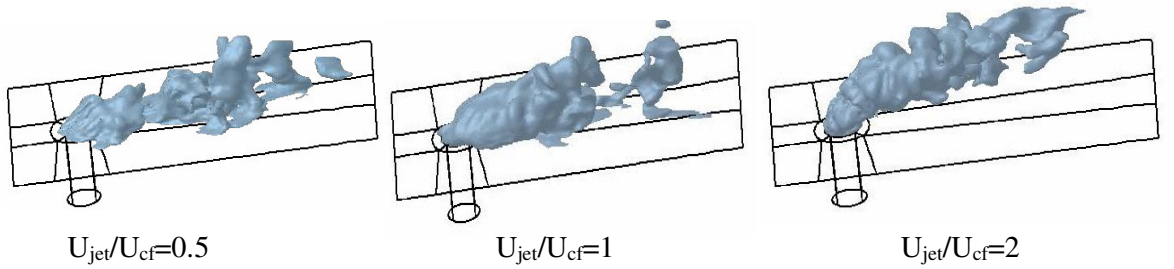

Figure 7.3: Iso-surface of mixture fraction after jet flow exiting from the pipe

The figure presents a visible idea of the jet flow developing from different inflow properties. With the low velocity ratio, the jet flow just climbs along the wall, so that a strong interaction between the wall and jet flow takes place. For the higher velocity ratio, the flow becomes fully developed and the influence from the wall is no more significant. Figure 7.4 shows the value of MIX along the streamwise direction for the three situations. The amount of the mixed fluid increases monotonically, so that larger mixing is observed in the wake of the flow due to larger front excursions. It can also be seen that, the lager velocity ratio brings larger MIX because the increased inlet mass flow of jet produces more mixed fluids.

There is a so-called maximum mixing position shown in Figure 7.4, thereafter the value of the mixedness parameter keeps almost unchanged. Even though the final values of MIX are distinct for three different velocity ratios, they reach the maximum mixing almost at the same position ($x/D=3$) in the streamwise direction. This result may bring important information for design purpose, which relies on the length at which the maximum mixed fluid can reach. After the position the value of MIX remains constant expressing an unalterable probability of the presented of mixed fluids involved in the computational domain.

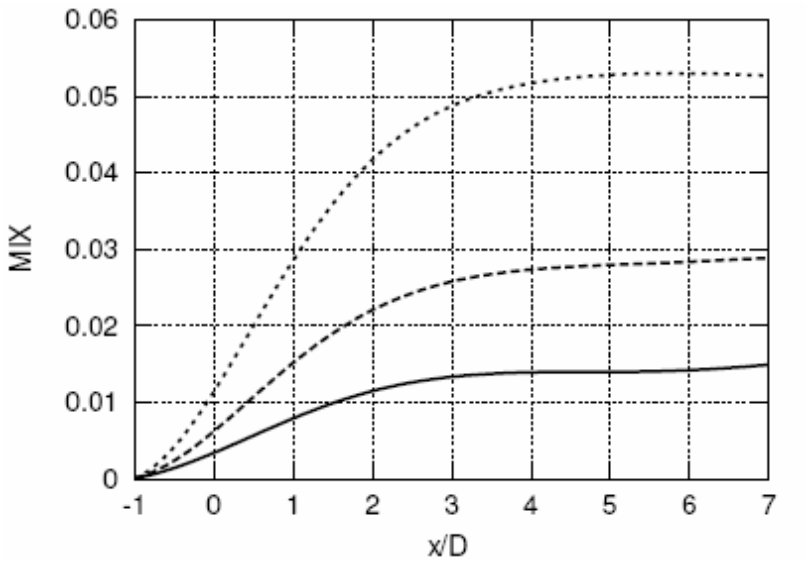

Figure 7.4: MIX values along streamwise direction for different inflow conditions

(— U_{jet}/U_{cf}=0.5 --- U_{jet}/U_{cf}=1 ····· U_{jet}/U_{cf}=2)

The normalized SMD results are smaller for the case with higher velocity ratio, which consists in the fact that the full-developed flows have a tendency towards homogeneous status of mixture. At *x/D=3*, even the probability of mixed fluid is constant, the macromixing is not yet fully homogenous. The two flows interact with each other at the same rate. This unsteadiness keeps SMD decreasing which means an ongoing macromixing process, see Figure 7.5.

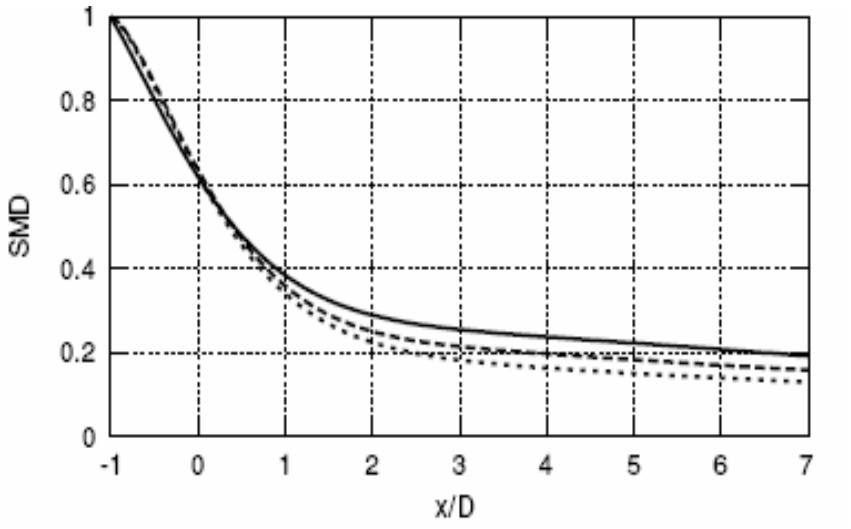

Figure 7.5: Normalized SMD values along streamwise direction for different inflow conditions

(— U_{jet}/U_{cf}=0.5 --- U_{jet}/U_{cf}=1 ····· U_{jet}/U_{cf}=2)

b. Jet Swirling Number: This is confirmed by modifying the jet inlet properties by swirling the jet flow with different swirling number (*0.5* and *1*). The swirling number is calculated as [95]:

$$Sw = \frac{\int_0^R U_{ce} W_\theta r^2 d_r}{\int_0^R R U_{ce}{}^2 r d_r} \text{ with } \quad W_\theta = \frac{a_1}{R}\left(1 - \exp\left(-a_2 R^2\right)\right), \tag{7.6}$$

where R is the radius of the jet and U_{ce} is the centerline velocity on the inlet. Here a_1 and a_2 are empirical constants. The MIX results for different swirling number are plot in Figure 7.6 a. From this figure, the mixedness parameter gains larger value with higher swirling number between the positions *x/D=0* and *x/D=2* downstream because the swirling causes an increasing interaction area between the swirled jet and the cross flow. The maximum mixing position is also shifted to the nozzle direction. Behind *x/D=2* downstream, the swirl intensity seems to have no influence with increasing swirling number. The MIX tends quickly to reach the same maximum value expressing the steady mixed fluid portion in the computational domain. This is expectable, because the involved fluid mass stream is the same for these cases resulting in the same portion of the mixed fluid at the wake of flow.

The normalized SMD results, see Figure 7.6 b, show the same tendency. From the definition, SMD is counting the sum of scalar gradient with regard to the mean value over a profile. The inflow perturbation (swirl) can not produce significant influence on the sum. Therefore, from the SMD results, the difference can be visible only near jet brim area. Once the flow is far from this region, the SMD results become coincided for the three situations. This means this kind of inflow perturbation can not influence the overall macromixing.

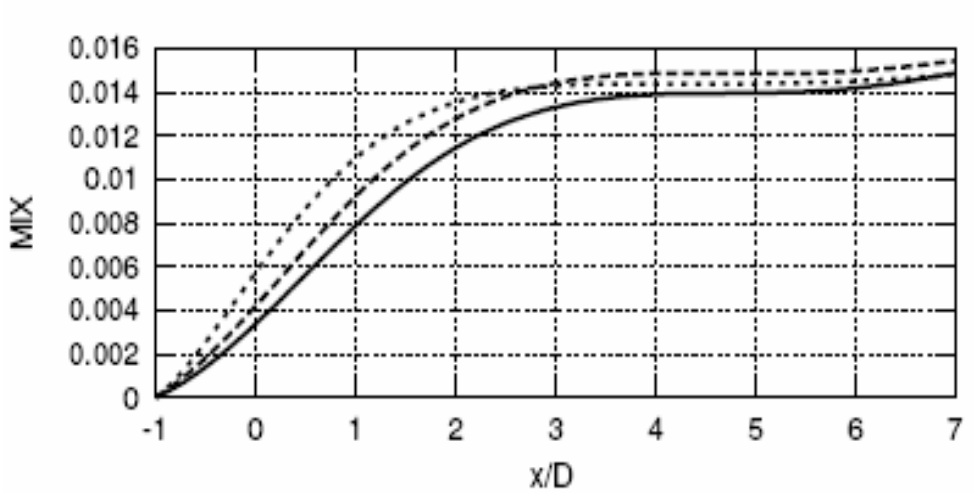

a.

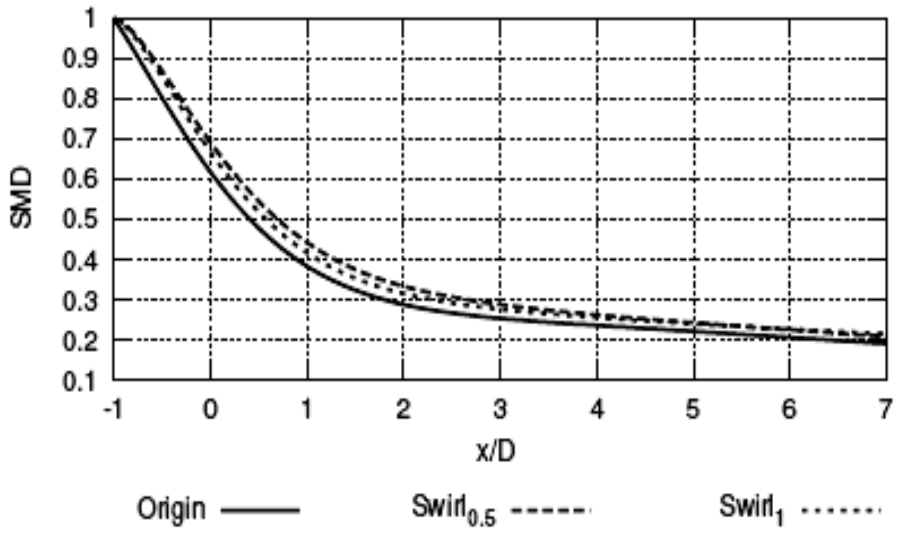

b.

Figure 7.6: Mixing parameter results for different inflow swirling numbers

a. MIX; b. Normalized SMD

Geometrical Conditions: Passive Modification

In the following, the evaluation of the mixing enhancement is accomplished by changing the geometrical parameters. Because of geometry modification, the probability of mixed fluids in computational domain is no more illustrative. Macro and micromixing indices therefore are used as measures.

In work of B. Wegner et al. 2004, different mixing processes are investigated by varying the jet angles. In this thesis, a passive mixing enhancement technique is employed by locating an obstacle structure (tab). The obstacle locates at different positions downstream the jet exit to alter the trajectory and mixing characteristics of the flow. Besides the tab positions, the height and pitch of the tab are important parameters. In general, the increase in the tab height increases the turbulent mixing for an open configuration but raises the pressure drop. The optimum height of the tab is assumed to make the trajectory of the jet flow through the middle of mixing region. There also exists an optimum pitch, since it should be longer than the recirculation zone formed behind the tab. More information about these two parameters needs detail structure studies as reported in [31].

The complex flow structures, for the low velocity ratio situation, are stemmed from the strong interaction between the jet and the cross flow near the flat surface, where the counter-rotating kidney-shaped vortex pair yields the negative streamwise velocity, see Figure 7.7 a. This negative streamswise velocity approximately begins from the position at $x/D= 0.5$ and ends at $x/D= 2$. With regarding to this flow structure, one can locate a tab inside the vortex structure in order to enhance it or after it in order to produce another vortex structure. It therefore necessitates two simulations: first computation with closer tab at the position of $x/D=1$ and another simulation with a farer tab located at $x/D=2$, see Figure 7.7 b.

From the statistical results, at $x/D=1$, the negative wall normal velocity at the symmetric profile lies from $y/D=1$ to $y/D=0$ and thus the tab used is designed with height and width of the same order of magnitude: $H/D=W/D=0.5$. Figure 7.7 b is the instantaneous mixture fraction with a tab structure at different positions.

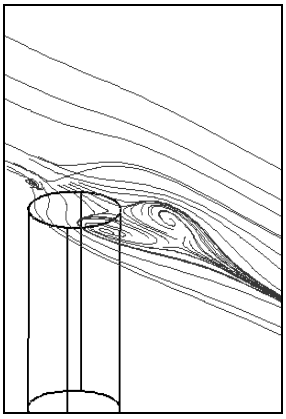

a.

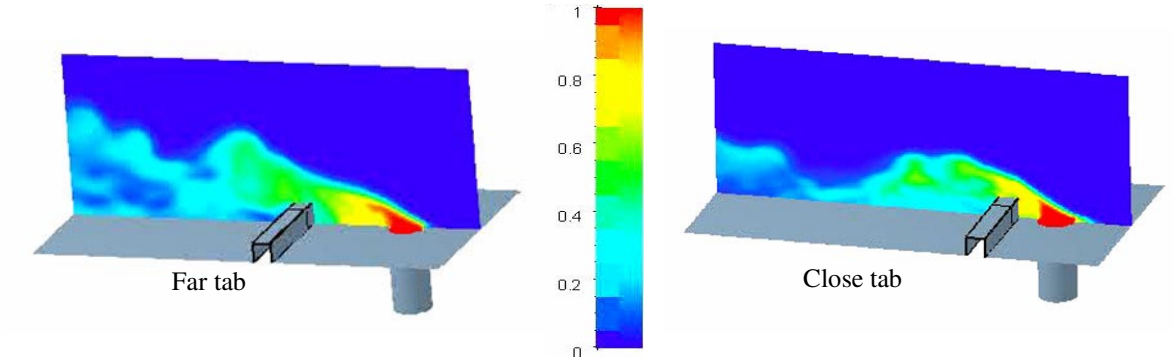

b.

Figure 7.7: Enhancement of the mixing process with an obstacle (tab) structure

a. Counter-rotating kidney-shaped vortex in the jet in cross flow configuration;

b. Instantaneous mixture fraction with a tab structure at different positions

The normalized SMD and TMD results for these situations including a no obstacle case are presented in Figure 7.8. Because the obstacle disturbs the flow structure and thus produces more scattered and back flows, in general, this modification can increase the degree of mixing processes in terms of macromixing (see SMD).

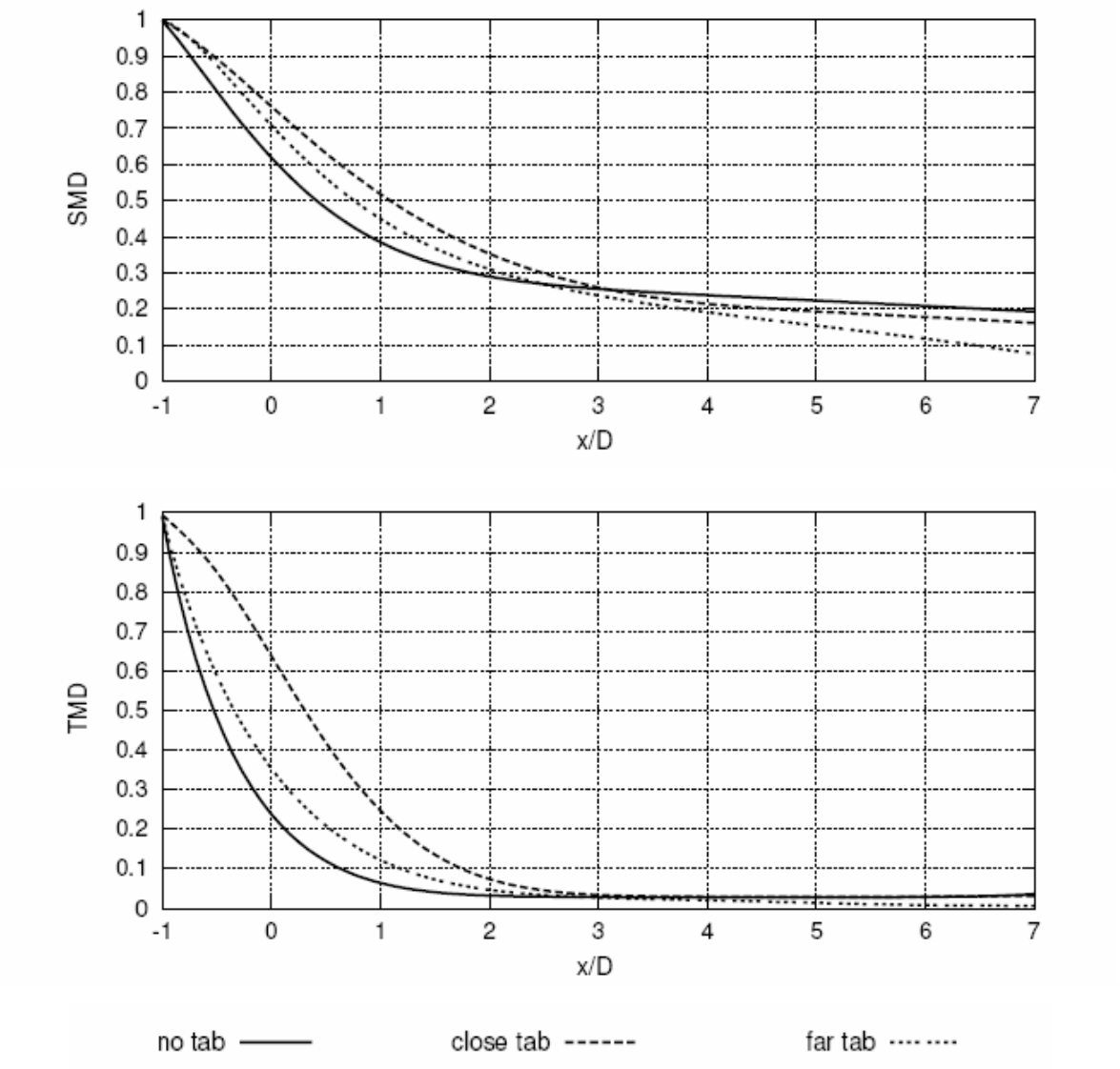

Figure 7.8: Normalized SMD and TMD reuslts with a tab structure at different positions

The results of SMD prove that the farer tab structure can produce a further macromixing at the wake of the flow compared to the closer tab. It dues to this structure is located at the position where the macromixing almost reaches steady (see the no tab case) and it disturbs flow structures producing “a second mixing” at the wake of the flow.

However, the TMD results show another tendency. Because the TMD calculation handles the variations of local fluctuation, the instabilities are revealed by TMD results. In Figure 7.8, the TMD results with tab structure are larger than the no-tab case before the tab position. The phenomena may because the tab structure will influence the unsteady behavior of the flow, which produces larger magnitude of the fluctuation. While at the wake the flow, the TMD results

approach to the same value. This reveals that, by this kind of passive modification, the enhancement of macromixing is better than of micromixing

7.2 Mixing Optimization

Process optimization is similar to troubleshooting, it can be applied in the area when one is trying to control the mixing processes or want to learn more about mixing, mixing application, nomenclature or mixer components.

The mixing optimization through experimental and empirical studies based on trial and error may have high consumption on money and time. Experimental methods to evaluate mixing in real time would allow, for example, optimal mixing conditions to be determined for a mixer. It is rather expensive and hard to be extended, as the scale–up is sometimes difficult for complex flow configurations. As computing power continues to increase and mixing simulations become more practical, numerical optimization as first step is very promotional. It can coinstantaneous help with the experimental plan, the experimentation or design.

The optimization is to find the best values of the design (flow) variables that minimize or maximize the objective functions while satisfying constraints.

Objective functions and constraints: In mixing processes, increasing the mixing rate is accompanied with increasing the pressure drop, the energy input and mixing efficiency. Thus the energy input and SMD/TMD may be adopted as the objective functions. In practical situations for a mixer design, however, it is generally required that the minimum scalar variance should be maintained under the desired one. Thus, the minimum variance (or gradient of SMD/TMD) is used as one of constrained condition while the SMD/TMD is adopted as objective function in this work.

In the section below, a general mixing optimization procedure is introduced and carried out in an impinging jet configuration. Although the principal focus is a specific impinging jet problem, the methodology developed is equally applicable to virtually any other aspect of technology and engineering, where mixing processes are important.

7.2.1 General Optimization Procedure

Figure 7.9 shows a flow chart of genetic procedure for estimating an optimal design parameter.

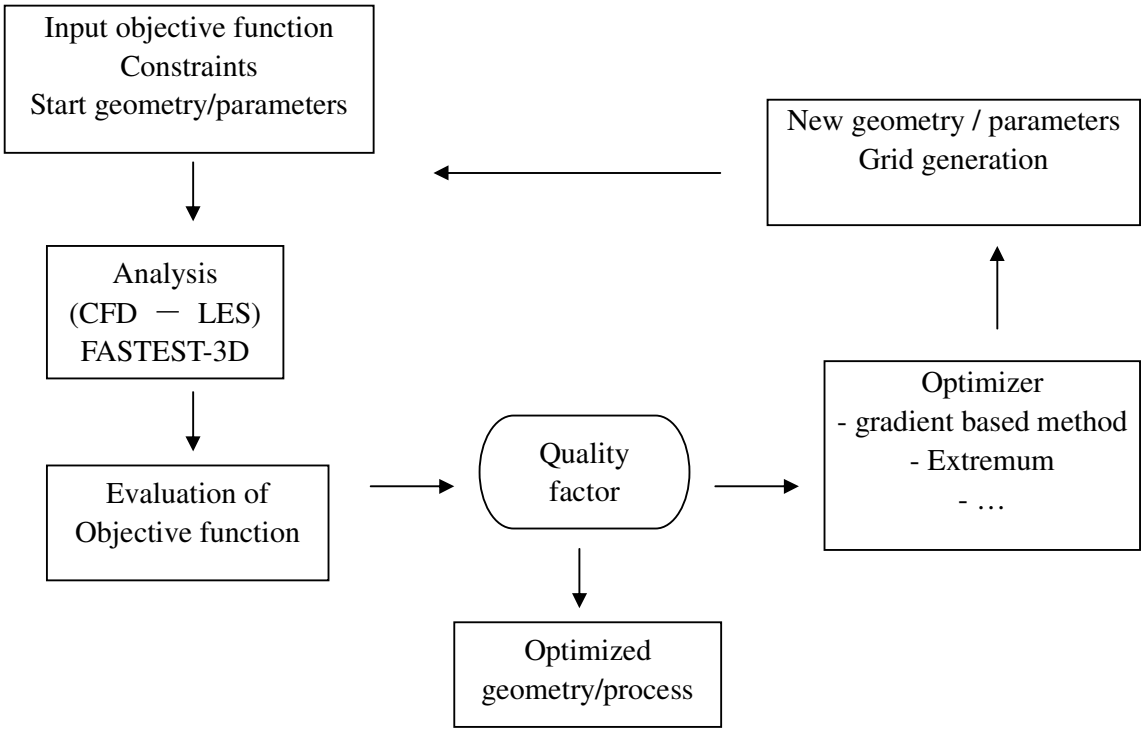

Figure 7.9: A general mixing optimization procedure

The procedure begins with input needed to define objective function. We deal with an original mixing system, which includes the parameters describing the flow and mixing conditions as well as a start geometry. Because physical problems are described by relations, which are dominated by quantities that have a certain dimension, such as length, time, mass, force, temperature etc., the practical mixing problems will be restricted by some constraints. With these initial conditions, different CFD-computations can be introduced in order to get the simulation data to perform the needed analysis. In this work, LES with FASTEST-3D code is performed. Firstly, the simulation results are usually compared with reference data (e.g. experimental data) to insure the model and numerical code working in an accurate way. Then, with the accurate results, the objective function (here SMD) can be evaluated. This objective function is then compared with the quality factor, which can be treated as system criteria or constraints. It defines, for the problem

concerned, the mixing degree required in the practical situation.

The comparison between the objective function and quality factor may inform that the original system already reach the requirement. If not, a new design is proposed and a new simulation must be performed to get the value of the objective function. This is normally achieved by an optimizer.

Optimizer is a series of statistical and mathematical techniques. It utilizes data by numerical computations or experiments and constructs response objective function by interpolating the data. It has ability to reduce the number of simulations.

Following the suggestions of the optimizer, some flow parameters or geometry parameters have to be changed. Thereafter, a new simulation based on these adjustments will be performed and corresponding results will be available. The repetitions on this loop will lead to find an optimal design value with which mixing can reach the system requirement (quality factor). The function evaluation by means of LES, in general requires much computational cost to reach final optimal results.

In this work, this general procedure is applied to a specific problem — the impinging jet configuration described below.

7.2.2 Mixing Optimization of a Impinging Jet Configuration

This is an example of a mixing-dominated problem. Impinging jet mixers are widely used in industrial processes such as reaction injection mold, crystallizations and precipitations, and detergent neutralizations. Due to the rapid reactions that occur in these processes, inefficient mixing can also lead to a chain of related undesirable consequences: desired reactions are slowed, selectivity is decreased, and the accumulation of unwanted byproducts is increased. It is thus clear that mixing has a large impact on both product quality and process profitability.

Different techniques (e.g. [29], [42] and [90]) therefore have been employed to examine the performance of impinging jets in an attempt to achieve a fundamental understanding of mixing in these systems. Even though different mixing statuses have been identified in this configuration, the optimal mixing is still an open question.

The numerical study aimed at finding an optimal mixing with various design parameters. The

numerical set up of impinging jet mixer is based on the experiments of D. R. Unger & F. J. Muzzio 1999. Basic geometer parameters are presented in Figure 7.10. The mixer was experimentally constructed with glass.

Five profiles indicted in Figure 7.10 are investigated within the mixer. Vertical cross-sections are used rather than horizontal cross-sections, because in many mixing systems such as stirred tanks radial symmetry exists and segregation most often occurs in the axial direction. Thus, uniformities in the mixer can be clearly observed within a single cross-sectional image.

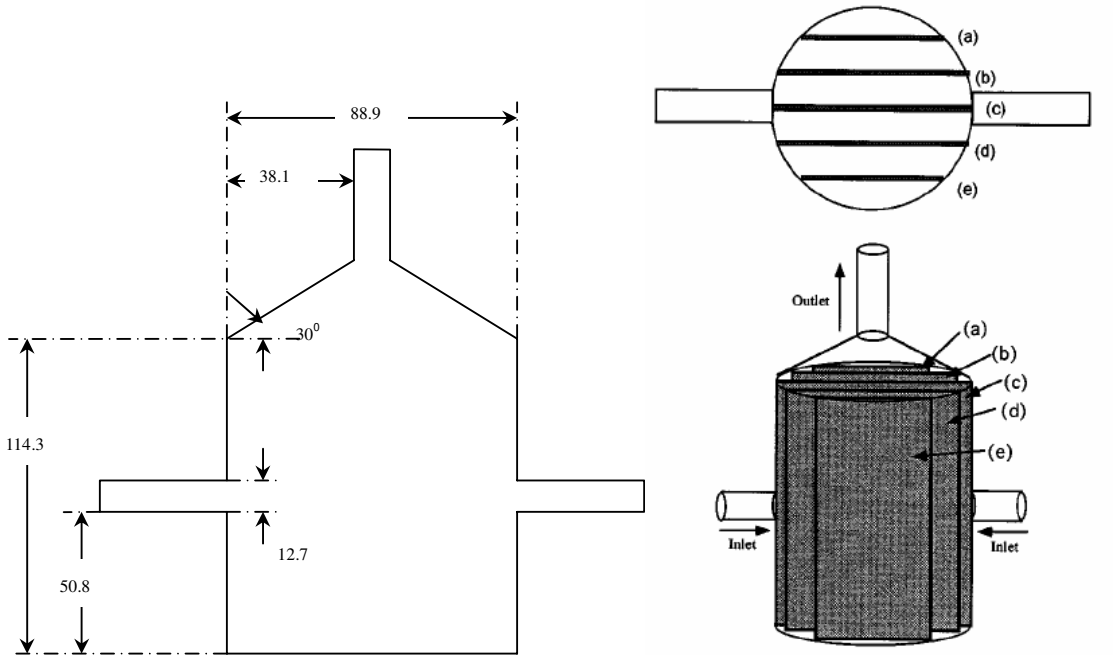

Figure 7.10: Basic geometric parameters (in mm) and the investigated cross-sections of the impinging jet configuration

Cross-section (a). 30mm behind the jet axis; (b). 15mm behind the jet axis;

(c). through the jet axis; (d). 15mm in front of the jet axis; (e). 30mm in front of the jet axis

Simulation is performed with jet Reynolds number $\mathrm{Re}_{jet} = 150$ based on the jet bulk velocity and diameter of the entrance jet.

With utility of FASTEST-3D code, LES are performed on this configuration with dynamic SGS model both in the velocity field and scalar field with total CV *428100*. The computational cost of the anisotropy model does not allow its use for this purpose. The same consideration leads to the restriction on this grid resolution. Since the objective function only needs the mixture fraction data, we concentrate on this quantity. The result presented in Figure 7.11 is a comparison of

mean mixture fraction on the symmetric profile with experimental results. The consistent results permit further analysis based on the numerical setup.

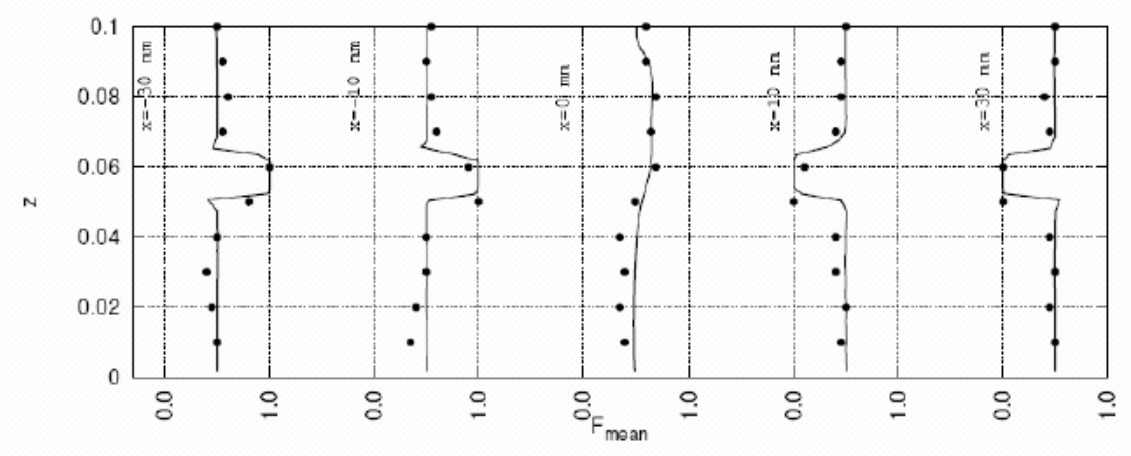

Figure 7.11: Comparison of mean mixture fraction on the symmetric profile

(—LES ···EXP)

For giving a visible idea of the mixing process, representative examples of the mean mixture images obtained by simulation with the impinging jet geometry are shown in Figure 7.12 at different vertical cross-sections.

The figure shows large regions of unmixed fluid exist in the mixer for $\mathrm{Re}_{jet} = 150$. Since the convective motion of fluid is slow in the bottom half of the mixer (below the jets), some of the fluid in the bottom of the mixer is entrained in recirculation regions, thus providing additional time for diffusion to complete the mixing process. Therefore, although some regions near the bottom of the mixer appear well-mixed, the mixing rate in these regions may be much slower than required by the reactions of a given process.

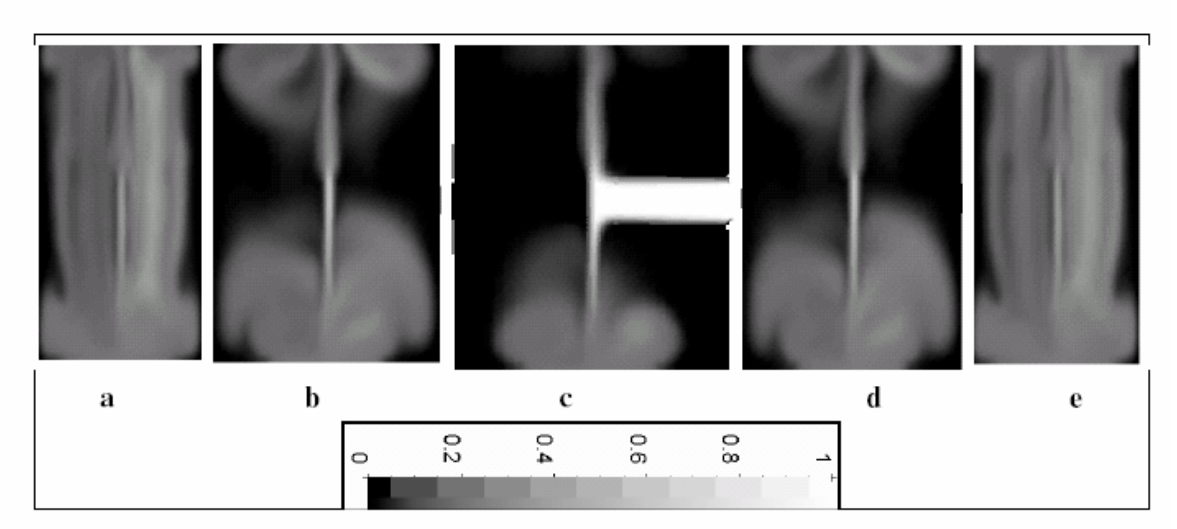

Figure 7.12: Mean mixture fraction images for impinging jet configuration at Re_{jet} = 150
Cross-section (a). 30mm behind the jet axis; (b). 15mm behind the jet axis;
(c). through the jet axis; (d). 15mm in front of the jet axis; (e). 30mm in front of the jet axis

After obtaining the simulation results, the next step should be the evaluation of the objective function. As mentioned above, in a mixing process, the knowledge mixing efficiency (spatial or temporal) is necessary. To make the problem simple and consistent, SMD is used throughout this chapter. Therefore, the SMD is averaged for each of the five cross-sections resulting in $SMD = 0.13$ for the original design.

It is to mention that most industrial blending operations can be satisfied with a SMD of five percent (*SMD = 0.05*). However, some applications may require coefficients of variation of one percent or less (*SMD<0.01*) [1]. By considering the *SMD=0.13* for the original impinging jet, which is larger than *0.05*, it turns out that the mixing process described above can not directly apply to engineering practices. It therefore requires techniques that address to develop and propose a new design to optimize the mixing in this configuration.

In an impinging jet configuration, the relative design variables are listed in the Figure 7.13.

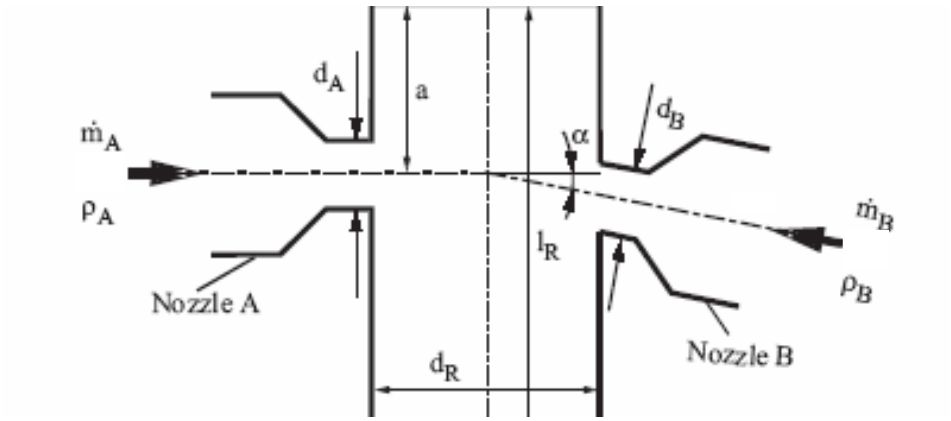

Figure 7.13: Design parameters for mixing processes within an impinging jet mixer

To sum up, the design parameters are classed into flow conditions, such as the inflow conditions; flow properties, such as density, mass flow rate $\dot{m}$, etc.; and the geometric parameters such as jet angle α and the size of mixer, e.g. *a, d_A*. These parameters which strongly influence the value of SMD can be related to SMD in the form of

$$SMD = f(d_A, d_B, d_R, \alpha, a, m_A, \rho_A \cdots) . \tag{7.7}$$

Thus the optimization problem considered in this study can be expressed as to find $\{d_A, d_B, d_R, \alpha, a; m_A, \rho_B \cdots\}$ that minimize SMD subject to the specific constraints, e.g. $grad(SMD) \le 0; -90^o \le \alpha \le 90^o$, etc.

To choose which parameter has to be adjusted in $\{d_A, d_B, d_R, \alpha, a; m_A, \rho_B \cdots\}$, practical analysis and requirements have to be taken into account. In the impinging jet configuration, the statement of the experimental work shows that the mixing is related to the jet angle *α*, because the jet angle influences the flow recirculation. It is then reasonable to choose jet angle as one of the design parameter to be adjusted in order to reach optimal mixing. The remaining parameters are kept as constants to simplify the problem. Physically, the jet angle can vary from *-90* degree to *90* degree. Together with minimum variation of SMD, these conditions constitute constraints of this optimization task.

It is almost impossible to simulate the whole range of angles with available computational resource. It is therefore practical to choose several angles as samples. The first choice was to move the angle directing up, *α=-40*. With this jet angle, new numerical grids are generated and

simulation has been started as beginning geometry simulation. Different variations have been considered (α= 40°, 70° and 80°). The resulting evaluation of the objective function is displayed in Figure 7.14.

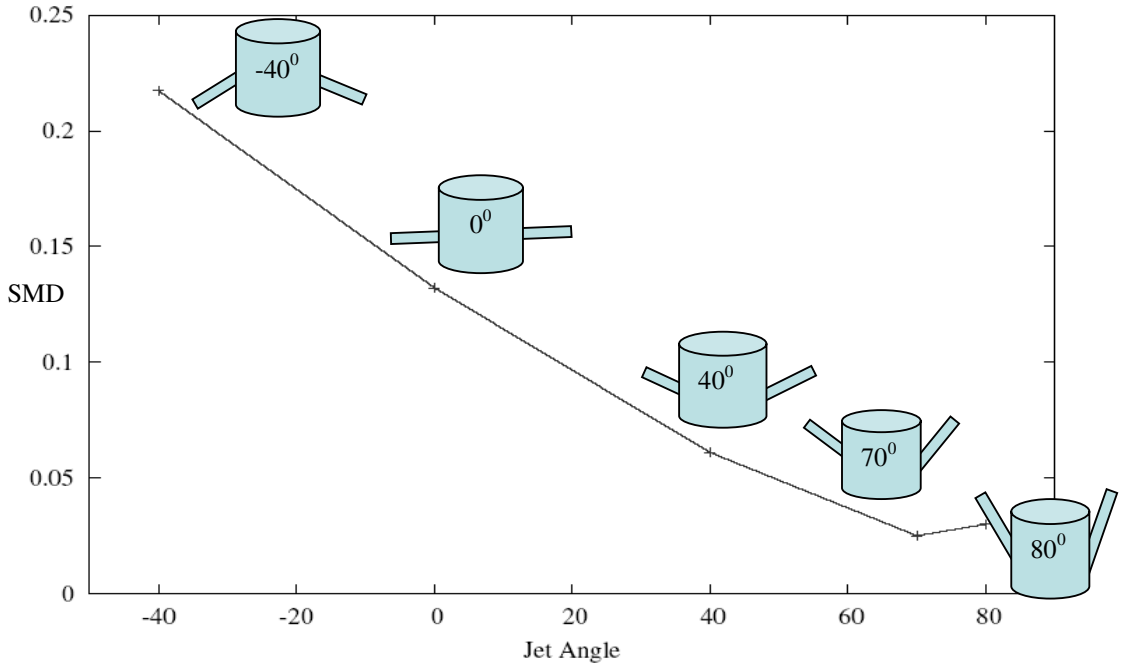

Figure 7.14: SMD results based on different jet angles of the impinging jet configuration

Figure 7.14 presents the SMD results as a function of jet angle α. This function can be approached by a polynomial form as:

$$SMD(\alpha^*) = \sum_i x_i \alpha^{*i}, \tag{7.8}$$

where x_i is the ith order function coefficient and α^* is the normalized angle by $\alpha = 1^0$ in order to make α dimensionless. With the five known values in Figure 7.14, the function can be approximated primitively as:

$$SMD(\alpha^*) \approx 1.2 \cdot 10^{-9} \alpha^{*4} - 2.1 \cdot 10^{-8} \alpha^{*3} + 1.1 \cdot 10^{-5} \alpha^{*2} + 1.6 \cdot 10^{-4} \alpha^* + 0.14. \tag{7.9}$$

More sampling points can reduce the approximation error while every point means a new LES. A higher accuracy requires more simulation time. Because the numerical optimization results can be tested and improved in practical setting, the fifth order error is acceptable. The conditional relative extremum in the range from *-90* to *90* is from these simulations with

$$Grad(SMD(\alpha^*))\Big|_{-90\le\alpha\le90} \sim 0, \tag{7.10}$$

achieved with

$$\alpha^* \sim 72. \tag{7.11}$$

This means the minimum SMD result can be approached when the angle α is around 72^o. Thereby, the resulting SMD (*SMD=0.02*) value is around *15%* SMD of the original mixer (*SMD=0.15*) and satisfies the quality factor (*SMD = 0.05*).

7.2.3 Conclusion

This study outlined a general procedure to perform the mixing optimization. It has to be noticed that such technique may be highly time consuming. Because of the time consuming LES, a full loop of mixing analysis is hardly to be performed especially for a complex mixing system. Reduced information about required mixing quantities will be necessary.

Chapter 8
Conclusions

This thesis focuses on the numerical simulation of three-dimensional turbulent mixing processes using Large-eddy simulation (LES) technique. LES has been conducted to explore the stages towards an accuracy description of mixing processes. A systematic evaluation of SGS scalar flux has been carried out. Classical SGS models for the turbulent flow field and scalar field has been considered. In particular a new formulated SGS scalar flux mode, so called "anisotropy model", has been introduced. It is designed to consistently describe the turbulent mixing transport processes even in complex configurations. Table 8.1 summarizes the SGS models combination accomplished in this work. The entire SGS models have been implemented in FASTEST-3D code. The validation has been performed in three configurations with increasing complicity.

Subgrid stress	Subgrid scalar flux
Germano/Lilly model (1991, 1992)	Eddy diffusivity model (1985,1990) Dynamic procedure based model (1991) Scale-similarity models (1980) **Anisotropy model (2004)**

Table 8.1: Different SGS models combinations implemented in this work

The first configuration concerned a mixing layer in a confided channel. Besides the evaluation of different SGS models, the investigation of this configuration aimed at demonstrating once again LES as a researching and industrial CFD tool to capture mixing process. A sensitivity study of LES was carried out in terms of grid resolutions, boundary conditions and time-averaging processes. To obtain accurate results, these issues must be carefully considered. We found, for LES applied in scalar filed, that even the main procedure is similar as in the flow filed, additional

considerations of the grid resolution suitable for scalar are necessary because the energy spectrum can be different depending on the molecular Schmidt number. With regard to the mixture fraction, the boundary treatment is very simple. A correct description of boundary conditions in flow field is always an important issue encountered in LES and DNS. Two classes of boundary conditions (laminar and turbulent inlets) are applied in this work. They show their advantages and disadvantages depending on different numerical setups. Time-averaging process directly influences the statistical results. Some criteria have been presented within this configuration which should be considered in every LES statistical procedure. It turns out that a rough implementation of time-averaging process may produce unreliable LES statistical results. To focus on the SGS scalar flux modeling, different SGS scalar flux models have been implemented and the results showed that the SGS anisotropy model achieved an overall better prediction than isotropic eddy diffusivity based models. However, this achievement is appended by more computational time, as shown in Table 6.4.

The next two configurations presented the flow and mixing encountered in many engineering applications. The investigations on the jet in cross flow and jet in channel flow configuration have four objectives.

Firstly, to cover all the mixing scaling phenomena which can be well defined by the molecular Schmidt number *Sc*. Two kinds of working fluid are used. One is water ($Sc > 1$) in the jet in channel flow configuration and another is air ($Sc \leq 1$) in the jet in cross flow configuration.

Secondly, these configurations are paradigms of complex geometers and complex physics. The complexities are stemmed from the strong interaction of jet flow and cross flow existing in near wall region and thus, the near wall effect brings challenges to both the grid resolution and modeling. Therefore, these two configurations present two ways to involve the cross flow: one is the jet flow injected into an open area and cross fluid flows with a free path; another way is to choose the cross flow bounded by four sides walls (channel) which means the mixing happening in a confined area.

Thirdly, focusing on the mixing processes, the influence of the SGS scalar models on the prediction of the mixing has been introduced throughout these configurations. This study aimed at obtaining reliable numerical data for the scalar field.

With the data, the last purpose was to quantitatively describe mixing processes by introducing

the “mixing parameters”. With these parameters, one can easily clarify the effects of different handling parameters on the mixing mechanism comprising macro and micromixng.

Most processes in which mixing is involved require that mixtures are efficient mixed prior to a reaction or further engineering processes. The degree of mixing influences yield and purity of end product. Therefore, which handing parameters can better be modified and how the mixing processes can be controlled draw our further attention. In general, two different approaches can be applied. The first is to change the internal conditions such as flow boundary conditions (active modification). The second is achieved by varying external conditions, for example, the geometrical parameters (passive modification). By varying these handing conditions, the mixing enhancement or modification has been studied within the jet in cross flow configuration.

These previous works only reach to the knowledge of mixing enhancement/modification by the adjustment of some handling parameters. The optimization study has been initiated and carried out. It is a new field to optimize mixing using LES. It was motivated by the LES ability to provide detailed, accurate and comprehensive data of mixing quantities. This study outlined a general procedure to perform the mixing optimization. An impinging jet mixer was used to illustrate the procedure. An optimal jet angle was found and the overall mixing degree with this jet angle reached around six times of the original design. However, it has to be noticed that such technique may be highly time consuming. Because of this, a full loop of mixing analysis is hardly to be performed with LES especially for a complex mixing system. It therefore needs an integration of reduced system in this working routine. The corresponding idea and methodology can directly help engineering design and therefore open a future extension of this work.

To sum up, this work have achieved

- the development, validation and application of a new anisotropy SGS model that is designed to better describe the behavior of SGS scalar flux transport;
- the characterization and quantification of turbulent mixing processes, in terms of scalar structures and degree of mixing along with implementation of passive and active modification techniques
- the attempt towards an optimization of mixing

It therefore establishes LES as valuable tool for these purposes in academic and engineering environments.

Bibliography

[1] A. Bakker, R.D. LaRoche, E.M. Marshall, “Laminar flow in static mixers with helical elements”, published in “The Online CFM Book” at http://www.bakker.org/cfm, 1998

[2] A. Degenhardt, P. Droll, M.E. Ganaoui, L. Kadinski, M. Kurz, A. Lamazouade, D. Morvan, E. Serre, I. Teschauer, P. Bontoux, F. Durst, G. Mueller, M. Schaefer, “High performance computer codes and their application to optimize crystal growth processes II”, In Numerical Flow Simulation II, "Notes on numerical fluid mechanics", Vieweg, 2000

[3] A. Kempf, H. Forkel, J.Y. Chen, A. Sadiki, J. Janicka, “Large-eddy simulation of a counterflow configuration with and without combustion: mixing and flow field”, 8th European Turbulent Conference, 2000

[4] A. Kempf, “Large eddy simulation of non-premixed flames”, Doctoral thesis, 2002

[5] A. Maltsev, “Towards the development and assessment of complete CFD models for the simulation of stationary gas turbine combustion processes”, Doctoral thesis, 2004

[6] A. Mitsuishi, Y. Hasegawa, N. Kasagi, “ Large eddy simulation of mass transfer across an air-water interface at high Schmidt number”, The 6th ASME-JSME Thermal Engineering Joint Conference, 2003

[7] A. Roshko, “Structure of turbulent shear flows: a new look”, AIAA Journal 14, pp.1349-1357, 1976.

[8] A.O. Demuren, “Modeling of jets in cross flow”, NASA Contract No. NAS1–19480, 1994

[9] A.Sadiki, S. Jakirlic, K. Hanjalic, “Towards a thermodynamically consistent, anisotropy-resolving turbulence model for conjugate flow, heat and mass transfer”. Turbulence, Heat and Mass Transfer 4. Begell House, Inc., 2003

[10] A.V. Johansson, P.M. Wikstroem, "DNS and modelling of passive scalar transport in turbulent channel flow with a focus on scalar dissipation rate modelling", Flow, Turbulence and Combusion 63, pp.223-245,1999

[11] A.W. Cook, "Determination of the constant coefficient in scale similarity models of turbulence", Phys. Fluids ,Vol. 9(5), pp.1485-1487, 1997

[12] A. Yoshizawa, "A statistically-derived subgrid model for the large-eddy simulation of turbulence" Phys. Fluids, Vol.25 (9), pp.1532-1538, 1958.

[13] A. Yun, "Development and analysis of advanced explicit algebraic turbulence and scalar flux models for complex engineering configurations", Doctoral thesis, 2005

[14] B. Despres, "Lax theorem and finite volume schemes", Mathematics of Computation, Vol.73, pp.1203-1234, 2003

[15] B.E. Launder, G. J. Reece, W. Rodi, "Progress in the development of a Reynolds-stress turbulence closure", J. Fluid Mech., Vol.68(3), pp. 537-566,1975

[16] B.J. Geurts, "Inverse modeling for large-eddy simulation", Phy. Fluids, Vol.9(12), pp.3585-3588, 1997

[17] B.J. Geurts, "Mixing efficiency in turbulent shear layers", Journal of Turbulence 2-017, 2001

[18] B. Kosovic, "Subgrid-scale modelling for. the large-eddy simulation of high-. Reynolds-number boundary layers", J. Fluid. Mech., Vol.336, pp.151–182, 1997

[19] B. Wegner, Y. Huai, A. Sadiki, "Comparative study of turbulent mixing in jet in cross-flow configurations using LES", International Journal of Heat and Fluid Flow, Selected papers from the 4th International Symposium on Turbulence Heat and Mass Transfer, Vol.25, pp.767-775, 2004

[20] C. Fureby, G. Tabor, H.G. Weller, A.D. Gosman, "A comparative study of subgrid scale models in homogeneous isotropic turbulence", Phys. Fluids, Vol.9(5), pp.1416-1429,1997

[21] C. Meneveau, J. Katz, "Scale-invariance and turbulent models for large eddy simulation", Fluid Mech., Vol.32, pp.1-32, 2000

[22] C. Mengler, C. Heinrich, A. Sadiki, J. Janicka, ”Numerical predictions of momentum and scalar fields in a jet in crossflow: comparison of LES and second order turbulence closure calculations”, 2nd Int. Symp. on Turbulent Shear Flow Phenomena, Vol.II, pp.425-430, 2001

[23] C. Priere, L.Y.M. Gicque, P .Kaufmann, W. Krebs, T. Poinsot, “LES predictions of mixing enhancement for jets in cross-flow”, Journal of Turbulence, 5-005, 2004

[24] C. Speziale, “Analytical methods for the development of Reynolds-stress closures in turbulence”, Annual Review of Fluid Mechanics, Vol.23, pp.107-157, 1991

[25] C. Speziale, “Turbulence modeling for time-dependent RANS and LES-a review”, AIAA paper, 97-2051,1997

[26] D.C. Wilcox, “Turbulence modeling for CFD”, California, DCW Industr. Inc., 1993

[27] D. Lilly, “The representation of small-scale turbulence in numerical simulation experiments”, Proceedings of the IBM Scientific Computing Symposium on Environmental Sciences, pp.195-210, 1967

[28] D. Lilly, “A proposed modification of the Germano subgrid-scale closure method”, Phys. Fluids, Vol.4(3), pp.633-635, 1992

[29] D.R. Unger, F.J. Muzzio, “Laser-induced fluorescence technique for the quantification of mixing in impinging jets”, AIChE Journal, Vol.45(12), pp.2477-2486, 1999

[30] E. Bohr, “Inflow generation technique for large eddy simulation of turbulent boundary layers”, Doctotral thesis, 2005

[31] E J. Gutmark, K.C. Schadow, K.H. Yu,“ Mixing Enhancement in Supersonic Free Shear Flows”, Jnnual Review of Fluid Mechanics, Vol. 27, pp.375-417, 1995

[32] E.V. Driest, “On turbulent flow near a wall”, J. Aeronaut. Sci., Vol.23, p.1007-1011, 1956

[33] E. Villermaux, “Mixing as an aggregation process”, IUTAM Symposium on Turbulent Mixing and Combustion, pp.1-21, 2002

[34] F.A. Jaberi, P.J. Colucci, “Large eddy simulation of heat and mass transport in turbulent flows. part 1: velocity field”, International Journal of Heat and Mass Transfer, Vol.46(10), pp.1811-1825, 2003

[35] F.A. Jaberi, P.J. Colucci, "Large eddy simulation of heat and mass transport in turbulent flows. part 2: scalar field", International Journal of Heat and Mass Transfer, Vol.46(10), pp.1826-1840, 2003

[36] F. Durst, M. Schaefer, "A parallel blockstructured multigrid method for the prediction of incompressible flow", Int. J. of Numerical Methods in Fluids, Vol(22), pp.549-565, 1996

[37] F. Porté-agel, C. Meneveau, M.B. Parlange1, "Some basic properties of the surrogate subgrid-scale heat flux in the atmospheric boundary layer", Boundary-Layer Meteorology 88, pp. 425–444, 1998

[38] F. Sarghini, U. Piomelli, E. Balaras, "Scale-similar models for large eddy simulations", Phys. Fluids, Vol.11, 1596–1607,1999

[39] F.V. Katopodes, R.L. Street, J.H. Ferziger, "Subfilter-scale scalar transport for large-eddy simulation", 14th Symposium on Boundary Layer and Turbulence, American Meteorological Society , pp.472-475, 2000

[40] G. Brethouwer, B.J. Boersma, M.J.B.M. Pourquié, F.T.M. Nieuwstadt, "Direct numerical simulation of turbulent mixing of a passive scalar in pipe flow", Eur. J. of Mech: B/Fluids 18, pp.739-756, 1999

[41] G.Y. He, T. Hsu "The effect of schmidt number on turbulent scalar mixing in a jet-in-crossflow", International Journal of Heat and Mass Transfer, Vol.42, pp.3727-3738,1999

[42] H. Hattori, Y. Murase, Y. Nagano, "DNS of turbulent heat transfer in plane impinging jet", Proceedings of Turbulence, Heat and Mass Transfer 4, pp. 449-456, 2003

[43] H.S. Kang, C. Memeveau "Passive scalar anisotropy in a heated turbulent wake: new observations and implications for large-eddy simulations", J. Fluid Mech., Vol.442, pp.161–170, 2001

[44] H.S. Stone, "An efficient parallel algorithm for the solution of a tridiagonal linear system of equations", J. ACM. 20, pp. 27–38, 1973

[45] J.A. Domaradzki, E.M. Saiki, "A subgrid-scale model based on the estimation of unresolved scales of turbulence", Phys. Fluids, Vol.9(7), pp.2148-2164, 1997

[46] J. Andreopoulos, W. Rodi, "Experimental investigation of jets in a crossflow", J. Fluid Mech., Vol.138, pp.93–127, 1984

[47] J. Baldyga, J. R. Bourne, "Turbulent mixing and chemical reactions", John Wiley & Sons (Editors), 1999

[48] J. Bardina, J. H. Ferziger, W.C. Reynolds. "Improved subgrid scale models for large eddy simulation", AIAA paper 80–1357, 1980

[49] J. Bonnet, R. Moser, W. Rodi, "A selection of test cases for the validation of large eddy simulations of turbulent flows", AGARD advisory report 345, Ch. 6.3 Jets, pp.1-35, 1998

[50] J. Chen, J. Katz, C. Meneveau. "The implication of mismatch between stress and strain-rate in turbulence subjected to rapid straining and destraining on dynamic LES models", J. Fluids Eng. (Submitted), 2004

[51] J. Foss, "Interaction region phenomena for the jet in a cross-flow problem", In: Report SFB 80/E/161, 1980

[52] J.H. Spurk: Strömungslehre, "Einführung in die Theorie der Strömungen", Springer, Berlin, 3. Auflage, 1992

[53] J.M. Redondo, P.F. Linden, "Report on turbulent and mixing in geophysical flow II", Applied Scientific Research 59, pp.89-110, 1998

[54] J. Smagorinsky, "General circulation experiments with the primitive equations I. The basic experiments" J. Mon Weather Rev. 91, pp.99-164,1963

[55] J.U. Schlueter, T. Schoenfeld, "LES of jets in cross flow and its application to a gas turbine burner flow", Turbulence and Combustion 65, pp.177-203, 2000

[56] K. Abe, K. Suga, "Large eddy simulation of passive scalar in complex turbulence with flow impingement and flow separation", Heat Transfer-Asian Research, 30 (5), 2001

[57] K.E. Meyer, O. Ozcan, P.S. Larsen, P. Gjelstrup, G.H. Westergaard, "Point and planar LIF for velocity-concentration correlation in a jet in cross flow ", proceedings of FEDSM, 2001

[58] K. Hanjalic, "The state-of-the-art in modeling turbulent heat transfer", Keynotes, 4th ICCHMT, 2005

[59] K. Horiuti, "A proper verlocity scale for modelling subgris-scale eddy viscosities in large eddy simulation" Phy. Fluids, Vol.5(1), pp.146-157, 1993

[60] K. Horiuti, "A new dynamic two-parameter mixed model for large-eddy simulation", phys. Fluids, Vol.9 (11), pp. 3443-3464, 1997

[61] K. Park, P.K. Oh, "Heat sink optimization using CFD and Kriging method", procedings of 4th ICCHMT, pp.1370-1375, 2005

[62] K.R. Sreenivasan, "The passive scalar spectrum and the Obukhov–Corrsin constant", Phys. Fluids, Vol.8 (1), pp. 189 -196, 1996

[63] L. Davidson, "LES of recirculating flow without any homogeneous direction: a dynamic one-equation subgrid model", 2nd Int. Symp. on Turbulence Heat and Mass Transfer, pp.481-490, 1997

[64] L.K. Hjertager, B.H. Hjertager, N.G. Deen, T. Solberg, "Measurement of turbulent mixing in a confined wake flow using combined PIV And PLIF", Can. J. Chem. Eng., Vol. 81(6), pp. 1149-1158, 2002

[65] L. Moser, M. Cantwell, "PCH00: Fully developed turbulent pipe flow simulations", In: A Collection of Test Cases for the Validation of Large Eddy Simulation. No. 345 in AGARD Advisory Reports. AGARD, Ch. 5: Pipes and Channels, 1998

[66] L. Yuan, R. Street, "Trajectory and entrainment of a round jet in cross-flow", Phys. Fluids, Vol.10 (9), pp.2323-2335,1998

[67] M. Germano, U. Piomelli, P. Moin, W.H. Cabot, "A dynamic subgrid-scale eddy viscosity model", Phy. Fluids, Vol.3(7), pp.1760-1765,1991

[68] M. Klein, A.Sadiki, J.Janicka, "A digital filter based generation of inflow data for spatially developing direct numerical or large eddy simulations", J. Comp. Physics 186, pp.652-665, 2003

[69] M. Klein, A. Kempf, J. Janicka, "Mixing analysis of a plane jet using direct numerical simulation", Proceedings of Euromech 10th European Turbulence Conference, 2004

[70] M. Mihaescu, "Computational aeroacoustics based on large eddy simulation and acoustic analogies", Doctoral thesis, 2005

[71] M. Periç and J.H. Ferziger "Computational Methods for Fluid Dynamics" Springer, 1996

[72] N. Rott, "Note on the history of the Reynolds number", Annual Review of Fluid Mechanics 22, pp.1-11, 1990

[73] O.S. Sun, L. K. Sun, "Experimental assessment of scalar mixing models for large-eddy simulation", 34th AIAA Fluid Dynamics Conference and Exhibit, 2004

[74] P.E. Dimotakis, "Turbulent mixing**",** Annual Review of Fluid Mechanics 37, pp.329-356, 2005

[75] P. Flohr, J.C. Vassilicos, "A scalar subgrid model with flow structure for large-eddy simulation of scalar variances", J. Fluid Mech., Vol.407, pp.315–349, 2000

[76] P. Moin and K. Mahesh, "Direct numerical simulation: a tool in turbulence research", Annual Review in Fluid Mech. 30, pp.539-78, 1998

[77] P.M. Wikstronem, S. Wallun, A.V. Johansson, "Derivation and inverstigation of a new explicit algebrauc model for passive scalar flux", Phys. of Fluids, Vol.5(3), pp.688-702, 2000

[78] R.B. Bird, W. E. Stewart, E. N. Lightfoot, "Transport phenomena", second edition, John Wiley & Sons, Inc., 2002

[79] R. Borghi, "Turbulent combustion modeling", Prog. Energy Combust. Sci.14, pp.245-292, 1988

[80] R. Everson, D. Manin, L. Sirovich and M. Winter, "Quantification of mixing and mixing rate from experimental observations", AIAA Journal, Vol.36(2), pp.121-127, 1998

[81] R. K. Akula, B. Wegner, A. Sadiki, J. Janicka, "Study of the performace of anisotropic SGS models for large eddy simulation", The 12th International Conference on Fluid Flow Technolongies, 2003

[82] R. Kelso, T. Lim, A. Perry, "An experimental study of round jets in cross-flow", J. Fluid Mech., Vol.306, pp.111-144, 1996

[83] R.J. Margason, "Fifty years of jet in cross flow research", presented at an AGARD Meeting on "Computational and Experimental Assessment of Jets in Cross Flow", 1993

[84] R.O.Fox, "Computational models for turbulent reacting flows", 2003

[85] S. Ghosal, "An analysis of numerical errors in large-eddy simulations of turbulence", Journal of Computational Physics, Vol.125(1), pp.87-206, 1996

[86] S.H. Peng, L. Davidson, "On a subgrid-scale heat flux model for large eddy simulation of turbulent thermal flow", Internationa Joural of Heat Mass Transfer, Vol.45, pp.1393-1405, 2002

[87] S. Kurien, K.G. Aivalis, K.R. Sreenivasan, "Anisotropy of small–scale turbulence", J. Fluid. Mech, Vol.448, pp.279-288, 2001

[88] S.M. de Bruyn Kops, J. J. Riley, "Direct numerical simulation of reacting scalar mixing layers", Phys. of Fluids, Vol.13(5), pp.1450-1465, 2001

[89] S. Menon, P.K. Yeung, W.W. Kim, "Effect of subgrid models on the computed interscale energy transfer in isotropic turbulence", Computers and Fluids, Vol. 25, pp.165-180, 1996

[90] S. Nakamura, R.S. Brodkey, "Direct and large eddy simualtion of the three-dimensional unsteady flows in the counter-jet mixing vessel", Fluids Engieering Summer Conference Boston, 2000

[91] S. Pope, "Turbulent flows". Cambridge University Press, 2000

[92] S.S. Girimaji, Y. Zhou "Analysis and modeling of subgrid scalar mixing using numerical data", Phys. Fluids, Vol.8(5), pp.1224-1236, 1996

[93] S. Stanley, S. Sarkar, J. Mellado, "A study of the flow field evolution and mixing in a planar turbulent jet using direct numerical simulation", J. Fluid. Mech., Vol.450, pp.377-407, 2002

[94] S. Stolz, N.A. Adams, "An approximate deconvolution procedure for large-eddy simulation", Phys. Fluids, Vol.11(7), 1999

[95] S.V. Alekseenko, P.A. Kuibin, V.L. Okulov, S.I. Shtork, "Helical vortices in swirl flow", J. Fluid Mech., Vol. 382, pp.195-243, 1999

[96] T. Eidson, "Numerical simulation of the turbulent Rayleigh-Bénard problem using subgrid modeling", J. Fluid Mech., Vol.158, pp.245-268, 1985

[97] T.F. Fric, A. Roshko, "Vortical stucture in the wake of a transverse jet", J. Fluid. Mech., Vol.279, pp.1-47, 1994

[98] T. Lehnhauser, M. Schaefer, "Improved linear interpolation practice for finite-volume schemes on complex grids", Int. J. Numerical Methods in Fluids 38, pp.625-645, 2002

[99] U. Piomelli, "Large-eddy and direct simulation of turbulent flows", 9e Conference Anunelle de la Societe Canadienne de CFD, 1998

[100] U. Piomelli, "Large eddy simulation: achievements and challenges", Progress in Aerospace Sciences 35, pp.335-362, 1999

[101] W. Cabot, P. Moin, "Large eddy simulation of scalar transport with the dynamic subgrid-scalar mode", LES of Scalar Transport, pp.142-158, 1993

[102] W. Layton, "A mathematical introduction to large eddy simulation", Computational Fluid Dynamics-Multiscale Methods (H. Deconinck, editor), 2002

[103] W. Rodi, J.H. Ferziger, M. Breuer, M. Pourquie,"Status of large eddy simulation: results of a workshop", J. Fluids Engineering 119, pp.248-261, 1997

[104] Y. Chang, A.Vakili, "Dynamics of vortex rings in crossflow", Phys. Fluids, Vol.7(7), pp.1583-1597, 1995

[105] Y. Huai, B. Wegner, A. Sadiki, C. Olbricht, "Numerical Investigation of Mixing Process", Proceedings of International Conference on Micromixing in Turbulent Flows with Chemical Reaction, 2004

[106] Y. Huai, B. Wegner, A. Sadiki, "Effects of flow and scalar subgrid scale modelling on LES performance for mixing analysis", Proceedings of Euromech 10th European Turbulence Conference, 2004

[107] Y. Huai, A. Sadiki, "Investigation of heat and mass transfer in a jet in channel flow configuration using LES", Proceedings of 4th ICCHMT, pp. 223-228, 2005

[108] Y. M. Marzouk and A. F. Ghoniem. "Vorticity formulation for an actuated jet in crossflow." AIAA paper, pp. 2004-0096, 2004

[109] Z. Warhaft, "Passive scalars in turbulent flows" Ann. Rev. Fluid Mech.32, pp.203-240, 2000

Resume of Ying Huai

Date of birth: 7, April, 1976 Nationality: Chinese

Education and Experience:

1995－1999 Undergraduate education, Bachelor of Engineering
Power System Department, Sichuan Technology University, China
Major: Automatic Control

2000－2002 Graduate education, Master of Science
Mads Clausen Institute, University of Southern Denmark, Denmark
Major: Fluid Mechanics

2001－2002 Internship (master project) at R&D Department
Danfoss Drives AG, Denmark
Project title “Heat transfer processes in electric induction motors”

2002－2005 PhD education
Institute for Energy and Powerplant Technology, Darmstadt University of Technology, Germany
Major: Large Eddy Simulation in the Scalar Field

Large Eddy Simulation in the Scalar Field

Abstract

Focusing on Large Eddy Simulation (LES) in the scalar field, this work has threefold achievement:

- The development, validation and application of a new anisotropy subgrid scale (SGS) model that is designed to better describe the behavior of SGS scalar flux transport

In the frame of LES, a new developed anisotropy model is proposed and implemented. Unlike the isotropic SGS scalar flux models, the new model involves the anisotropic diffusivity and takes into account the scalar gradients in different directions of flows. This model is validated in different engineering related configurations of various complexities, which include a mixing layer problem, a jet in cross flow and jet in channel flow configuration. Thereby mixing processes involving low Schmidt number and high Schmidt number effects have been carefully examined. It is shown that the proposed model achieves a good agreement with the experimental data and significantly outperforms isotropic form models.

- The characterization and quantification of turbulent mixing processes, in terms of scalar structures and degree of mixing along with implementation of passive and active modification techniques

To provide a methodic analysis of turbulent mixing processes, a representation of mixing is involved, which includes its physical nature, scales and resolution study. With this understanding, the so-called “Mixing parameters” are introduced. The ability of these parameters to retrieve the mixing mechanism is clearly established within different mixing processes. A mixedness parameter (MIX) can represent the probability of mixed fluids in the computational domain. The following two are the spatial mixing deficiency (SMD) and the temporal mixing deficiency (TMD) parameters for characterizing the macromixing and micromixing.

- The attempt towards an optimization of mixing

A numerical mixing optimization procedure is demonstrated using LES. The motivation is that LES has the approved ability to obtain detailed, accurate and comprehensive data of mixing quantities, which meets the requirement of mixing optimization design. Although the principal focus is a specific impingement mixing mixer problem, the methodology developed is equally applicable to virtually any aspect of technology and engineering, where mixing processes are important.

Ying Huai

Grobstruktursimulation des skalaren Feldes

Kurzfassung

Durch Anwendung der Grobstruktursimulation (LES) zur Bestimmung von skalaren Verteilungen konnte diese Arbeit wissenschaftliche Erkenntnisse erzielen, die sich in drei Bereichen unterteilen lassen:

- Im Rahmen des LES-Verfahrens wurde ein neues Anisotropie-Modell erstellt und so implementiert, dass es eine verbesserte Beschreibung des Skalarflusstransports der Feinstrukturkomponenten liefert. Dieses Modell wurde auf etliche technisch relevante Konfigurationen unterschiedlicher Komplexität appliziert, die sowohl die Mischungsschichtproblematik seitlich umströmter Freistrahlströmungen als auch Rohrströmungen umfassten. Dabei wurden Mischungsprozesse sowohl mit kleinen Schmidt-Zahlen als auch mit hohen Schmidt-Zahlen sorgfältig untersucht, und es konnte gezeigt werden, dass das hier verwendete Modell eine gute Übereinstimmung mit experimentellen Daten, besonders im isotropen Fall, erzielt.

- Um eine methodische Analyse der turbulenten Mischung zu erhalten, wurde die Mischung so beschrieben, dass die physikalischen Prozesse, Skalen und Strukturen korrekt wiedergegeben werden. Im Rahmen dieser Beschreibung wurden die sog. „Mischungsparameter“ eingeführt. Die Fähigkeit dieser Parameter, Mischungsprozesse korrekt zu beschreiben ist mit der Anwendung unterschiedlicher Mischungsprozesse zu erklären. Der Vermischungsparameter (MIX) repräsentiert die Wahrscheinlichkeit von vermischten Komponenten im betrachteten Berechnungsgebiet. Die weiteren verwendeten Parameter zur Charakterisierung der Makro- und Mikromischung sind der räumliche Mischungsmangel (SMD) und der zeitliche Mischungsmangel (TMD).

- Eine numerische Prozedur zur Mischungsoptimierung wird mittels der LES-Methode veranschaulicht. Obwohl der Schwerpunkt auf die Wechselwirkung zwischen Mischung und Mixer gelegt wurde, können die hier entwickelten und angewandten Methoden auf beliebige ingenieurtechnischen Problematiken, die Mischungsprozesse enthalten, appliziert werden.

Ying Huai